PHYSIOLOGICAL BASIS AND FUNCTION OF DEPOLARIZING AFTERPOTENTIALS IN THE ENTORHINAL CORTEX

FRANZISKA S. KÜMPFBECK

Dissertation der Fakultät für Biologie der
Ludwig-Maximilians-Universität München

24th July 2018

Franziska S. Kümpfbeck: *Physiological Basis and Function of Depolarizing Afterpotentials in the Entorhinal Cortex*

Reviewer 1: Prof. Dr. Andreas Herz
Reviewer 2: Prof. Dr. Laura Busse
Date of submission: 24th July 2018
Date of oral defense: 1st April 2019

Für Opa,

CONTENTS

ABSTRACT

In rodents, supra-threshold responses of layer II neurons of the medial entorhinal cortex (mEC) depend on the location of the animal. While an animal explores its surroundings, the cells' membrane potentials exhibit dynamics on different time scales that include slow sub-threshold voltage ramps, theta-band oscillations and supra-threshold burst episodes with inter-spike-intervals shorter than 10 milliseconds. These irregular high-frequency burst episodes have received little attention but may add substantial information about the animal's location in space.

A large group of principal neurons in layer II of the mEC have a stellate morphology, with many primary dendrites attached to the cell body. These cells also exhibit distinct physiological characteristics. They display sag responses to injected hyperpolarizing step currents, resonances to oscillatory current injections and short spike latencies at rheobase. These cells also show a prominent depolarizing afterpotential (DAP) following an action potential. This additional depolarization lasts for 2-8 milliseconds and might enhance burst episodes in these stellate cells.

In this thesis, I investigate how intrinsic cellular properties affect the DAP and explore the DAP's potential functional role. To do so, I performed whole-cell current-clamp recordings from layer II cells in acute brain slices of the mEC of mature rats and gerbils near physiological temperature (~35◦C). In layer II, pyramidal and stellate cells differed in their response properties. Only stellate cells responded to current stimuli with a characteristically short latency. They also exhibited more pronounced sag responses, more robust membrane voltage resonances to sinusoidal current injection in the theta range, and stronger DAPs than pyramidal cells. Both the DAP width and amplitude could be modulated by hyperpolarization of the membrane potential prior to the action potential. DAPs were completely blocked by different calcium channel blockers NNC, Cadmium and Nifedipin. Low TTX concentrations also abolished the DAP, whereas the selective blocker of I_h ZD7288 only decreased the DAP amplitude. However, results of control experiments without drug application revealed a washout effect which complicated the interpretation of all pharmacological recordings.

To elucidate the functional impact of the DAP, we assayed its influence on action potential generation in a paired pulse paradigm. The intensity of the first current pulse was chosen to elicit an action potential, while the intensity of the second pulse was varied. Larger DAPs provide a window of opportunity to spike again.

To mimic in-vivo firing responses I injected a sinusoidal current (theta oscillation) modulated by a slow depolarizing wave (ramp). Membrane oscillations occur jointly with a slow ramp during a grid-field passage. The hypothesis that I wanted to test was whether these phenomena are suited to amplify bursting. I was, however, not able to reliably elicit short bursts in these experiments or corroborate the hypothesis. Short bursts were also not elicited in control experiments.

Future directions will include combining the collected data with computational modeling to construct a comprehensive and consistent biophysical portrait of mEC layer II cells.

1 INTRODUCTION

An ultimate goal of neuroscience is to understand how complex cognitive processes, such as memory, learning, decision making and path finding in space, work. Neuronal information processing between and within cortical networks proceeds at many time scales and depends on the temporal characteristics of activity patterns at the single neuron and population level. For example, brief bursts of spikes play important roles in brain function, among others by facilitating transmitter release during long-term potentiation or by serving as conditional synchrony detector (Magee and Johnston, 1997; Harris et al., 2001). A classical system to investigate how bursts of spikes modulate neuronal processing is the hippocampal formation (HF).

1.1 ARCHITECTURE OF THE HIPPOCAMPAL FORMATION

The hippocampal formation is a crucial component of the medial temporal lobe (Ma et al., 2008) and plays an important role in memory and spatial navigation (O'Keefe and Dostrovsky, 1971; Zola-Morgan et al., 1989). The neuroanatomist Santiago Ramón y Cajal investigated its structures and connections at the beginning of the 20th century (Fig. 1.1). According to Andersen, Morris et al., 2009, the HF is defined as the entorhinal cortex, the dentate gyrus (DG), the hippocampus proper with its subfields Cornu Ammonis (CA) 1, CA2 and CA3, the subiculum, and the pre- and parasubiculum. Others segregate the three layered cortical HF structure (DG, CA3, CA2, CA1 and subiculum) from the six layered parahippocampal region (presubiculum, parasubiculum and entorhinal cortex) (Witter, Naber et al., 2000). In the following, I will refer to the first definition of HF based on the fact that the entorhinal cortex is the first relay station that processes neocortical input to the HF (Andersen, Morris et al., 2009).

Important anatomical connections include the trisynaptic loop within the HF. This unidirectional loop consists of the following three synapses (Yeckel and Berger, 1990; Andersen, Blackstad et al., 1966): First, the stellate cells of the EC layer II project to the granule cells of the dentate gyrus. This excitatory connection is also known as the perforant path (Schwartz and Coleman,

1981; Doller and Weight, 1982). Second, the dentate gyrus connects to the CA3 region via mossy fibres. Third, Schaffer collaterals of CA3 pyramidal neurons synapse onto CA1 pyramidal neurons (Yeckel and Berger, 1990).

It is important to note that the entorhinal-hippocampal circuitry also has other pathways (Fig. 1.1) (Van Strien et al., 2009). For example, there is another component of the perforant path, which includes the direct connection between entorhinal layer III pyramidal cells and CA1 (Steward, 1976; Dickson, Mena et al., 1997). From CA1 the signals are further conveyed to the subiculum or directly to the deeper layers of the entorhinal cortex.

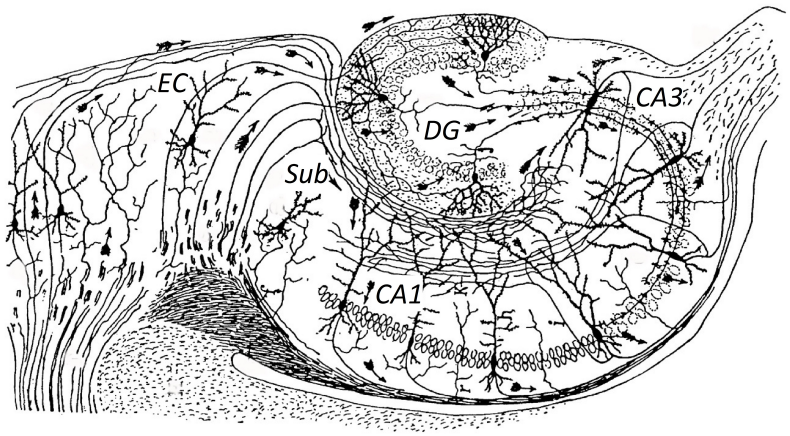

Figure 1.1: Hippocampal formation illustrated by Ramón y Cajal (1909). Horizontal section of a rodent brain with the defined subfields of the hippocampal formation: entorhinal cortex (EC), dentate gyrus (DG), hippocampal CA3 and CA1, the subiculum (Sub). Defined subfields were adapted by me. Presubiclum (PrS) and parasubiculum (PaS) are not marked.

1.1.1 *Entorhinal cortex*

The entorhinal cortex (EC) (Brodmann's area 28) can be considered as the nodal point between a variety of multimodal cortices (prefrontal, temporal, etc.) and the rest of the HF. The EC can be subdivided into two areas: the lateral EC (lEC) and the medial EC (mEC, see Fig. 1.2) (Brodmann, 1909; Steward, 1976). The presubiculum (PrS), the parasubiculum (PaS), the postrhinal cortex (POR) and the perirhinal cortex (PER) are the source of major inputs to the EC (Van Hoesen and Pandya, 1975; Suzuki and Amaral, 1994). The PER preferentially projects to the lEC (Naber, Caballero-Bleda et al., 1997). The PrS, PaS and POR on the other hand provide substantial inputs to the medial entorhinal cortex (Koganezawa et al., 2015; Caballero-Bleda et al.,

1993; Canto and Witter, 2012). Given the distinct input streams of the two entorhinal areas to the hippocampus, Witter, Doan et al., 2017 posited that the lEC is more likely to be involved in object information and attention processing. In contrast, the mEC is thought to play a very important role in spatial processing through the convergence of inputs to this area. In particular, the mEC contains a number of spatially modulated cell, including border and grid cells (see subsection 1.2.3 and 1.2.4).

The EC is composed of six different layers with a homogeneous distribution of neurons (Ramón y Cajal, 1909; Witter, Doan et al., 2017). Layer I/the superficial plexiform and layer IV contain no or only few neuronal cell bodies, whereas layers II, III, V, VI are considered to be cellular layers (Canto, Wouterlood et al., 2008). The EC layer II stellate cells provide the main input to the HF via the perforant path (see subsection 1.1), whereas EC layer III pyramidal cells project directly to CA1 and the Sub. The axons of layer V and VI neurons project to the angular bundle, an axonal fibre tract connecting the parahippocampal region with the HF, in the direction the Sub and superficial EC layers (Hamam et al., 2000; Canto, Wouterlood et al., 2008).

The different layers and the specific morphology, electrophysiological properties and projections of cells in the entorhinal cortex will be described in more detail in a later subsection (see subsection 1.3).

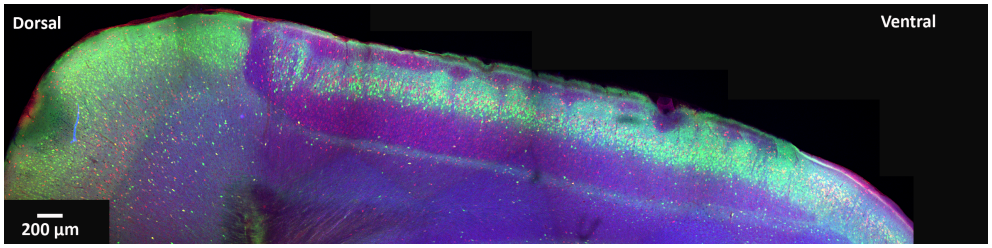

Figure 1.2: Confocal image of a sagittal rat brain section showing the medial entorhinal cortex. Cells were stained against Reelin (red, stellate cells), Calbindin (green, pyramidal cells) and MAP2 (blue, all neurons).

1.1.2 *Dentate gyrus*

The dentate gyrus (DG) receives its major unidirectional input from the EC via the perforant path and ultimately transfers information to the CA3 (see subsection 1.1). Three layers characterize the DG. The first layer, the molecular layer or hilus, is relatively cell-free and contains dendrites of dentate granule cells, perforant path fibers and a few interneurons (Van Strien et al., 2009).

Second, as suggested by its name, the principal or granule cell layer is mainly composed of tightly packed principal granule cells. The third layer is called the polymorphic cell layer and mainly hosts mossy and fusiform cells. The DG can be distinguished by its 'U'- or 'V'-shaped structure. This structure is built up by the first two cell layers and subdivided into the infrapyramidal and the suprapyramidal blade. These two substructures are connected via the so-called crest. The suprapyramidal blade or enclosed blade is situated between the CA3 and the CA1 field. Axonal terminals coming from the EC are constrained to the molecular layer, where they connect primarily to the dendritic spines of layer II granule cells. Mossy fibers, characteristically unmyelinated axons of the granule cells, transfer the information further to the mossy cells of the polymorphic layer and to the pyramidal cells of the CA3 area (Amaral, Scharfman et al., 2007).

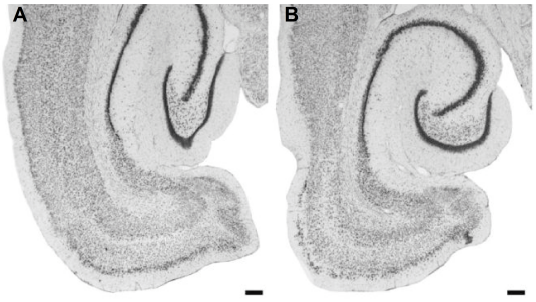

Figure 1.3: Horizontal section through the rat hippocampal formation illustrating the 'V-' (A, more dorsally located) or 'U'-shaped (B, more ventrally located) dentate gyrus (adapted from Amaral, Scharfman et al., 2007, with permission). Scale bar = 250 μm.

1.1.3 *Hippocampus proper*

The hippocampus proper was termed and subdivided by Lorente de Nó (1934) into three similarly organized fields of the Ammons's horn: CA1, CA2 and CA3. The cell layers of these three fields are known as strata: oriens, pyramidale, lucidum (only in CA3), radiatum and lacunosum-moleculare. The first layer, stratum oriens, is relatively neuron-free, only comprising interneurons and efferent/afferent fibres. Above this layer lies the stratum pyramidale, consisting of pyramidal neurons. The composition of the most superficial layer is subdivided and varies between CA3 and CA1/CA2. In CA1 and CA2 the stratum pyramidale is followed by the stratum radiatum, containing the apical dendrites of the pyramidal cells. Schaffer collateral

connections were found within CA3 and from CA3 to CA1. The CA3 to CA1 projections are organized topographically: the distal part of CA3 projects to the proximal CA1 and while the proximal part of CA3 projects to the distal CA1. However, the CA3 region consists of an extra layer between the stratum pyramidale and the stratum radiatum: the cell-free stratum lucidum. This layer receives inputs from the DG. The most superficial layer is the stratum lacunosum-moleculare, which comprises synaptic terminals of the perforant path (Van Strien et al., 2009; Witter and Amaral, 2004). In contrast to the CA1 and CA2 regions, CA3 additionally receives inputs from the DG mossy fibres. CA1 projects to the EC either directly on indirectly via the subiculum. Proximal CA1 neurons directly transfer information to the mEC. In contrast, distal CA1 cells synapse onto cells of the lEC (Tamamaki and Nojyo, 1995; Naber, Lopes Da Silva et al., 2001).

1.1.4 *Subiculum*

The subiculum (Sub) has received less attention than the other regions of the HF, even though it is the major output structure of the hippocampus projecting back to the EC (S. M. O'Mara et al., 2001; Tamamaki and Nojyo, 1995; Witter and Amaral, 2004). The Sub is the transition zone between the hippocampus and the EC (Stafstrom, 2005) and consists of three layers. First, a molecular layer extends the strata lacunosum-moleculare and radiatum of the neighboring CA1. Second, the enlarged pyramidal cell layer comprises the less tightly packed principal neuron somata which project their apical dendrites into the molecular layer. This layer also contains smaller neurons considered to be GABAergic interneurons. The third layer is a polymorphic or fibre layer (Stafstrom, 2005; S. O'Mara, 2005). The Sub receives its primary inputs from the CA1 pyramidal cell layer in a topographical manner (Amaral, Dolorfo et al., 1991). Proximal CA1 fibers project to the distal Sub, and distal CA1 fibers to the proximal Sub (S. O'Mara, 2005). Oligosynaptic backprojections to the CA1 also exist (Commins et al., 2002; Van Strien et al., 2009). However, the Sub also receives direct inputs from the EC (Naber, Witter et al., 1999) and as already mentioned above, processes information further mainly to the EC but also to other cortical and subcortical targets (S. O'Mara, 2005). Sub-to-EC connections are also organized topographically. Neurons of the proximal Sub innervate the lEC, whereas neurons of the distal Sub project to the mEC (Tamamaki and Nojyo, 1995; Stafstrom, 2005). Additionally, reciprocal connections exist between the Sub, EC and other subcortical fields (Van Strien et al., 2009).

1.1.5 *Pre- and Parasubiculum*

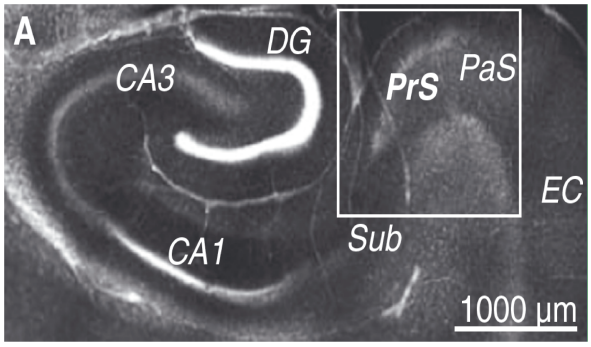

Figure 1.4: Hippocampal formation indicating the presubiculum and parasubiculum (adapted from Simonnet et al., 2013, with permission). Horizontal section stained with 4',6-diamidino-2-phenylindole. Subiculum (Sub), entorhinal cortex (EC), dentate gyrus (DG), CA3 and CA1 regions are also indicated.

The presubiculum (PrS) and parasubiculum (PaS) constitute the transitional area between the hippocampal archicortex and the six-layered neocortex, here the EC (see Fig. 1.4) (Simonnet et al., 2013; Ding, 2013; Nassar et al., 2015). PrS and PaS can be distinguished by the condensation of the neurons. in the PrS, layer II contains small and very densely packed pyramidal cells, whereas cells in deeper layers are less compressed. In contrast to this arrangement, layer II and III of the PaS comprise large and densely packed pyramidal cells. The superficial cell-free zone located above layer II of the PrS is continuous within the EC as well as the deeper layers of the PrS (Witter and Amaral, 2004; Abbasi and Kumar, 2014; Nassar et al., 2015). The PrS and PaS receive major inputs from the EC and the Sub (also reciprocally connected), which exhibit a topographical organization (Groen and Wyss, 1990; Funahashi and Stewart, 1997). Both regions also receive inputs from the retrosplenial cortex, the thalamus and many others (Groen and Wyss, 1990). Neurons in all layers of the PrS and PaS send their projections to the molecular layer of the DG, the Sub and to the stratum lacunosum-moleculare of CA3 and CA1 (Witter and Amaral, 2004). Caballero-Bleda et al. (1993) discovered that the PrS and PaS differently innervate the EC: the PrS primarily innervates layer III/I while the Pas innervates layer II (Haeften et al., 1997). The PaS shows a gradient in the density of projections to the EC. As a result, neurons from the proximal portion of the PaS project to the medial regions of mEC, whereas neurons from the center send their projections primarily to lateral parts of the mEC and to the most medial parts of the lEC. The distal area of the PaS projects mainly to the mediolateral region of the lEC (me-

diolateral gradient in the EC). The topographical organization of projections from the PrS to the EC is inverted in contrast to the PaS projection pattern. Proximal PrS cells project to the most lateral region of the mEC while distal cells innervate the central part of the mEC. Cells in the central region of PrS project to the most medial area of the mEC (Groen and Wyss, 1990).

1.2 FUNCTION OF THE HIPPOCAMPAL FORMATION: THE NEURONAL REPRESENTATION OF SPACE

Two main functions of the HF have dominated research in the last decades: 1. its role within the memory formation and consolidation, and 2. its crucial role in spatial representation and navigation (Andersen, Morris et al., 2009). A bilateral hippocampal ablation of severely epileptic patient Henry Gustav Molaison (H.M.) confirmed that the HF has a critical function in memory formation. After removal, the patient H.M. suffered from severe global amnesia. He was unable to form new memories (anterograde amnesia), but also showed a partial retrograde amnesia of the time just before the operation (Scoville and Milner, 1957).
Donald Hebb (1949) focussed on how memories are formed and consolidated. Hebb's rule is often summarised as 'cells that fire together wire together'. Such strengthening of synaptic connections through simultaneous activity in the pre- and postsynaptic neuron is presumed to be intimately linked to long-term potentiation (LTP) (Bliss and T, 1973). In contrast, long-term depression is a process which selectively weakens specific synapses (Massey and Bashir, 2007). At the millisecond time scale, potentiation often depends on the relative timing of pre-and postsynaptic spikes; this is known as spike-timing dependent plasticity (STDP) (Levy and Steward, 1983). These phenomena of synaptic plasticity play crucial roles in learning and memory formation.
Probing episodic memories in rodents and many other animals is usually done through spatial navigation tasks, which have been demonstrated to involve the HF. The nervous system of animals has evolved to make sense of cues that define the external environment and plan movement. To allow for adaptive responses, different activity patterns of the nervous systems reflect or correlate with features of the external world, these are referred to as neuronal representation (E. I. Moser et al., 2014). According to the mathematician and philosopher Gottfried Leibnitz (1715) "space is that which results from places taken together". Nearly 250 years later, O'Keefe and Dostrovsky (1971) discovered that space has a direct neural correlate: firing fields of hippocampal place cells. John O'Keefe received the Nobel prize in Physiology

or Medicine in 2014 for his work on place cells (see subsection 1.2.1) together with Edvard and May-Britt Moser, who in turn discovered entorhinal grid cells (2004) (see subsection 1.2.3). The following subsections will introduce cells in the hippocampal formation, which have been implicated in the representation of different aspects of space.

1.2.1 *Place cells*

Besides its role of memory formation and consolidation, the hippocampus plays a crucial role in spatial representation and navigation. O'Keefe and Dostrovsky (1971) discovered complex-spiking neurons in the rat hippocampus proper. These cells elicited action potentials whenever the animal crossed a certain field within its environment, called the 'place field' (see Fig. 1.5). Activated cells were identified as pyramidal neurons and named 'place cells': cells spike at different places, covering - and thereby representing- the animals' whole environment (O'Keefe, 1976). Many other experiments have followed, leading to a more in-depth characterization of place cells. One of these properties is that place cells shift their place fields in response to shifts of distal landmarks (Muller and Kubie, 1987; O'Keefe and Speakman, 1987). Another interesting observation is that place cells still elicit place fields in the dark after removing the landmarks (O'Keefe, 1976; Quirk et al., 1990). Moreover, place cells exhibit different place fields in different environments (O'Keefe and Conway, 1978). The activity of place cells appears to depend on locomotion, as shown by a decrease in responsiveness after restricting an animals' movement (Foster et al., 1989). Another very well known property of place cells on restricted tracks such as arm mazes is the complete direction-dependence on the environment (McNaughton, Barnes et al., 1983). In contrast, in open fields, place cell firing is not directional (Muller, Bostock et al., 1994).
Place cell firing is also accompanied by the background hippocampal theta rhythm. Yet the place cells fire at a slightly faster pace, which means that their spikes "phase precess" relative to the theta phase. As the animal enters a place field, the cell spikes late within the theta cycle. As the animal progresses through the field, the spikes shift earlier in phase until they have shifted by up to 360°, when the animal leaves the field. This describes the theta phase precession phenomenon of place cell firing, whereby place cells fire at progressively earlier phases of the theta rhythm (O'Keefe, Recce et al., 1993). Theta phase precession has also been studied in layer II grid cells of the mEC (see subsection 1.2.3) (Hafting, Fyhn, Bonnevie et al., 2008). This kind of temporal coding is thought to supply the system with more precise spatial information and facilitate memory for spatial and temporal se-

quences (O'Keefe, Recce et al., 1993; Skaggs and McNaughton, 1996; Moser et al., 2017).

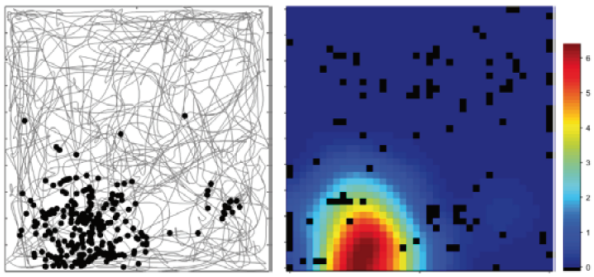

Figure 1.5: Place cell adapted from Moser et al., 2017, with permission. Left: trajectory in gray of a rat exploring its environment. The black superimposed dots represent the location of the animal when spikes occurred. Right: color-coded rate map which corresponds to the trajectory with red indicating the maximum rate and blue indicating the minimum rate.

1.2.2 *Head-direction cells*

Another scientific breakthrough in the field of neuronal spatial representation was the discovery of head-direction cells. These cells are specifically active if the animal's head faces a certain direction, regardless of the animal's location (see Fig. 1.6). Head-direction cells were first found in the dorsal presubiculum by Taube, Muller and Ranck, JB, 1990. They have since also been found in the parasubiculum and in the layers III-VI of the mEC and in the anterior thalamus (Burgalossi, Herfst et al., 2011; Sargolini et al., 2006; Boccara et al., 2010; Taube and Muller, 1998). The vestibular system seems to have an influence on head-direction cells by sustaining their direction alignment when the animal is in complete darkness. Visual landmarks can reset these head-direction cells (Robertson et al., 1998).

1.2.3 *Grid cells*

Spatially modulated firing behavior was also found in mEC layers II and III. A striking characteristic of these neurons is that they display a hexagonal grid-like periodic pattern with multipeaked place fields over the entire environment of the animal (Fig. 1.7). Therefore, these neurons are called grid cells (Fyhn, Molden et al., 2004; Hafting, Fyhn, Molden et al., 2005). Grid cells co-exist with head-direction cells (see subsection 1.2.2) and border cells (see subsection 1.2.4) in the superficial layers of the mEC (Sargolini et al.,

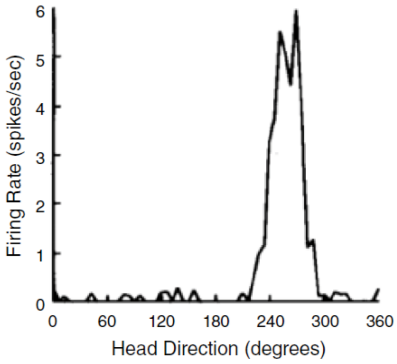

Figure 1.6: Head-direction cell (adapted from Moser et al. (2017), with permission): Firing rate as a function of head direction (maximum firing rate elicited around 250°).

2006; Boccara et al., 2010).
Hafting, Fyhn, Molden et al. (2005) characterized grid cells using several key parameters: 1. the size of the firing fields; 2. the distance between firing fields, referred to "spacing"; 3. the stable phase, which describes the x,y location of the grid vertices; 4. the direction/tilting of the grid with respect to an external reference line (Fyhn, Molden et al., 2004; Fyhn, Hafting et al., 2007). Additionally, the amplitude of the firing rates have been shown to differ between fields (Hafting, Fyhn, Molden et al., 2005). The formation of the hexagonal firing structure and its spacing are insensitive to changes in the environment or the removal of external sensory inputs. Grid cells maintain firing relationship to neighboring grid cells (Hafting, Fyhn, Molden et al., 2005; Fyhn, Hafting et al., 2007). Brun et al. (2008) and Stensola et al. (2012) found that grid spacing together with the grid field size increase along the dorso-ventral axis of the mEC. This increase is not continuous; rather it is clustered into at least four so-called modules, with each module having its own parameters (orientation, scale) (Stensola et al., 2012; Moser et al., 2017).

1.2.4 *Border cells*

The existence of border cells was already predicted from computational models as inputs leading to the typical spatial firing of hippocampal place cells (O' Keefe and Burgess, 1996; Burgess and O'Keefe, 1996; Burgess, Jackson et al., 2000). They were discovered in 2008 by Solstad et al. These cells typically only fire along the geometric border of the local environment, as illustrated in Figure 1.8. Border cells and border-like firing cells were found in the mEC,

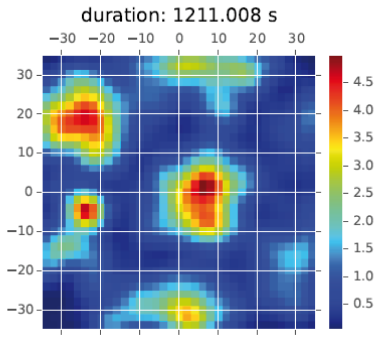

Figure 1.7: Grid cell: Color-coded rate maps with red indicating the maximum firing rate and dark blue indicating little or no firing. This data set was provided by courtesy of Latuske et al. (2015) and the figure was provided by courtesy of Dora Csordas.

the PaS, the Sub and the hippocampus (Solstad et al., 2008; Barry et al., 2006; Lever et al., 2009). Within the mEC, border cells intermingle with grid cells and head-direction cells. Border cells can be distinguished from the other two cell types by their activity pattern. Grid cells and border cells were never reported to transform into the other cell type. In contrast, border and head-direction cells can overlap in so-called 'conjunctive' border cells, which fire only within their field when the rat moves in a certain direction. In the mEC, border cells comprise less than 10% of the principal neurons (Solstad et al., 2008; Moser et al., 2017).

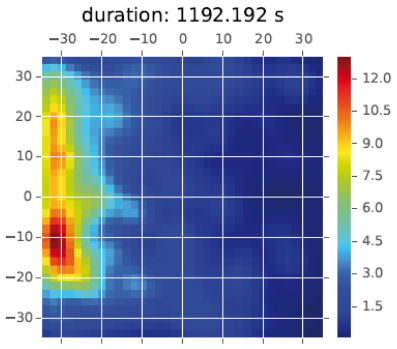

Figure 1.8: Border cell: Color-coded rate maps with red indicating the maximum firing rate and dark blue indicating little or no firing. This dataset was provided by courtesy of Latuske et al. (2015) and the figure was provided by courtesy of Dora Csordas.

1.2.5 *Speed cells*

Speed cells are the most recently discovered cell type involved with spatial representation in the hippocampal formation. In the hippocampus and in layer III and deeper layers of the mEC, it had already been observed that place and grid cells contained information on changes in the animal's speed (McNaughton, Barnes et al., 1983; Hirase et al., 1999; Sargolini et al., 2006). Kropff et al. (2015) found that a considerable fraction of neurons (15 %) across all layers of the mEC, respond linearly to the running speed of the animal and only weakly to spatial or directional changes (see Fig. 1.9). Speed cells fire independently of visual inputs, leading to the suggestion that the input signal of these cells originates from proprioceptive or motor-efference parts of the mesencephalon. Neurons with similar features were also found in the hippocampus, but with a larger overlap with other cell types, in contrast to the speed cell population in the mEC (Kropff et al., 2015; Ye et al., 2018). MEC speed cells were shown to be fast-spiking, Parvalbumin-expressing, putative GABAergic neurons directly projecting to hippocampal areas (Buetfering et al., 2014; Ye et al., 2018).

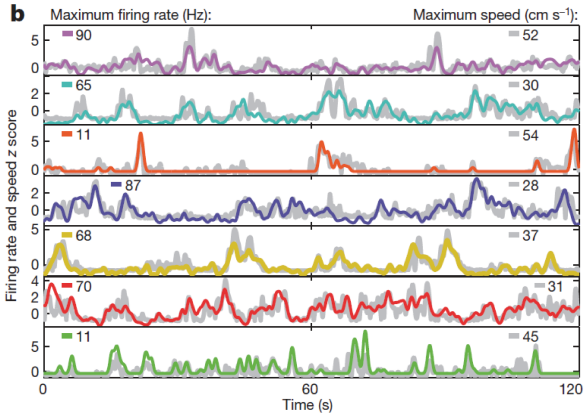

Figure 1.9: Speed cells, adapted from Kropff et al. (2015), with permission. Traces show z scores for firing rate (colour) and speed (grey) for seven representative entorhinal speed cells during 2 min of free foraging (different sessions). Maximum values of firing rate and speed are indicated (left and right, respectively).

Grid, border, head-direction and speed cells were all discovered in layers of the mEC (mainly superficial layers I-III), which leads to the assumption that these cell types may interact with each other. However, it is still not clear which neuron or interneuron types underlie these spatially tuned cells and how these individual neurons contribute to spatial representation (Burgalossi, Herfst et al., 2011). A more in-depth characterization of these cells' morphology and physiology will advance our understanding of the microcircuit underlying spatial representation. The following subsections describe layers I-III of the mEC (already briefly described in subsection 1.1.1) in more detail (see Fig. 1.10).

1.3.1 *Layer I*

Layer I of the mEC is relatively cell-free with scattered horizontal and multipolar neurons (see Fig. 1.10). Multipolar neurons are located deep in layer I and are characterized as non- or sparsely spiny, with axons projecting towards layers II and III providing feed-forward inhibition (Finch et al., 1986). They are often positively stained against Calretinin and GABA, with a minority fraction of Calretinin-positive cells that are glutamatergic or Calbindin-positive (Wouterlood, Mugnaini et al., 1985; Wouterlood, Denderen et al., 2000). In contrast, horizontal cells are located between layer I and II. The elongated somata of horizontal cells extend laterally, with their nearly spine-free dendrites within layer I and II. Their axons travel towards the hippocampus (Germroth et al., 1989; Schwerdtfeger et al., 1990; Canto, Wouterlood et al., 2008). These cell types cannot be distinguished based on electrophysiological recordings/properties and are grouped together. Layer I neurons respond with a sag to hyper- and depolarizing current injections, resulting in a prominent rebound potential. They have a lower input resistance than layer III neurons, leading to a significantly shorter time constant (tau). Principal layer I neurons also elicit depolarizing afterpotenials, which are larger compared with layer III neurons (Canto and Witter, 2012).

1.3.2 *Layer II*

Layer II of the mEC is mainly composed of two major excitatory principal cell types, namely stellate cells (SC) and pyramidal cells (PC) , shown in Figure 1.10 (Alonso and Klink, 1993). Two intermediate cell groups and six

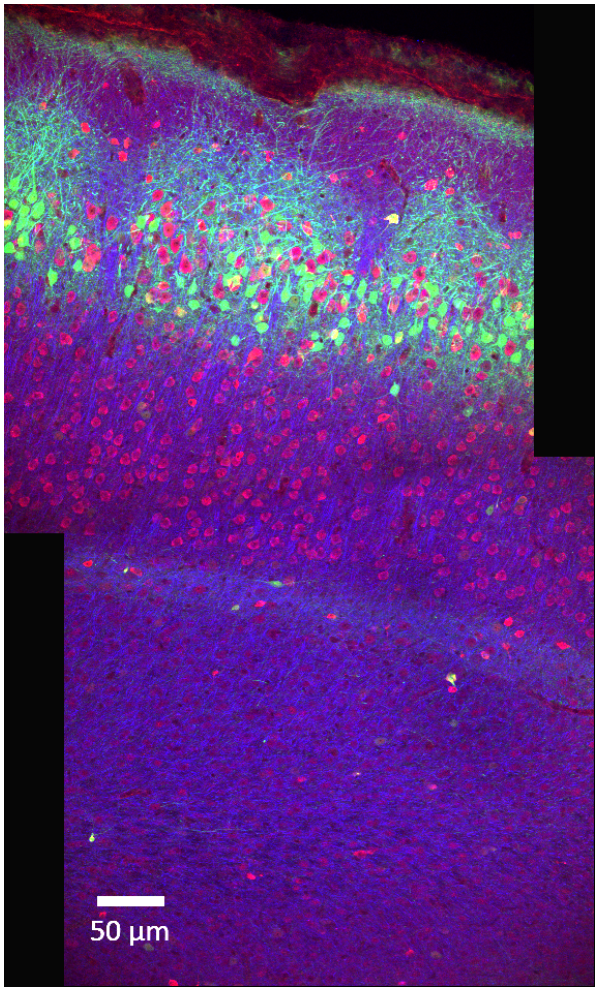

Figure 1.10: Layers of the mEC: neurons are stained against MAP2 (blue), Reelin (red) and Calbindin (green). Two confocal images of sagittal sections were stitched.

main subgroups of interneurons have also been discovered (Canto and Witter, 2012; Fuchs et al., 2016; Ferrante, Tahvildari et al., 2017).

Stellate cells

Alonso and Klink discovered these two cell types in 1993 and characterized their electrophysiological properties in detail using in vitro recordings. Similarly to layer I cells, SCs display a prominent sag as a response to hyper- or depolarizing current steps mediated by hyperpolarization-activated cur-

rents (Ih) (Alonso and Klink, 1993; Dickson, Magistretti, M. H. Shalinsky et al., 2000; Nolan, Dudman et al., 2007; Linden and Lopes da Silva, 1998). In response to depolarizing current steps, SCs elicit rebound potential, often resulting in rebound spikes or bursts. As a consequence of this phenomenon, the mean first inter-spike-interval (ISI) is very short, with the second AP significantly smaller in amplitude than the first AP. A large fraction of SCs exhibit prominent depolarizing afterpotentials (DAPs), whereas a smaller fraction elicits DAPs with very small, if at all detectable, amplitudes Alessi et al. (2016). Depolarization induces persistent membrane potential oscillations Canto and Witter (2012). Injecting sinusoidally modulated currents reveal subthreshold resonance properties at stimulus frequencies in the theta range which may play a role in frequency-dependent information flow (Alonso and Klink, 1993; Erchova et al., 2004; Canto and Witter, 2012; Alessi et al., 2016).
SCs comprise the major cell type of layer II and are distributed throughout this layer. These cells are characterised by 2 to 11 spiny primary dendrites, which project from the apex and the sides of the soma towards the pia and horizontally double the length of PC dendrites. The axon of SCs is more than double the thickness of that of PCs and gives off collaterals, which travel from the soma towards the angular bundle, projecting via the perforant path to the dentate gyrus granule cells and to CA3 pyramidal cells. The difference in axonal diameter suggests a faster action potential propagation from SCs to the DG/CA3 than via PCs (Schwartz and Coleman, 1981; Klink and Alonso, 1997; Canto and Witter, 2012).
Varga et al. (2010) identified two cellular markers, Calbindin and Reelin, which specifically label PCs and SCs (see Fig. 1.10), respectively. These findings further support the existence of at least two types of principal neurons.

Pyramidal cells

In contrast, PCs display neither membrane oscillations nor strong resonance frequencies. Most PCs exhibit a prominent sag. PCs without a sag in response to hyperpolarizing currents also do not show a sag response to depolarizing currents, leading to small rebounds and to delays in response to weak depolarization. The majority of PCs elicits a small DAP (Alonso and Klink, 1993; Linden and Lopes da Silva, 1998; Canto and Witter, 2012; Alessi et al., 2016). PCs differ significantly from SCs in terms of morphology, in that they have a pyramidally shaped soma with one apical dendrite traveling towards the pia and branching in layer II and I. Basal dendrites spread within layer II and also extent towards layer III. The main axons of PCs project to CA1 with collaterals to the angular bundle and to layer I-III (Canto and Wit-

ter, 2012; Witter, Doan et al., 2017; Canto, Wouterlood et al., 2008; Kitamura et al., 2014).
As mentioned above, PCs are typically Calbindin-positive. In addition to Calbindin, Kitamura et al. (2014) and reported that PCs stained positively for Wolframin syndrome 1 (Wfs1) as another specific marker in rats.

Intermediate cells

Two other principal neuron types have been reported in layer II: intermediate cell groups in between SCs and PCs. Intermediate SCs (IMSCs) express Reelin with a minority co-expressing Calbindin. In turn, different varieties of intermediate PCs (IMPCs) have been found: Calbindin-positive, Reelin-positive and Reelin and Calbindin positive (Fuchs et al., 2016; Witter, Doan et al., 2017). IMPCs have pyramidally shaped somata, horizontally tilted with one main spiny apical dendrite reaching towards the pia (Canto and Witter, 2012). The soma perimeter and number of primary dendrites also differ significantly from that of SCs and PCs (Fuchs et al., 2016).
Fuchs et al. (2016) could identify the four principal cell types based on one morphological and four diverse electrophysiological properties: the presence of a hyperpolarizing and depolarizing sag potential, a ratio of ISI1/2, the presence of a depolarizing afterpotential, the latency to first spike, the presence of a main (apical) dendrite. However, IMSCs differ from SCs in that they display a longer latency to the first spike In addition, IMPCs exhibit a very clear depolarizing after potential compared to PCs.

Interneurons

Inhibitory interneurons are thought to influence all cortical functions (Tahvildari, Wölfel et al., 2012). While the data on EC interneurons is limited, three recent studies revealed 3-6 interneuron subgroups in the superficial layers I-III of the EC (Tahvildari, Wölfel et al., 2012; Fuchs et al., 2016; Ferrante, Tahvildari et al., 2017). The different interneurons can be distinguished based on their morphology, projection sites, immunohistochemical markers such as calcium-binding proteins, intrinsic membrane properties and others. The six subgroups of inhibitory interneurons are referred to fast-spiking/PV^+/$RCan2^+$ (FS), Somatostatin (SOM), neuropeptide Y with neuro-gliaform (NPY-NGF), neuropeptide Y with no neuro-gliaform (NPY-Non-NGF), vasoactive intestinal peptide (VIP) and 5HT3a receptor containing interneurons (5HTR3a).

While FS interneurons are generally Parvalbumin-positive (PV^+), some are cholecystokinin-positive. FS interneurons co-express the regulator of calcineurin2 ($RCan2^+$) and are mostly GABAergic (Tahvildari, Wölfel et al., 2012; Buetfering et al., 2014; Armstrong et al., 2016). These so-called basket or chandelier cells (McCormick et al., 1985) are multipolar with 3 to 6 dendrites and with dense axonal arbors, which spread within the same layer. Intrinsic membrane properties differentiate this cell type from the others, as shown by the most strongly hyperpolarized resting membrane potential (–78.5 $\pm$ 0.6 mV), the lowest input resistance (156 $\pm$ 8 MOhm), the shortest AP width (0.48 $\pm$ 0.02 ms) and a prominent delay of the first spike, characterizing them as delay fast-nonadapting (Ferrante, Tahvildari et al., 2017).

SOM interneurons display the morphological characteristics of Martinotti neurons with a very thick axon at the soma that thins progressively with branching. SOMs elicit Ih-dependent post-inhibitory rebound spikes in response to hyperpolarizing current steps. SOMs are also characterized by a fast-AHP and a depolarizing afterpotential after the spike. They also showed the most depolarized resting membrane potential (–70.7 $\pm$ 0.5 mV), a prominent sag potential and were low-threshold and adapted less than the other subgroups (Tahvildari, Wölfel et al., 2012; Fuchs et al., 2016; Ferrante, Tahvildari et al., 2017).

NPY-NGF interneurons are called 'NGF' as they display round somata and four to nine dendrites spreading within the same layer, characteristic morphological properties of c neurogliaform interneurons. They exhibit a delayed and regular-adapting firing pattern.

In contrast, NPY-Non-NGF interneurons display a typical low-threshold spiking pattern, post-inhibitory rebound spikes and APs are followed by a fast-AHP and a depolarizing afterpotential. NPY-NGF interneurons also differ significantly from non-NGF interneurons by virtue of their smaller AP amplitude, input resistance and tau. NPY-Non-NGF cells have polygonal somata with three to four primary dendrites extending into multiple different layers. The axon is less branched but projects to several layers as well (Tahvildari, Wölfel et al., 2012; Ferrante, Tahvildari et al., 2017).

VIP interneurons can be subdivided into two functional groups. The majority of VIP cells respond to depolarizing stimuli with a regular adapting firing pattern. Other VIP interneurons elicit an irregular adapting spiking pattern. In terms of intrinsic membrane properties, VIP interneurons have the highest input resistance (508 $\pm$ 43 MOhm), the slowest tau (38.5 $\pm$ 2.6 ms), the lowest AP amplitude (59.5 $\pm$ 1.2 mV) and the longest AP (width at half-height 1.19 $\pm$ 0.04 ms). Morphologically, VIP cells can be distinguished from other

interneurons by their bipolar/double-bouquet shape with basal dendrites projecting to layers I/II (Tahvildari, Wölfel et al., 2012; Ferrante, Tahvildari et al., 2017).

5HTR3a interneurons mostly exhibit a regularly adapting spiking pattern. Additionally, some 5HTR3a interneurons elicit post-inhibitory rebound spikes. Morphologically, 5HTR3a interneurons can be segregated into two groups: bipolar cell and multipolar cells (Tahvildari, Wölfel et al., 2012; Ferrante, Tahvildari et al., 2017).

1.3.3 *Layer III*

Canto and Witter (2012) performed a morphological analysis of layer III of the mEC and identified five different principal neurons. First, small spiny pyramidal neurons located throughout layer III, with the apical dendrite extending towards the pia and the basal dendrites extending to deeper layers. The axon projects towards the angular bundle and to CA1 and the Sub (Tahvildari and Alonso, 2005). Second, complex pyramidal neurons mainly located in the middle and deep areas of layer III, with two primary spiny apical dendrites and basal dendrites, which spread within layer III. The main axon projects towards the angular bundle and into the Sub. Third, multipolar neurons located in the middle and deep layer III, close to the PaS. The multipolar dendrites spread within layers III/II and the axon travels towards the angular bundle and occasionally also to the PaS. Fourth, SCs located in the superficial region of layer III with one frequently branching apical dendrite, a multipolar dendritic tree spreading within layer III and an axon projecting towards the angular bundle. Fifth, the bipolar complex pyramidal neuron possesses up to two apical dendrites reaching towards the pia, one main basal dendrite spreading horizontally within layer III and the main axon projects towards the angular bundle and branches within layer III.

Interestingly, morphological layer III neurons types do not differ significantly in their intrinsic membrane properties (Canto and Witter, 2012). Layer III neurons do not display resonance or subthreshold membrane oscillations (Dickson, Mena et al., 1997; Canto and Witter, 2012). In contrast to layer II neurons, they display a very small sag, no rebound potential, no depolarizing afterpotential. Their APs are also significantly broader compared to layer II neurons and they start firing with a delay (Linden and Lopes da Silva, 1998; Canto and Witter, 2012).

1.3.4 *Microcircuits*

Since the discovery of grid cells, it has become increasingly important to characterize the neuronal circuitry that encodes spatial representation. As described in subsection 1.1, the connections from the EC to other areas and back are well known (Steward, 1976). In turn the intrinsic microcircuit of the main principal cells in the superficial mEC layers is largely unknown and has been the subject of a lot of discrepancy and further investigation (Winterer et al., 2017; Armstrong et al., 2016; Fuchs et al., 2016; Buetfering et al., 2014; Couey et al., 2013; Beed et al., 2010; Varga et al., 2010).

The most recent study from Winterer et al. (2017) focused on the excitatory microcircuits in layers II/III of the mEC and found some intra- and inter-laminar connections (Köhler, 1986). Within layer III, PCs contact other layer III PCs, but a higher number of layer III PCs exhibit largely unidirectional feedforward connectivity with layer II SCs. Excitatory connections within layer II were only shown between SCs and between PCs and SCs, but not between SCs to PCs, so that excitatory projections mainly converge onto SCs in layer II. They also found recurrent excitatory synaptic projections among layer III PCs and layer II SCs (Beed et al., 2010). In contrast to these findings, Couey et al. (2013) and Beed et al. (2010) reported that SCs are mainly interconnected via fast-spiking (FS) inhibitory interneurons and that no connectivity between FS interneurons and PCs could be found (Buetfering et al., 2014). Fuchs et al. (2016) could demonstrate that IMPCs and IMSCs are both inhibited by FS interneurons and receive excitatory input back from them. IMPCs and SCs receive inhibitory input from SOM interneurons, whereas SOM cells receive excitatory input from SCs, IMPCs and IMSCs and not from PCs. 5HTR3a interneurons were also found to inhibit all four principal neurons of layer II. Another study demonstrated that GABAergic FS interneurons innervate fewer Reelin-positive SCs and rather project more to Calbindin-positive PCs (Armstrong et al., 2016). Additionally, Varga et al. (2010) found cannabinoid type 1 receptor–expressing GABAergic basket cells (CCKBCs) which preferentially connect with Calbindin-positive PCs of layer II and avoid Reelin-positive SCs.

Bursts modulate neuronal processing and represent a typical spike firing pattern in vivo (Kandel and Spencer, 1961). A phenomenon which could support on the formation of bursts is the depolarizing afterpotential (DAP) (Wong and Prince, 1981; Storm, 1987). The DAP arises as part of a triphasic postspike dynamic in the absence of applied current. It is preceded by a fast afterhyperpolarization (fAHP) and followed by a medium-rate afterhyperpolarization as illustrated in Figure 1.11. The fAHP corresponds to the fast repolarizing phase of the AP. The DAP appears as a depolarization of the membrane voltage of a few millivolts with a peak amplitude approximately 5-6 ms after the AP (Wong and Prince, 1981; Alonso and Klink, 1993; Storm, 1987). In the mEC a larger DAP was reported in SCs than in PCs which, could be due to different repolarization mechanisms in these principal cell types (Alonso and Klink, 1993). It was also observed that preceding hyperpolarization increased the DAP amplitude, sometimes eliciting an extra AP. This second triggered spike never caused another DAP (Linden and Lopes da Silva, 1998).

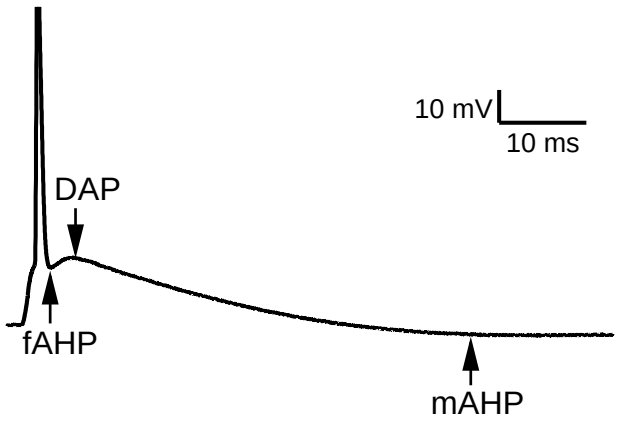

Figure 1.11: Voltage response elicited by a short depolarizing ramp current of two milliseconds shows an action potential followed by the fAHP, DAP and mAHP.

DAPs were found in different animals species and at distinct locations in the network of the nervous system. In different neurons, DAPs have different underlying mechanisms. One mechanism seen in pyramidal neurons of the electrosensory lateral line lobe in weakly electric fish, is the active backpropagation of spikes along the apical dendrite. Na^+ channels are dis-

tributed along the proximal apical dendrite and support the active back-propagation of somatic APs, which results in a DAP (Turner et al., 1994; Doiron et al., 2007). Additionally, the DAP of these cells can be modulated by voltage-gated K^+ channels and leak currents, which are expressed along the somato-dendritic axis (Fernandez, 2005; Mehaffey, 2005). In Aplysia, Kramer and Zucker (1985) proposed that in bursting pace-maker neurons DAPs are generated by a "Ca^{2+}-dependent activation of a voltage-independent non-specific cationic conductance". Hippocampal pyramidal neurons have attracted attention since the early 1960's, which accelerated after the discovery of place cells (Kandel and Spencer, 1961). Wong and Prince (1981) suggested that in CA3 PCs the DAP is due to a voltage-dependent inward Ca^{2+}-current. Some years later, Azouz et al. (1996) found that DAPs of CA1 PCs are mediated by a low voltage-activated, persistent Na^+-current. Additionally, in 2004 Yue and Yaari concluded from their experiments in CA1 that the DAP is also influenced by the KCNQ/M current. In the mEC Kispersky et al. (2010) additionally proposed that the DAP could be influenced by the M-current, and by an autapse, a fast recurrent connection, which enhances the DAP and facilitates firing. Alessi et al. (2016) could distinguish between two types of DAPs in the principal cells of mEC layer II. They demonstrated that at near-threshold the DAP is influenced by Na^+-currents in SCs as well as in PCs. SCs showed a second additional mechanism, which depends on Ca^{2+}-currents and which is present during membrane hyperpolarization (Alessi et al., 2016).

1.5 MEMBRANE POTENTIAL DYNAMICS

Another interesting phenomenon which was found during in-vivo patch-clamp recordings in mice navigating in virtual-reality environments was a strong correlation of grid field firing with slow depolarizing membrane potential ramps (5.0 ± 1.0 mV) as illustrated in Figure 1.12 (Domnisoru et al., 2013; Schmidt-Hieber and Häusser, 2013). These findings were observed in mEC layer II stellate cells and provide insights into how grid cell activity emerges from the interplay of synaptic inputs and cell-intrinsic dynamics (e.g. DAP). However, the intracellular theta oscillations influenced the grid cell spike timing, it was positively (but weak) correlated with the running speed (10 - 30 cm/s) and its phase comprises much more spatial information than spike rates (Domnisoru et al., 2013; Reifenstein et al., 2012).

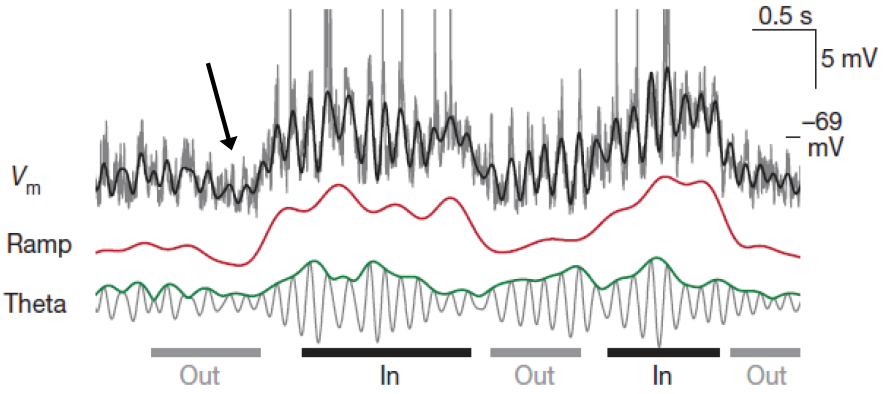

Figure 1.12: Whole-cell recording from grid cell in vivo. The membrane potential (grey, spikes truncated) could be decomposed into ramp (red) and theta components (grey) and was closely approximated by their sum (black overlay). Trace of the membrane potential illustrates the pre-hypolarization before the animal enters the grid field. Figure modified from Domnisoru et al., 2013, with permission.

1.6 THESIS AIMS

While a rodent explores its surroundings grid cells in the mEC encode the animal's location by eliciting firing fields that are arranged in a hexagonal pattern (see Fig. 1.13C). Grid cells exhibit distinct membrane potential phenomena proceeding at different time scales, such as theta-band oscillations, slow ramps and burst episodes with very short inter-spike-intervals (ISI) on the order of a few milliseconds (4 - 10 ms) (Alonso and Llinás, 1989; Dickson, Magistretti, M. Shalinsky et al., 2006; Giocomo and Hasselmo, 2007). Such short ISIs have received little attention but may contribute substantially to the encoding of spatial information, because of their occurrence in layer II of the mEC where the highest proportion of grid cells have been found and where most of the excitatory inputs converge (Hafting, Fyhn, Molden et al., 2005; Winterer et al., 2017; McNaughton, Battaglia et al., 2006).
The in vivo data of Latuske et al. (2015) show a high number of these very short ISIs (~25 % of all spikes), as illustrated in the ISI distribution (Fig. 1.13A) and the corresponding cumulative histogram (Fig. 1.13B) of one example grid cell. It seems that especially spikes with a preceding short ISIs cluster closer to the grid field centers (Fig. 1.13C). In addition, in vitro recordings of mEC layer II principal cells have demonstrated that the action potential is followed by a pronounced DAP. The channels underlying the

DAP, its biological function and its relation to other electrophysiological features are, however, poorly understood.

In the present thesis, we aim to corroborate the core hypothesis that DAPs underlie transient burst-like discharges in mEC cells and play an important role in the dynamics and the information processing of the entorhinal cortex. Therefore, the following approach was chosen:

1. Whole-cell patch recordings were performed on principal cells in mEC slices to elucidate the basic response properties of layer II neurons.
2. Detailed analysis of the DAPs in mEC layer II neurons: modulation, pharmacology and function.
3. Post-hoc immunohistochemical stainings of recorded cell were performed to investigate which serotype of mEC neurons corresponds to which kind of characteristic mEC cell response.
4. We carried out a quantitative cluster analysis on all measured cells in the rat to find different cell populations.
5. In a final step, we aimed at connecting in vitro data with in vivo data by partially mimicking the in vivo firing response in acute slices.

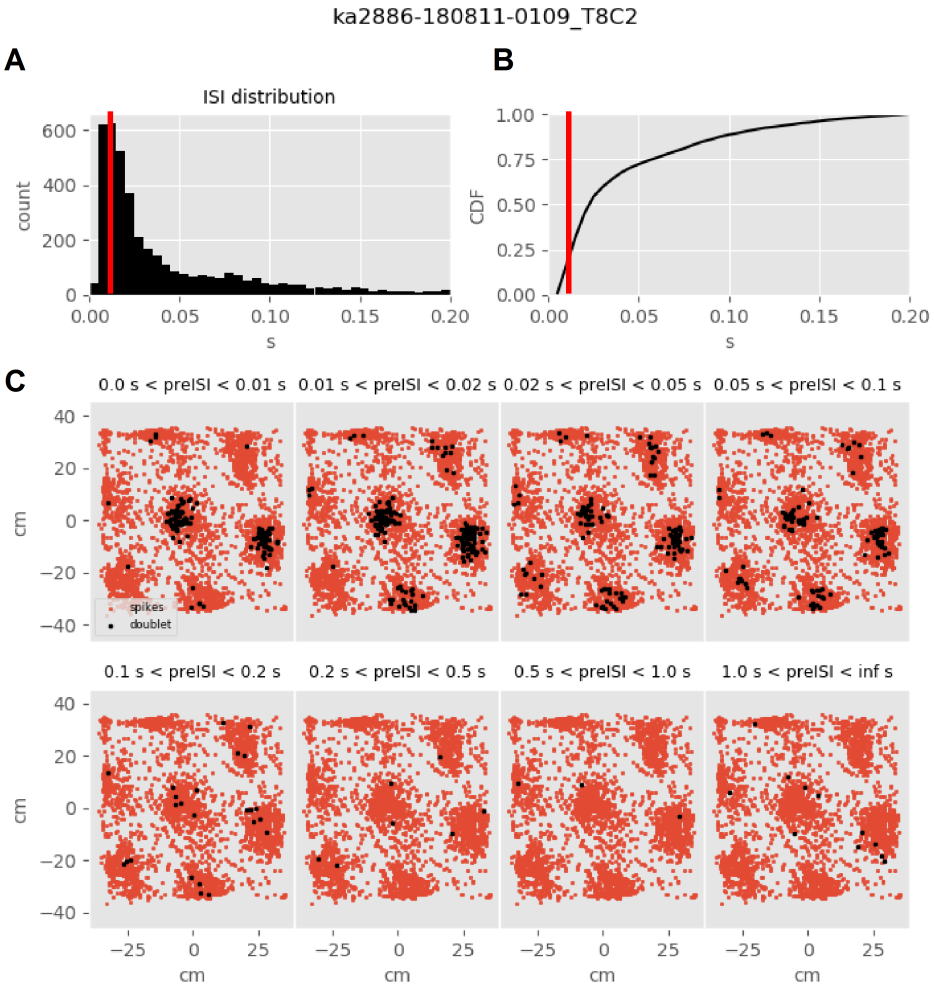

Figure 1.13: Plots showing short inter-spike-intervals of in vivo mouse data. (A) Histogram of the inter-spike-interval distribution of an example grid cell. Red line indicates 10 ms. (B) Corresponding cumulative histogram of the ISI distribution of this particular cell with the red line marking 10 ms. (C) Red dots represent the location of the animal at any given spike while the mouse is exploring its environment. Superimposed black dots illustrate the position of short ISIs with different preceding ISI conditions increasing from left to right and indicated in each title. This dataset was provided by courtesy of Latuske et al. (2015) and the figure was provided by courtesy of Dora Csordas.

2

MATERIAL AND METHODS

2.1 ANIMALS

Experiments were conducted either with Mongolian gerbils (*Meriones unguiculatus*) from a wild-type colony from the LMU animal facility or with Long-Evans rats purchased from Charles River Laboratories in Italy (Charles River Laboratories International, Inc.). After rats arrived they were allowed to acclimate to the new surrounding for at least four days to decrease the stress level before they were used for the experiments. Rats as well as Gerbils were housed in separate rooms together with their siblings in a 612 x 435 x 216 mm (internal floor area: 2065 cm^2, Typ 2000P) box, filled with wooden chipping and wooden wool as bedding. They were kept under constant laboratory conditions with a 12 hour light/dark cycle, 22 - 23 °C room temperature. The humidity in the rat room is around 50 - 55%, whereas it is a bit more arid in the gerbil room with 45%. Animals were allowed to eat ad libitum and had unrestricted water access. All experiments of this work complied with institutional guidelines, national and regional laws. Animal protocols were reviewed and approved by the Regierung of Oberbayern (according to the Deutsches Tierschutzgesetz).

2.2 PREPARATION

Sagittal and horizontal brain slices containing the mEC were prepared from postnatal day (P) 30-45 Mongolian gerbils and Long-Evans rats of either sex. Animals were anesthetized with isoflurane and rapidly decapitated. Brains were quickly removed and transferred to ACSF (artifical cerebrospinal fluid) containing (in mM) 50 or 120 sucrose, 25 NaCl, 27 $NaHCO_3$, 2.5 KCl, 1.25 NaH_2PO_4, 3 $MgCl_2$, 0.1 $CaCl_2$, 25 glucose, 0.4 ascorbic acid, 3 myo-inositol and 2 Na-pyruvat (pH 7.4 when bubbled with 95% O_2 and 5% CO_2). Brain slices of 400 µm were taken using a VT1200S vibratome (Leica Microsystems GmbH, Wetzlar, Germany) and incubated in recording solution (same as ACSF but with 125 mM NaCl, no sucrose, 1.2 mM $CaCl_2$, and 1 mM $MgCl_2$)

at 36 °C for 45 minutes.

2.3 ELECTROPHYSIOLOGY

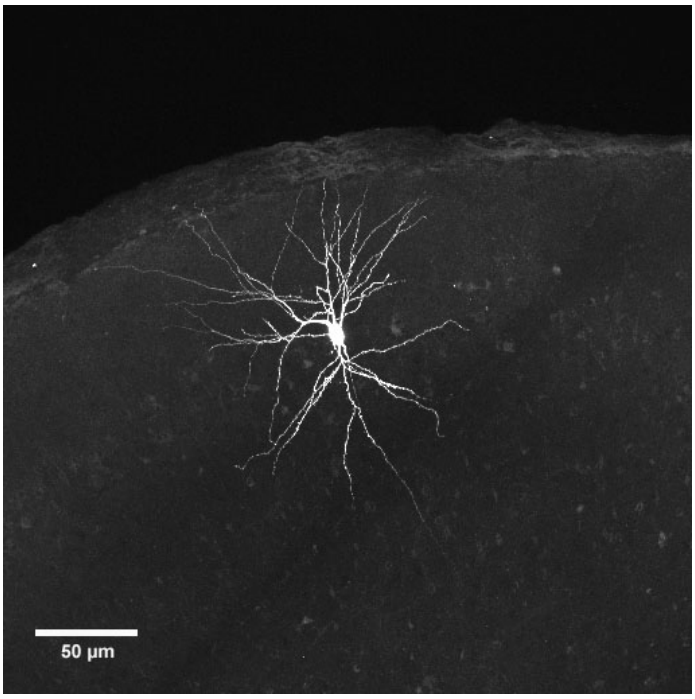

Figure 2.1: Maximum projection of a confocal stack of a recorded stellate cell of the mEC layer II filled with Alexa 594. This picture was taken after fixating the slice and mounting it on a slide.

After incubation slices were transferred to a recording chamber and continuously perfused with recording solution. Whole-cell recordings were acquired from visually identified mEC neurons of layer II using a CCD camera (TILL-Imago VGA). The TILL Photonics imaging system (Gräfelfing, Germany), a combination of a charge-coupled device camera and a monochromator (Polychrome IV), was mounted onto an upright microscope (BX50WI) with a 60 x 1 numerical aperture (NA) objective (Olympus, Center Valley, PA). The microscope was equipped with gradient contrast illumination (Luigs and Neumann, Ratingen, Germany) and a 1.4-NA oil-immersion condenser. Recordings were performed with an EPC10/2 amplifier (HEKA Elektronik, Lambrecht (Pfalz), Germany). All experiments were performed at physiolo-

gical temperature of 36 ± 1 °C , which was maintained by bath chamber (PH-1) and in-line (SF - 28) heaters (Warner Instruments, Biomedical Instruments) and controlled by a temperature sensor placed next to the slice. All recordings were performed with 3-3.5 MΩ filamented, fire-polished borosilicate glass electrodes (inner diameter: 0.86 mm; outer diameter: 1.50 mm, Harvard Apparatus Ltd., Edenbridge, Kent, UK), pulled with a horizontal multi-step puller (DMZ-Universal Puller, Zeitz Instruments, Martinsried, Germany) and heat-polished to guarantee a smooth tip. Electrodes were filled with internal solution and fixated to an electrode-holder/headstage, which was connected to a PatchStar Micromanipulator (ScientificaLtd., Uckfield, East Sussex, UK) to translate xyz direction, and to a manometer to control orally-generated pipette pressure. This positive pressure was applied to retain a clean pipette tip. The ground electrode and the electrode linking the headstage with the internal pipette solution were made of Ag/AgCl wire. For current-clamp recordings, an internal solution containing (in mM) 145 K-gluconate, 4.5 KCl, 15 HEPES, 2 Mg-ATP, 2 K-ATP, 0.3 Na-GTP, 7.5 Na2-phosphocreatin adjusted by adding KOH to pH 7.25 was used. To reconstruct and verify the location of recordings, cells were filled with 100 µM Alexa 594 added to the internal solution. During current-clamp recordings the bridge balance was compensated to 100% after estimation of the series resistance. The liquid junction potential (LJP = 17 mV, see Ammer et al., 2015) was not corrected for any of the solutions. Data were acquired at 20-25 kHz and filtered at 3 kHz. At the end of the recording pipette was slowly and carefully retracted until a sufficiently high resistance was reached to ensure the cell membrane re-sealed and to avoid damaging the cell. Finally slices were fixated in 4% PFA (paraformaldehyde) for 3 hours.
Different calcium currents were pharmacologically isolated with bath application of NNC 55-0396 dihydrochloride (20 µM, Tocris), Cadmium chloride (100 µM, 202908 Aldrich, 99.99% trace metals basis) or Nifedepine (50 µM, N7634 Sigma ⩾ 98% (HPLC) diluted in DMSO). Sodium currents were blocked with bath-application of TTX (0.03/0.04/0.08/2 µM, Tetrodotoxin). Hyperpolarization activated cation currents (I_h) were blocked with bath-application of ZD7288, (50 µM, M4-ethylphenylamino-1,2-dimethyl-6- methylaminopyridinium chloride).

2.4 STIMULUS GENERATION

Stimulus generation and data acquisition were executed primarily with the Patchmaster software (HEKA Elektronik, Lambrecht (Pfalz), Germany). The stimulus template of ZAP and sinus stimuli was generated with two other

programs (*Template Creator*, written by Christoph Krist, and IgorPro, from WaveMetrics, Lake Oswego, OR).

2.4.1 *IV stimulus*

A 500 ms current step of amplitude ranging from -150 pA to +800 pA was injected in 25 or 50 pA increments. These square current pulses were applied from the cell's resting potential. This protocol was used in all recordings as a standard protocol to obtain certain membrane characteristics.

2.4.2 *Stepper*

The stepper, another standard protocol, consisted of a 400 ms hyperpolarizing current step of -5 pA injected at the cell's resting membrane potential and repeated 60 times. The resulting voltage responses allowed the input resistance (R_{in}), the capacitance and the time constant to be approximated.

2.4.3 *Ramp*

The third standard protocol was a short depolarizing current ramp consisting of a short rising phase of 0.8 ms and a descending phase of 1.2 ms. The current was increased in 100 pA increments from the resting membrane potential until an action potential was elicited.

2.4.4 *ZAP generation*

To record ZAPs (impedance amplitude profiles) to estimate subthreshold resonance frequencies (Erchova et al., 2004), Christoph Kirst was so kind to write a program for this project, a Template Creator. The *Template Creator* was written in C^{++} and controls the Patchmaster by the "batch file control" protocol of HEKA (Heka, 2013). This program was used to generate sinusoidally frequency-modulated current stimuli whose frequency f(t) increased linearly in time. These current stimuli were conveyed to the Patchmaster software and applied to the cells:

$$I_{ZAP}(t) = a \cdot \sin(2 \cdot \pi \cdot f(t) \cdot t) \tag{2.1}$$

$$f(t) = fo + (f1 - fo) \cdot \frac{t}{2T} + off \tag{2.2}$$

For the time-dependent frequency of the ZAP current, we used a range from 0-20 Hz (f0 = 0Hz, f1= 20Hz) with a stimulus duration (T) of 30 seconds as in Schreiber et al., 2004. This was done to ensure the ZAP current changes slowly enough to obtain a precise estimation of the impedance. A standard current amplitude (a) of 0.1 nA was injected. By applying a constant offset current (off) the cell's membrane voltage could be adjusted to be either above or below spike threshold. The stimulation was repeated at least once. The recorded data were then transferred back from Patchmaster to the Template Creator and rapidly analyzed online for further experiments. This protocol was applied to all recorded cells as another standard protocol.

2.4.5 *Generation of sine-wave stimuli*

The generation of sinus stimuli was carried out in IGOR Pro (WaveMetrics, Lake Oswego, OR). Generated templates (e.g. stim.tpl) were transferred to the Patchmaster's pgf-folder. In the Patchmaster software the input had to be changed to "stimulus from template". Sinus stimuli (stim) consisted of a slow sinus half wave (stim1) superposed with a fast sinus wave (stim2).

$$\begin{aligned} \mathrm{stim1}(t) &= \sin(\pi \cdot t \cdot f1) \\ \mathrm{stim2}(t) &= \sin(2 \cdot \pi \cdot t \cdot f2) \\ \mathrm{stim}(t) &= \mathrm{amplitude1} \cdot \mathrm{stim1}(t) + \mathrm{amplitude2} \cdot \mathrm{stim2}(t) \end{aligned} \tag{2.3}$$

2.5 IMMUNOHISTOCHEMISTRY

Immunohistochemistry was carried out on brain sections from P30-P45 Long-Evans rats. Animals were quickly anesthetized with isoflurane followed by a deep anaesthesia using 200 mg/kg body wt pentobarbital (Narcoren, Merial GmbH, Hallbergmoos, Germany) via intraperitoneal injection. The animals were perfused transcardially with Ringer solution, supplemented with 0.1% heparin (Meditech Vertriebs GmbH, Parchim, Germany) for 5 min, followed by 4% PFA for 30 min. The brains were removed and postfixed in 4% PFA overnight at 4°C. Brains were washed three times in 0.1 M PBS (phosphate-buffered saline) (see table 2.1) and horizontal slices of 60 - 80 µm thickness were taken using a VT1200S Vibratome. Standard immunohistochemical procedures were performed on free-floating slices using the primary antibodies listed in Table 2.2.
After two days of incubation, the secondary antibodies were applied for 3 hours at RT and were conjugated with fluorescent dyes listed in Table 2.3.

The slices were then washed four times in 0.1 M PBS for 5 min. Finally, the sections were mounted with Vectashield medium (H-100; Vector Laboratories, AXXORA, Enzo Life Sciences GmbH, Lörrach, Germany).

0.1 M phosphate-buffered saline
Solution A: 27,22 g KH_2PO_4 (MW=136,09 g/mol) in 1 l H_2O dest.
Solution B: 35,67 g Na_2HPO_4 x 2 H_2O (MW=177,99g/mol) in 1 l H_2O dest.
Titrate: 100 ml Solution A + 400 ml Solution B + ca. 500 ml H_2O dest. => pH 7,4

Table 2.1: Phosphate-buffered saline 0.1 M

Antigen	**Host**	**Type**	**Dilution**	**Company**	**Cat.no**
MAP2	chicken	poly	1:1000	Neuromics	CH22103
Calbindin	rabbit	poly	1:500	Swant	CB38
Calbindin	mouse	mono	1:500	Swant	300
Reelin	mouse	mono	1:500	Millipore	MAB5364
Calretinin	mouse	mono	1:500	Swant	6B3
Calretinin	rabbit	poly	1:500	Swant	7699/3H
Parvalbumin	rabbit	poly	1:500	Swant	PV 28
WFS1	rabbit	poly	1:500	ProteinT	11558-1-AP

Table 2.2: Primary antibodies

To stain electrophysiologically recorded cells, free-floating slices used for recordings were fixated for 3 hours in 4% PFA, after which standard immunohistochemistry procedures were performed. Slices were washed four times in PBS for five minutes at RT. Sections were then blocked in blocking solution (0.3% Triton, 0.1% saponin, 1% BSA in PBS) for 1 hour on a shaker at RT and then incubated for 48 h at 4 °C on a shaker using primary antibodies against the calcium binding proteins Calbindin and the extracellular matrix protein Reelin diluted in blocking solution. Slices were then washed four times in PBS again for five minutes at RT, followed by the application of the secondary antibodies conjugated with Alexa 488 (Donkey-α Rabbit) and Alexa 647 (Donkey-α mouse), also diluted in blocking solution, for two days at 4 °C on a shaker. Finally, the slices underwent the same washing procedure as before and were mounted in Vectashield medium.

Antigen	Conjugate	Host	Dilution	Company	Cat.no
α-rabbit	Alexa 488	donkey	1:200	Mol. Prob.	A21206
α-mouse	Alexa 488	donkey	1:200	Mol. Prob.	A21202
α-mouse	Alexa 647	donkey	1:200	Dianova	715606150
α-chicken	AMCA	donkey	1:100	Dianova	703156155
α-mouse	Cy3	donkey	1:400	Dianova	715166151
α-mouse	Cy3	donkey	1:400	Dianova	715156155
α-rabbit	Cy3	goat	1:100	Dianova	111165144
α-goat	Cy5	donkey	1:100	abcam	Ab6566
-	Nissl (640/660)	-	1:100	Mol. Prob.	N21483

Table 2.3: Secondary antibodies

2.6 CONFOCAL MICROSCOPY

To image immunohistochemical stainings, confocal optical sections were obtained with a Leica 6000CS SP5-2 confocal laser- scanning microscope (Leica Microsystems, Mannheim, Germany) equipped with a 10x 0.3 NA and 20x 0.7 NA oil immersion objective. Fluorochromes were visualized by using an UV laser with an excitation wavelength of 405 nm (emission 410–430 nm for AMCA), an argon laser with an excitation wavelength of 488 nm (emission 494– 555 nm for Alexa 488), a DPSS laser with a excitation wavelength of 561 nm (emission 565–606 nm for Cy3) and a helium-neon laser with an excitation wavelength of 633 nm (emission 640–740 nm for Alexa 647/Cy5/Nissl (640/660)). For each optical section the images were recorded sequentially for the different fluorochromes. To obtain an improved signal-to-noise ratio, each section image was averaged from six serial line scans. The voxel size was either 3033.3 x 3033.3 x 2056.1 nm (10x objective) or 1516.6 x 1516.6 x 629.4 nm (20x objective). The image size was 512 x 512 pixels. After stack acquisition, we used a custom plugin for ImageJ (NIH) written by Dr. Boris Joffe to correct the chromatic aberration-induced Z shift between color channels. The images illustrated in the figures are maximum-intensity projections which were assembled using ImageJ 1.37k plugins as well as Adobe Photoshop 8.0.1 (Adobe Systems, San Jose, CA) software.

Data were processed and analyzed in IGOR Pro (WaveMetrics, Lake Oswego, OR), Matlab (MathWorks Inc., Natick, MA, USA) and mecPhysio (custom-made, self-written program by Johannes Nagele). Statistics were calculated with Prism 7 (Graphpad Software Inc., La Jolla, CA, USA). Group data are presented as mean ± standard deviation. The sample size of cells (n) is indicated in the summary tables. Data were screened for normal distribution with the Kolmogoro-Smirnov test and were then tested either by the parametric paired/unpaired t-test or by the non-parametric Mann-Whitney U test.

2.7.1 *Analysis of electrical resonance*

The analysis of electrical resonance responses to Zap stimulations was performed as described in Erchova et al. (2004) and Schreiber et al. (2004). First the impedance (Z) was calculated as the ratio between the Fast Fourier Transform (FFT) of the voltage signal (measured cell membrane voltage = out) divided by the Zap stimulus (injected current = in):

$$Z(f) = \frac{fft_{out}(f)}{fft_{in}(f)} \tag{2.4}$$

The impedance consists of a real and an imaginary part

$$Z(f) = Z_{real}(f) + iZ_{imaginary}(f) \tag{2.5}$$

To estimate the resonance frequency the acquired impedance curve was then fitted with an electrical two parallel branches RCL circuit model with 4 fit parameters (a,b,c,d) (Erchova et al., 2004; Schreiber et al., 2004).

$$|Z(f)|^2 = \frac{a + b \cdot f^2}{f^4 + c \cdot f^2 + d} \tag{2.6}$$

The resonance frequency ($f_{resonance}$) can then be calculated as the maximum of the impedance fit (see Figure 3.1):

$$f_{resonance} = \sqrt{-\frac{a + \sqrt{a^2 - a \cdot b \cdot c + b^2 \cdot d}}{b}} \tag{2.7}$$

Frequencies of 1 Hz and less were excluded for the fits to avoid errors. $F_{resonance}$ for cells with low-pass properties was set to 0 Hz. Another characterizing measurement for resonators is the Q value, which displays the sharpness of the resonance. It is computed as the ratio between the impedance at the resonance frequency and the impedance at 0 Hz (Schreiber et al., 2004):

$$Q = \sqrt{\frac{|Z_{max}|}{|Z_0|}} \tag{2.8}$$

2.7.2 *Cluster analysis*

For clustering the recorded cells into different subpopulations we decided on a heuristic quantitative cluster analysis. This analysis was performed by Johannes Nagele who first started with a cross-validated factor analysis to get the optimal number of features which should be used for the clustering. Based on that we selected seven electrophysiological measurements, representing passive and active membrane properties which explain a large ratio of variance (~80%). On these selected features a k-means clustering was performed. K-means clustering is a method to partition n data points into k clusters. Each data point is assigned to the cluster with the nearest mean (Steinhaus, 1956). Here we used the Euclidean distance and repeated 50 times by randomly performing k-means clustering on 50% of the data to ensure convergence. For each of the results of such clustering a "Silhouette" (Rousseeuw, 1987) and a "Similarity" score were computed. The silhouette score is a measurement of similarity/dissimilarity of a cell to the other cells within its own cluster and across clusters. For a given cell i, it is calculated as

$$s(i) = (b(i) - a(i))/\text{maximum}[a(i), b(i)], \tag{2.9}$$

where a(i) is the average distance between cell i and all other cells in its cluster and b(i) is the mean distance between cell i and all cells that are in the cluster closest to i's cluster. The results can range from -1 to 1, with a high score indicating a high similarity within the cluster and a low score indicating less similarity within the cluster. We augmented the silhouette scores by computing average pairwise adjusted Rand indices between the clusterings. The Rand index is a standard measurement in data clustering to quantify the similarity between two data clusters (Rand, 1971). By comparing these two scores a optimal number of clusters was estimated (C = 4). With

this optimal cluster number the k-means was repeated on all data to get a cluster score for each cell.
In addition to the k-means clustering a hierarchical Ward clustering was used to validate the clustering (Ward Jr., 1963).
For both clustering procedures z-score normalized values (based on mean and standard deviation of each feature) were used to avoid potential biases due to variance differences along the different parameter axes.

3

RESULTS

3.1 BASIC PROPERTIES OF MEC CELLS

Whole-cell current-clamp recordings were performed to characterize different in vitro sub- and supra-threshold response properties of MEC layer II neurons, as described previously in several experimental studies (Alonso and Klink, 1993; Linden and Lopes da Silva, 1998; Erchova et al., 2004). Firstly, the resting membrane potential (E_{rest}) was estimated by averaging the membrane potential during 200 ms in the absence of any current injection (see Methods 2.4.1). Secondly, we used an IV protocol (see Methods 4.1) to measure the sag: which is an undershoot that characterizes the voltage response to a hyperpolarizing current injection (in this case, -150 pA). The sag was calculated as the voltage difference between the mean membrane potential at steady state (last 200 ms) and the maximum membrane potential hyperpolarization (Fig. 3.1 A). MEC layer II cells were stimulated with the Stepper protocol (see Methods 2.4.2) to determine the input resistance, the membrane time constant and the membrane capacitance. A small current injection (-5 pA, 400 ms) was applied to elicit a change in membrane potential. The input resistance was calculated by dividing the average membrane potential deflection (60 repetitions) to the applied current. To calculate the membrane time constant, the mean voltage response was fitted from the stimulation start to peak hyperpolarization with a single-order exponential function. The membrane capacitance was estimated by dividing the membrane time constant by the input resistance (Fig. 3.1 B). We used a ZAP stimulus (Methods 2.4.4), a sinusoidally modulated current injection from 0-20 Hz, to determine whether the cell membrane potential (Fig. 3.1 C) displayed a resonance at a certain frequency. The resonance frequency was calculated as described in the Method section 2.7.1. The maximum of the fitted impedance curve was measured and labeled as $f_{resonance}$, as shown in Figure 3.1 D. Finally, the voltage threshold was estimated by injecting a short current ramp (Methods 2.4.3). The voltage threshold was defined as the inflection point and was determined manually (Fig. 3.1 E). The analysis of these measured cell properties aims to characterize different cell populations and to find differences in the cells of the two measured animal species.

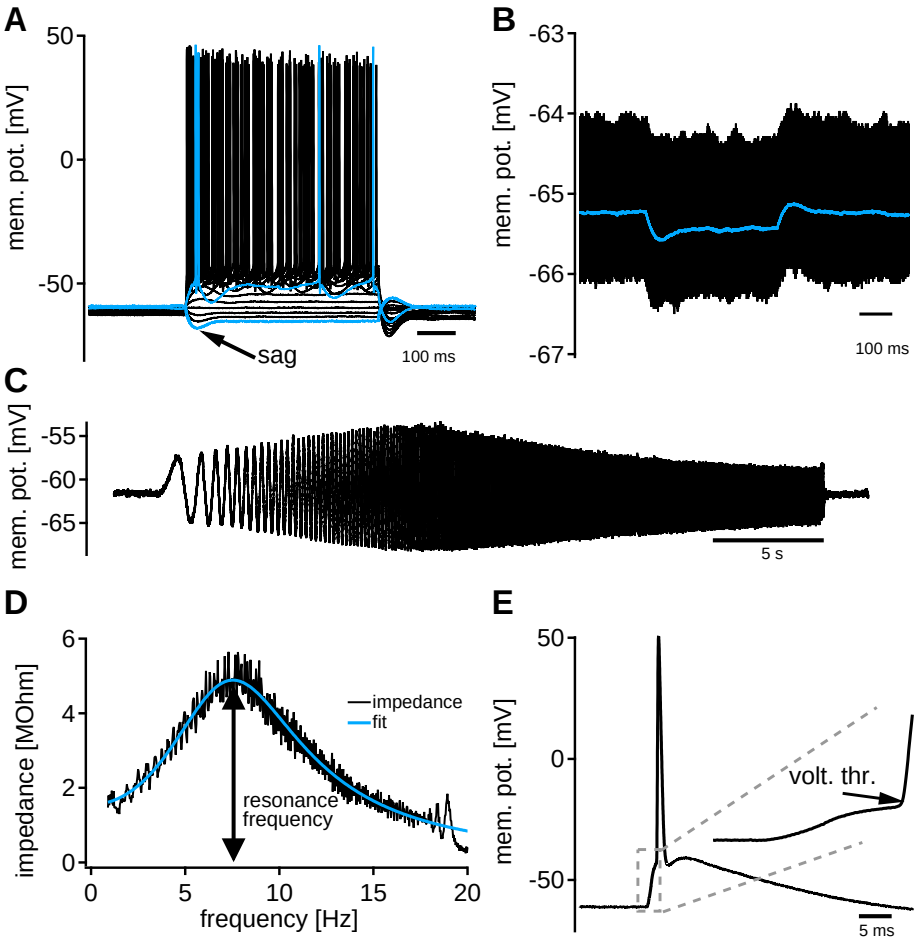

Figure 3.1: In-vitro membrane response properties of MEC layer II cells in response to current-clamp stimulations of different standard protocols. (A) Membrane potential in response to step current injections, indicating the sag as a basic characteristic. Step current injections from -150 pA up to +800 pA lasted 500 ms. (B) Membrane responses in response to a 400 ms hyperpolarizing current step of -5 pA injected at the cell's resting membrane potential and repeated 60 times. The blue trace illustrates the mean membrane potential deflection based on which the input resistance and the membrane capacitance were estimated. (C) Membrane potential in response to a ZAP stimulation (0-20 Hz) lasting 30 seconds. (D) Estimation of the resonance frequency ($f_{resonance}$), which was calculated from the impedance at different frequencies and measured as the maximum of the fitted curve. (E) Example voltage deflection in response to a short current injection that elicits an AP. The magnification indicates the corresponding voltage threshold.

Cumulative histograms show the aforementioned cell properties for both animal species measured in this study: gerbils (red) and rats (black) (Fig. 3.2). Cells are not yet clustered into different groups. All characteristics were tested for normality using the Kolmogorov–Smirnov test. Table 3.1 gives an overview of the characteristics as mean values $\pm$ standard deviation (SD). We further considered the differences between both species, which are already revealed in the histograms for some parameter. The non-parametric Mann-Whitney test was used to compare both groups and to find differences or similarities. All properties were significantly different between both species at the 5% level, except for the resting membrane potential and the sag potential (Fig. 3.2 A and D). Differences in the properties between gerbils and rat were not unexpected and a reasonable explanation could be the difference in body size.

In Figures 3.2 G-I, the data of different properties are displayed as scatter plots against the sag potential to see if some properties correlate with each other as indicated by earlier publications (Nolan, Dudman et al., 2007; Canto and Witter, 2012). The majority of cells seems to elicit sag responses within a relatively small range (between 0 and -5 mV), whereas the distribution of the resonance frequency and the input resistance are much broader. Indeed, in both species the sag correlates significantly with the resonance frequency and the input resistance. The resulting p values of the computed Spearman correlations are listed in Table 3.2. The voltage threshold did not correlate with the sag potential.

Histograms and scatter plots indicate that different cell populations can potentially be separated. For example, Figure 3.2 E shows the distribution of the resonance frequency and could be separated into a group without (PCs or interneurons) and a group with a resonance frequency (SCs). But clustering into different cell populations proved to be more difficult than what is described in the literature and therefore a quantitative cluster analysis was performed which will be described in a later section (see Section 3.7).

We were primarily interested in the depolarizing afterpotential (DAP) in these cells and based on this special interest this DAP was analysed into detail in the following sections.

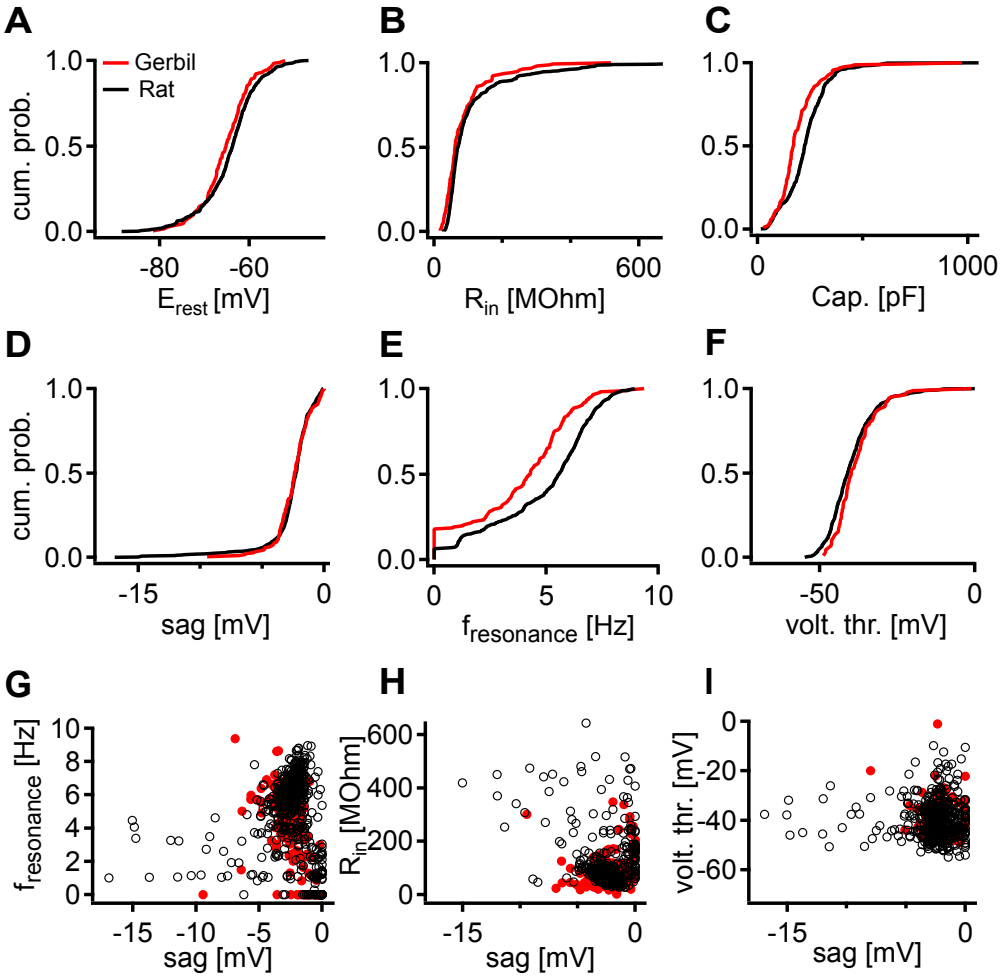

Figure 3.2: Cumulative histograms of the basic properties of MEC layer II cells (A-F). Scatter plots of resonance frequency, input resistance and the voltage threshold plotted against the sag (G-I). Data measured in rats are shown in black, data measured in gerbils are shown in red. Corresponding cell numbers (=n) are listed in table 3.1

Char.	Rat		n =	Gerbil		n =	p value
E_{rest}, mV	-64.4	± 6.35	531	-64.6	± 6.27	182	0.2610
R_{in}, MΩ	108.4	± 108.8	502	128.1	± 84.8	163	< 0.0001
Cap., pF	229.2	± 106.7	524	191.6	± 110	163	< 0.0001
sag, mV	-2.5	± 2.1	528	-2.5	± 1.82	179	0.3973
$f_{resonance}$, Hz	4.9	± 2.3	511	3.9	± 2.1	155	<0.0001
volt. thr., mV	-39.9	± 7.6	496	-38.1	± 7.4	85	0.0214
tau, ms	19.4	± 11.8	501	21.7	± 14	162	0.0124
AP width, ms	0.77	± 0.174	531	0.839	± 0.180	181	< 0.0001

Table 3.1: Electrophysiological parameters of MEC layer II cells. Values represent the mean ± SD and the corresponding number of cells (n) that were measured for rats and gerbils. E_{rest}, resting membrane potential; R_{in}, input resistance; Cap., membrane capacitance; $f_{resonance}$, resonance frequency; volt. thr., voltage threshold; tau, time membrane constant; AP width, action potential half width. All characteristics were first tested for normality using the Kolmogorov–Smirnov test. As none of the properties were found to be normally distributed, the non-parametric Mann-Whitney test was applied to compare both animal groups. Significance level: $p < 0.05$.

Condition	corr.	sign. level p < 0.05	p value
Rat			
Sag vs. $f_{resonance}$	-0.0871	yes	0.0495
Sag vs. R_{in}	-0.1685	yes	0.0002
Sag vs. volt. thr.	-0.03008	no	0.5052
Gerbil			
Sag vs. $f_{resonance}$	-0.4345	yes	<0.0001
Sag vs. R_{in}	0.2013	yes	0.0107
Sag vs. volt. thr.	0.02062	no	0.8514

Table 3.2: Correlations of some basic electrophysiological parameters.

3.2 CHARACTERIZATION OF THE DEPOLARIZING AFTERPOTENTIAL IN PRINCIPAL NEURONS OF MEC LAYER II

The depolarizing afterpotential (DAP) is an intrinsically generated phenomenon that arises after a single AP. The DAP occurs between a fast afterhyperpolarisation (fAHP), the AP fast repolarizing phase, and a medium-rate afterhyperpolarization (mAHP) (the slow recovery phase of the membrane potential toward the resting potential) as illustrated in Figure 1.11 and 3.3. The DAP manifests itself as a depolarization of a few millivolts, peaking approximately 5-6 ms after the peak of the AP (Alonso and Klink, 1993).

Our first goal was to examine different properties of DAPs in MEC layer II cells. Therefore, single APs were elicited close to the threshold using a 2 ms current ramp increasing in 100 pA increments (Methods 2.4.3). Two characteristics were defined from the resulting DAPs: DAP deflection and DAP width. The DAP deflection was calculated as the voltage difference between the DAP maximum and the fAHP trough (the minimum between AP maximum and DAP maximum), as shown by the arrow in the magnified inset in Figure 3.3 A. The DAP width was computed as the time window between the fAHP trough (see dotted arrow in Fig. 3.3 A) and the point at which the declining phase of the DAP reached half-maximum (= (membrane resting potential - DAP maximum potential)/2)), as indicated by the horizontal arrow in Figure 3.3 A. In addition, the time between AP maximum and DAP maximum was also calculated ($\text{timepoint}_{\text{DAP}}$-$\text{timepoint}_{\text{AP}}$).

Char.	Rat		n=	Gerbil		n=	p value
DAP defl., mV	2.6	± 1.54	426	1.36	± 0.98	44	<0.0001
DAP width, ms	17.4	± 6.48	417	18.3	± 7.02	43	0.3427
AP-DAP, ms	3.83	± 1.7	426	3.5	± 0.97	44	0.0691

Table 3.3: Electrophysiological characteristics and statistics of DAPs of MEC layer II cells. Values represent the mean ± SD, the measured cell number (n) for both species and the p value calculated by the Mann-Whitney test. Significance level: $p < 0.05$.

Cumulative histograms show the distribution of DAP deflection and DAP width. The Kolmogorov–Smirnov test revealed that the data were not normally distributed. Figure 3.3 B shows a difference in the DAP deflection between gerbil and rat data, which was shown to be statistically significant (Mann-Whitney test) (Tab. 3.3). However, the DAP width and the timing

between AP and DAP are not significantly different between both species (Fig. 3.3 C). Correlations between DAP deflection or DAP width and some basic electrophysiological parameters such as membrane resting potential, resonance frequency and the timing between AP and DAP, as illustrated in Figure 3.3 D-I, were calculated with the Spearman correlation (Tab. 3.4). The results of the data obtained in rats demonstrate that the DAP deflection correlates significantly with the resonance frequency as well as with the timing between AP and DAP. This shows that in cells with bigger DAP deflections the DAP maximum shifts to later time points. The same is true for gerbil data, with however, only a correlation with the AP to DAP timing. The DAP width in rats correlates with the resonance frequency, the membrane resting potential and the timing between AP and DAP. The DAP width in gerbils only correlates significantly with the AP to DAP timing.

Differences between rats and gerbils were also expected. The variation of the DAP deflection could be again attributed to the difference in body size which can be related to the cell size. In the scenario comparing bigger cells with smaller cells we would assume that bigger cells have a higher capacity than smaller cells which could have an impact on the DAP.

In addition, the data also may indicate at least two cell populations: one with DAP and resonance frequency which could correspond to the typical stellate cell and another without DAP and without resonance frequency corresponding to pyramidal cells (see Fig. 3.3 F). We wanted to test whether we could predict the presence or absence of a DAP from other electrophysiological parameters. This will be described in Section 3.7. But first we wanted to analyze the DAP in more detail.

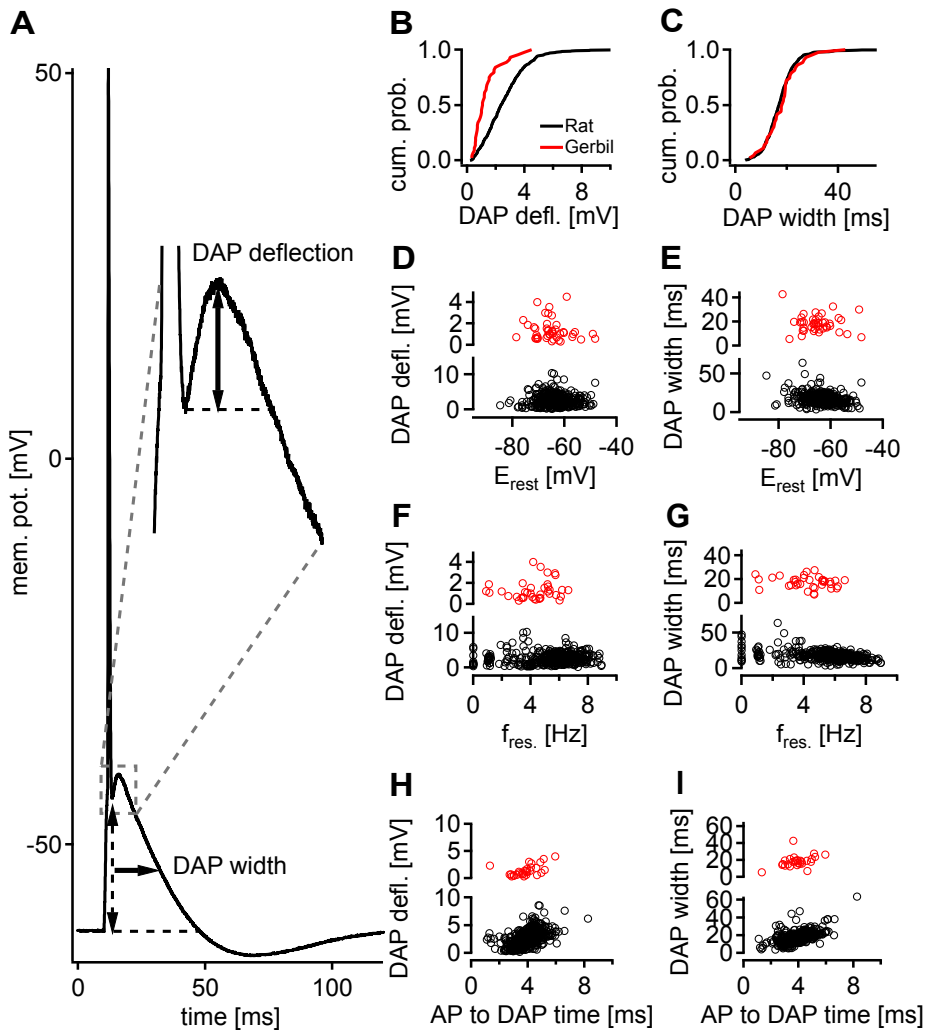

Figure 3.3: Basic properties of DAPs in MEC layer II cells. (A) Single AP elicited by a short current ramp increasing for 0.8 ms and decreasing for 1.2 ms, followed by a DAP. Arrows and magnified inset illustrate the two defined DAP characteristics: DAP deflection and DAP width. (B-C) Cumulative histograms of DAP deflection and DAP width in both species. Gerbil data are coloured in red and rat data in black. (D/F/H) Scatter plots with DAP deflection in relation to other characteristics of MEC II cells, such as membrane resting potential, resonance frequency and the time interval between AP maximum and DAP maximum. (E/G/I) Same characteristics for the DAP width.

Condition	corr.	sign. level $p < 0.05$	p value
Rat Defl. vs. E_{rest}	-0.055	no	0.2540
Rat Defl. vs. $f_{resonance}$	0.15	yes	0.0024
Rat Defl. vs. AP-DAP.	0.6	yes	< 0.0001
Rat Width vs. E_{rest}	-0.25	yes	< 0.0001
Rat Width vs. $f_{resonance}$	-0.37	yes	< 0.0001
Rat Width vs. AP-DAP	0.602	yes	< 0.0001
Gerb. Defl. vs. E_{rest}	-0.188	no	0.2215
Gerb. Defl. vs. $f_{resonance}$	0.157	no	0.3217
Gerb. Defl. vs. AP-DAP.	0.6	yes	0.0005
Gerb. Width vs. E_{rest}	-0.029	no	0.8528
Gerb. Width vs. $f_{resonance}$	-0.23	no	0.1691
Gerb. Width vs. AP-DAP	0.41	yes	0.0286

Table 3.4: Correlations between DAP deflection or DAP width and some basic electrophysiological parameters. Because of non-normal distributions the Spearman correlation test was applied. Significance level: $p < 0.05$.

During recordings of DAPs which were elicited from different holding membrane potentials we observed a voltage dependency of the DAPs. DAPs triggered at more negative membrane potentials showed an increase in DAP deflection and width. Based on these observations and the significant correlation between DAP width and the membrane resting potential in rats (see Tab. 3.4 and Fig. 3.3 E), we started to investigate how the DAP could be modulated. Therefore we preceded a 2 ms AP triggering ramp with a 500 ms hyperpolarizing or depolarizing current step, as illustrated for one example cell in the upper panel A1 of Figure 3.4. The corresponding cell membrane responses are shown in A2. The DAP deflection (diamonds) / DAP width (triangles) of each given trace are displayed as a function of the membrane potential. The vertical dotted blue line represents the resting potential of this example cell. Both the DAP deflection and width (Figure 3.4 B, D and E) correlate significantly with the "pre-AP" membrane potential in 14 out of 16 measured cells. These results are illustrated in Table 3.5, which summarizes the correlation coefficients for each individual cell of DAP deflection, DAP width and voltage threshold modulated by triggering the DAP from different "pre-AP" membrane potential. Hyperpolarizing the cells increased the amplitude of the DAP deflection and the width of the DAP, while depolarizing led to a decrease. These findings suggest that pre-polarization does indeed influence the DAP and that the DAP is voltage-dependent. Figure C shows the amplitude of the DAP deflection as a function of the voltage threshold. The voltage threshold does not change over the course of repetitions and does not correlate with the amplitude of the DAP deflection (15 cells out of 16, for one cell a significant correlation was found, see Tab. 3.5). Thus, the amplitude of the DAP deflection does not appear to be influenced by the voltage threshold. All DAP deflection and width data were found to be normally distributed and therefore the Pearson correlation coefficients were calculated. In turn, not all the voltage threshold data was normally distributed and therefore the non-parametric Spearman correlation was computed.

Additionally, we tested whether the length of the pre-hyperpolarization- or pre-depolarization affected the DAP by changing this time window (30 ms, 60 ms, 125 ms, 250 ms and 500 ms, n = 14 cells). The time interval of the pre-stimulation was randomly chosen. To compare the DAP for these different pre-stimulation times, we first checked for normality using the Shapiro-Wilk normality test. This test was used given the small sample size. All measurements were normally distributed. Out of 14 recordings, 12 were tested with

the RM one-way ANOVA with the Greenhouse-Geisser correction. The remaining 2 were tested with the paired t-test, because the sample size was too small to apply ANOVA. The ANOVA test revealed that 4 recordings showed significant differences in the DAP deflection for different pre-stimuli. However, 8 recordings were not significantly different. The t-test revealed two significant differences. Whether the duration of the pre-stimulation has an impact on the DAP can not be concluded from these results.

The finding that the DAP amplitude increases along with membrane hyperpolarization indicates/suggests the activation and influence of low-voltage activated calcium channels. This and the impact of other channels will be studied in the following subsections.

Cell	Corr. Defl.	Corr. Width	Corr. VT	t =
1	-0.9014*	-0.9673*	-0.01818	10
2	-0.982*	-0.9896*	0.1399	12
3	-0.9856*	-0.996*	0.3424	7
4	-0.9488*	-0.9919*	0.6458*	11
5	-0.9623*	-0.985*	-0.07732	10
6	-0.3372	-0.5212	-0.4021	8
7	-0.8557*	-0.9618*	-0.02114	11
8	-0.8532*	-0.945*	0.3261	10
9	-0.6283*	-0.9706*	-0.04245	11
10	-0.7517*	-0.9081*	-0.4	11
11	-0.9792*	-0.988*	0.7368*	11
12	-0.873*	-0.9622*	0.1367	11
13	-0.8734*	-0.9511*	0.4848	11
14	-0.9652*	-0.986*	-0.4167	9
15	-0.9734*	-0.9561*	-0.03607	12
16	-0.5637	-0.5888	-0.5879	10

Table 3.5: Correlation coefficients of modulated DAPs for DAP deflection, DAP width and the voltage threshold (VT). First column indicates the cell number with a total number of tested cells n = 16. Second to fourth column shows computed correlation coefficients for DAP deflection, DAP width and VT. Correlation coefficients of DAP deflection/width were computed between DAP deflection/width and "pre-AP" membrane potential. The correlation coefficients for VT were measured between DAP deflection and VT. Stars indicate significance at a significance level: $p < 0.05$. Last column shows the number of measured trials (t) at different "pre-AP" membrane potentials for each individual cell.

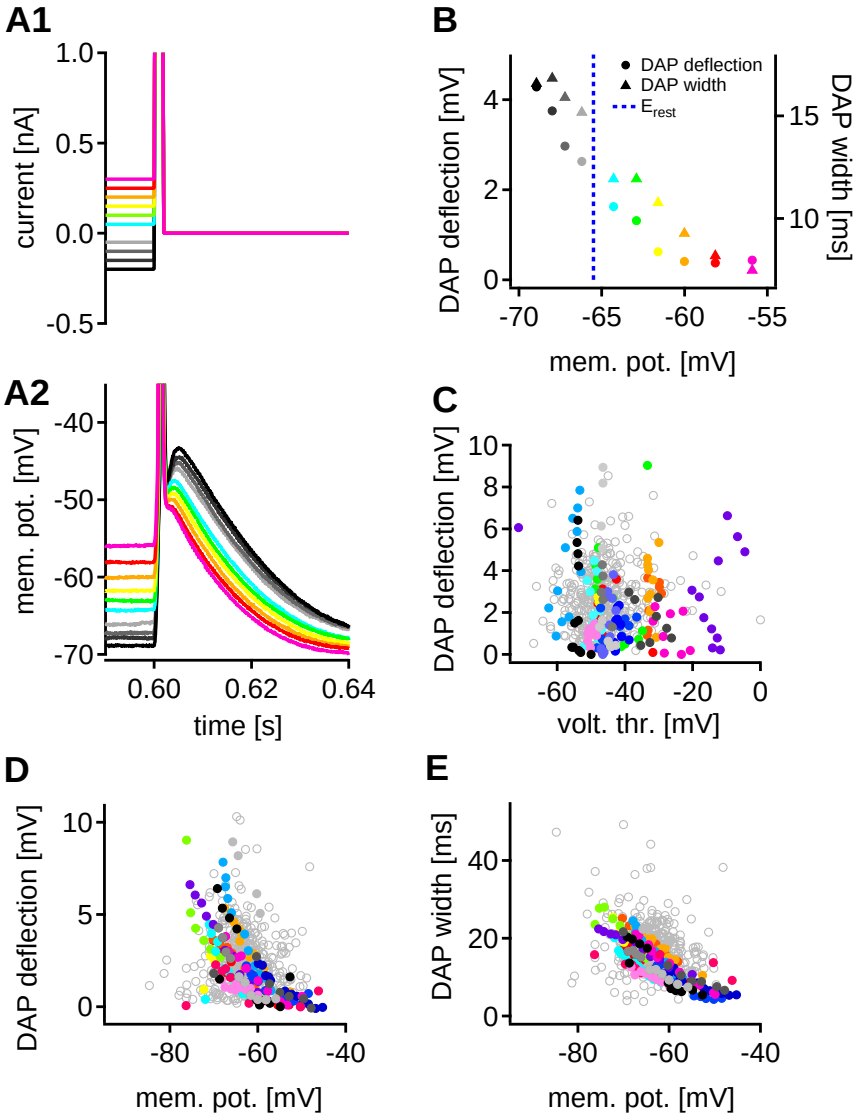

Figure 3.4: Depolarizing afterpotentials: Voltage dependence. (A1) Cutout of a 500 ms depolarizing- and hyperpolarizing current injection stepper followed by a 2 ms ramp. (A2) Corresponding membrane potential deflection in response to the different current injections. Grey scales represent hyperpolarizing and colored scales depolarizing currents/responses. (B) DAP deflection (diamonds) and DAP width (triangles) plotted as a function of the membrane potential (from A2). The dotted line represents the cell's resting potential. Summary plots of DAP deflection (C-D)/ width (E) as a function of the voltage threshold and of different membrane potential levels. All measured cells (n = 16) are represented by different colors. Unfilled grey dots indicate repeated basic ramp data from Figure 3.3.

The possible influence of voltage-gated calcium channels on the properties of the DAP was tested in a series of pharmacological experiments using three different types of voltage-gated calcium channel blockers. Additionally, we also tested the impact of TTX, a voltage-gated sodium channel blocker, and ZD, a blocker of the hyperpolarization-activated cation currents (I_h), on the DAP complex. In a final control experiment, we recorded responses from cells directly at the beginning of the recordings and 15-30 minutes later, simulating the long recording time with drug application.

We first compared the DAPs under control conditions to that 3-4 minutes after bath application of a blocker. All measured data were tested for normality with the Kolmogorov-Smirnov test. Depending on whether the data was normally distributed or not, either a parametric or a non-parametric test was used to assess statistical significance: (i) Paired tests for paired samples (control vs. drug), (ii) Wilcoxon matched-pairs signed rank test and (iii) one-way repeated measures ANOVA for multiple comparisons (control vs. drug at different concentrations).

3.4.1 *NNC*

NNC (55-0396 dihydrochloride) is a highly selective blocker of Ca_v3 low-voltage activated T-type calcium channels (Huang et al., 2004). In our experiments we used 20 µM, the same concentration as used by Alessi et al. (2016). Figure 3.5 A illustrates the responses of an example cell during the control condition (black) and after bath-application of NNC (blue). The amplitude of the DAP seems to decrease notably without a change in the "pre-AP" membrane potential. Cells were stimulated at their resting potential. All measured data were normally distributed. The paired t-tests (two-tailed) revealed no significant change in the resting potential (Fig. 3.5 B), but significant differences in AP width, DAP deflection and DAP width (n = 11). The AP broadened in most cells (C). The amplitude of the DAP deflection decreased considerably (D), resulting in a shortening of the DAP width (E) (Tab. 3.6). These results corroborate the findings of Alessi et al. (2016) and suggest a contribution of low-voltage activate Ca_v3 channels in the generation of DAPs in MEC layer II neurons.

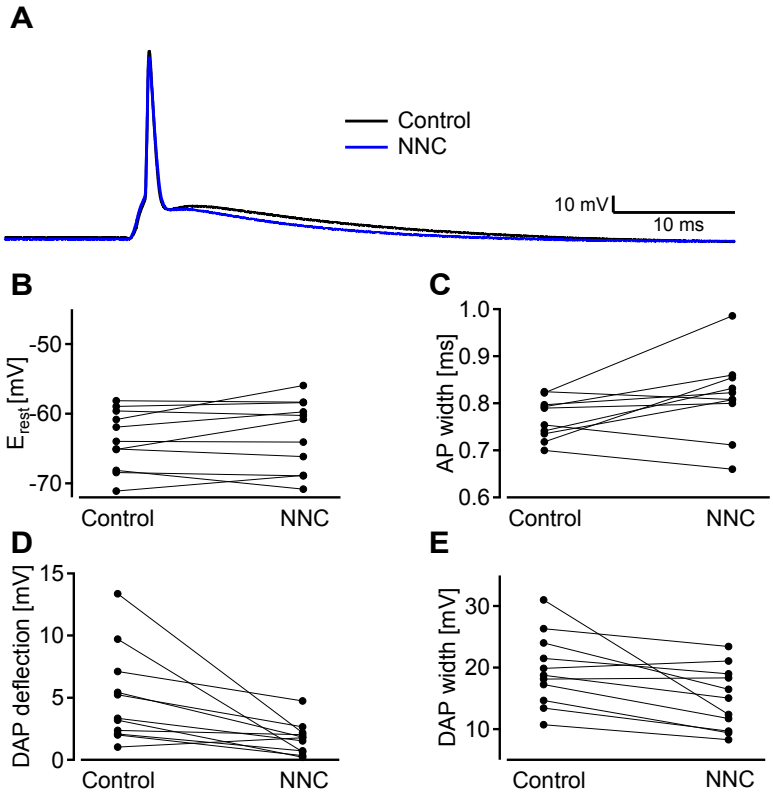

Figure 3.5: Effects of the T-type channel blocker NNC on DAPs in MEC II layer neurons. (A) Single APs elicited by a short current ramp under control conditions (black) and after bath application of 20 µM NNC (blue). (B-E) Scatter plots of different characteristics identified under control and in the presence of NNC on the left axis: (B) resting membrane potential (E_{rest}), (C) AP width, (D) amplitude of the DAP deflection and (E) DAP width.

3.4.2 *Cadmium chloride*

We also evaluated the effect of Cadmium chloride (Cd^{2+}) on the DAP properties. Cd^{2+} is a non-selective blocker of voltage-dependent calcium channels and its influence on fast DAPs has already been tested in pyramidal cells of the prefrontal cortex (Haj-Dahmane and Andrade, 1997). Cd^{2+} has also been shown to affect the afterhyperpolarization of MEC layer II cells (Khawaja et al., 2007). In our experiments we applied 100 µM Cd^{2+}. This concentration led to no notable change in the resting membrane potential (Fig. 3.6 A and B), while the amplitude of the DAP deflection (D) and the DAP width (E) decreased significantly or completely vanished. The AP width (C) in the Cd^{2+}

Char.	Control		NNC		p value
E_{rest}, mV	-63.74	± 4.274	-62.92	± 5.06	0.2740
AP width, mV	0.762	± 0.045	0.809	± 0.08	0.0484
DAP defl., mV	4.994	± 3.785	1.702	± 1.29	0.0129
DAP width, ms	19.62	± 5.905	14.99	± 5.10	0.0154

Table 3.6: Mean values and statistical tests of control and NNC effects on the DAP. Data of drug application via bath (n = 11). Calculated p values of the paired t-test (two-tailed) are added. Significance level: $p < 0.05$.

condition was also significantly different compared to the control condition (Tab. 3.7). Another difference between control and blocking condition is a positive shift of the voltage threshold which should not be confused with two spikes (blue trace in Fig. 3.6 A). Given that the DAP deflection and the DAP width were not normally distributed, the Wilcoxon matched-pairs signed rank test was used to test for statistical significance. The other two characteristics were normally distributed, therefore the paired t-test was applied.
From these results it can be concluded that voltage-dependent calcium channels have an impact on the AP and the DAP.

Char.	Control		Cd^{2+}		p value
E_{rest}, mV	-63.41	± 4.552	-63.2	± 5.009	0.5764
AP width, mV	0.757	± 0.127	0.821	± 0.150	0.0451
DAP defl., mV	2.264	± 1.373	0.520	± 0.939	0.0039
DAP width, ms	14.61	± 4.888	5.415	± 8.628	0.0039

Table 3.7: Mean values and statistical tests of control and Cd^{2+} effects on the DAP. Data of drug application in the bath (n = 9). Calculated p values of paired t-test (two-tailed)/Wilcoxon matched-pairs signed rank test are added. Significance level: $p < 0.05$.

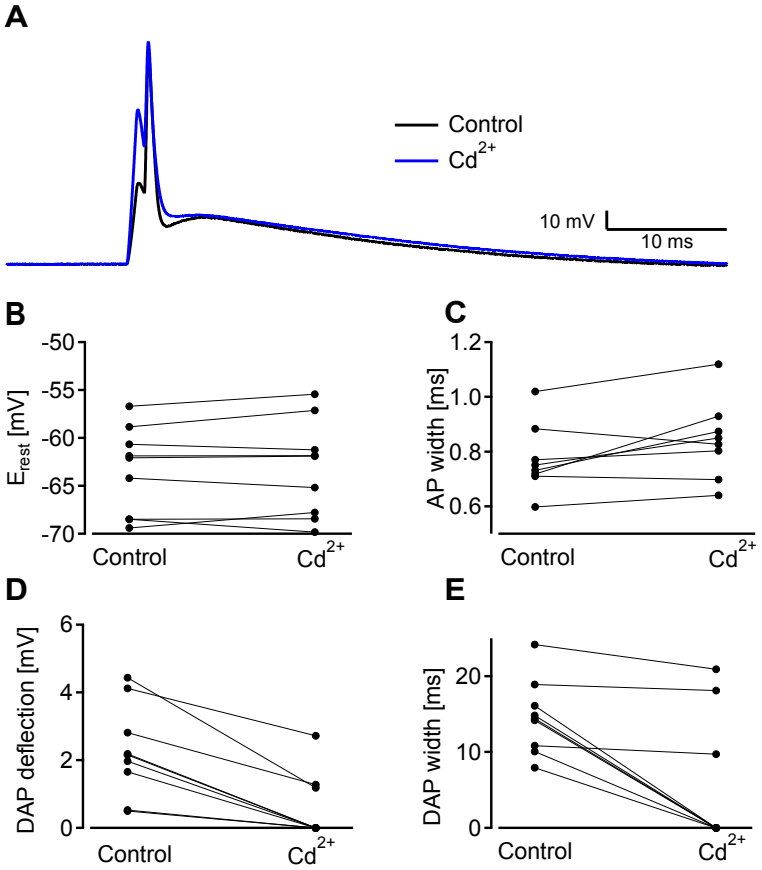

Figure 3.6: Effects of non-selective calcium channel blocker Cd^{2+} on DAPs in MEC layer II neurons. (A) Single APs elicited by a short current ramp under control conditions (black) and after bath application of 100 µM Cd^{2+} (blue). (B-E) Scatter plots of different characteristics identified under control conditions and in the presence of Cd^{2+} on the left axis: (B) resting membrane potential (E_{rest}), (C) AP width, (D) DAP deflection and (E) DAP width.

3.4.3 *Nifedipine*

In addition, we evaluated the effects of 50 µM Nifedipine on the DAP complex. Nifedipine is a selective blocker of high-voltage-activated L-type calcium channels (Huang et al., 2004). We found that 50 µM Nifedipine had a significant effect on the resting potential (Fig. 3.7 B), depolarizing it by an average of 2 mV. Nifedipine also significantly widened the AP (C) and had a significant inhibitory effect on the amplitude of the DAP deflection (A and D). In contrast, the DAP width (E) was not significantly (Tab. 3.8) decreased, although the measured width was less because of the smaller DAP deflection (A). In summary, the blocking of high-voltage-activated L-type calcium channels affects both AP and DAP phenomena; in particular, calcium currents seem to be a prerequisite for pronounced DAPs.

Char.	Control		Nif		p value
$\mathbf{E_{rest}}$, mV	-64.43	± 1.51	-62.19	± 1.84	0.0386
AP width, mV	0.701	± 0.09	0.78	± 0.11	0.0335
DAP defl., mV	6.144	± 3.01	2.606	± 2.75	0.0260
DAP width, ms	24.98	± 11.8	15.82	± 6.71	0.1084

Table 3.8: Mean values and statistical tests of control condition and Nifedipine effects on the DAP. Data of drug application via bath (n = 5). Calculated p values of paired t-test (two-tailed) are shown, too. Significance level: $p < 0.05$.

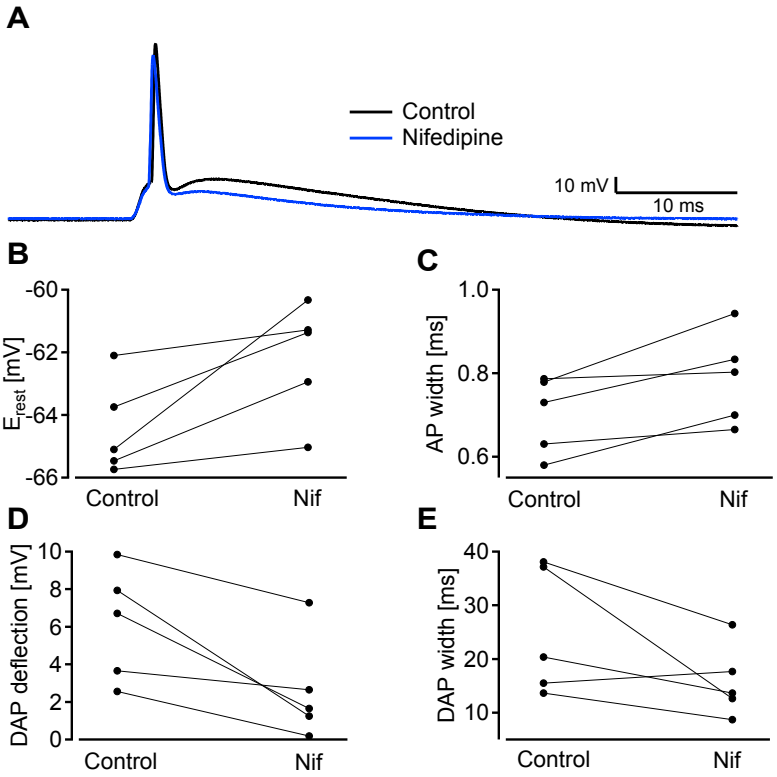

Figure 3.7: Effects of the L-type calcium channel blocker Nifedipine on DAPs in MEC layer II neurons. (A) Single APs elicited by a short current ramp under control conditions (black) and after applying 50 µM Nifedipine (blue). (B-E) Scatter plots of different characteristics in the control condition and in the presence of Nifedipine on the left axis: (B) resting membrane potential (E_{rest}), (C) AP width, (D) DAP deflection and (E) DAP width.

3.4.4 *TTX*

After testing three different blockers of voltage-gated calcium channels, we were interested in the effects of voltage-gated sodium channels (VGSC) on the generation of DAPs. VGSC are important for the formation of the AP (rising phase) (Hodgkin and Huxley, 1952). Therefore, we analyzed the DAP sensitivity to different concentrations of TTX using the ramp and ZAP stimulus. Concentrations as low as 0.03/0.04 and 0.08 were used to avoid strong effects on the AP. A saturating concentration of 2 µM TTX was applied at the end of each experiment to see whether the DAP complex is still elicited even without a preceding AP. Because this experiment was performed on a relatively small number of cells, it was only possible to statistically compare the control and the 2 µM condition (n = 5). The resting potential and the resonance frequency were normally distributed (Kolmogorov-Smirnov test), but the two-tailed t-tests did not reveal any significant differences between control and the 2 µM condition (see Tab. 3.9). APs and the ensuing DAPs could not be elicited with a saturating concentration of 2 µM TTX, as illustrated by the blue trace in the example in Figure 3.8 A. However, at low concentrations of TTX, DAPs and the preceding APs could be triggered, albeit with a decreased DAP deflection and DAP width, as shown in Figure 3.8 A, D and E. In turn, the AP width increased as the concentration of TTX was increased (Fig. 3.8 C). The legend describes the different measures for the five recorded cells. These results are consistent with data from Alessi et al. (2016), who could show that 0.03 µM TTX have significant effects on the AP shape and also considerably influences the DAP.

Char.	Control	n = 5	TTX 0.03	n = 2
E_{rest}, mV	-61.01	±4.33	-59.6	±1.34
AP width, mV	0.68	±0.04	0.79	±0.12
DAP defl., mV	1.55	±1.06	0.468	±0.17
DAP width, ms	11.4	±5.02	9.52	±2.71
$f_{resonance}$, Hz	6.7	±1.3	6.55	±1.5
Char.	TTX 0.04	n = 3	TTX 0.08	n = 2
E_{rest}, mV	-65.56	±4.02	-66.55	± 6.879
AP width, mV	0.82	±0.045	1.055	±0.360
DAP defl., mV	1.021	±1.101	0.375	±0.5303
DAP width, ms	9.147	±8.325	7.015	±9.921
$f_{resonance}$, Hz	4.9	±1.77	5.8	±0.28
Char.	TTX 2	n = 5	p value	
E_{rest}, mV	-62.56	±9.67	0.6336	
AP width, mV	-	-	-	
DAP defl., mV	-	-	-	
DAP width, ms	-	-	-	
$f_{resonance}$, Hz	6.23	0.92	0.1467	

Table 3.9: Mean values ± SD and statistical tests relating to the effect of different concentrations of TTX (0.03, 0.04, 0.08 and 2 μM) on DAP properties. Data of n = 5 measured cells. TTX was bath applied. The p values were calculated from paired t-tests (two-tailed, $p < 0.05$), which was only possible for the control and 2 μM TTX conditions, because of the small number of cells in other concentration conditions. Significance level: $p < 0.05$.

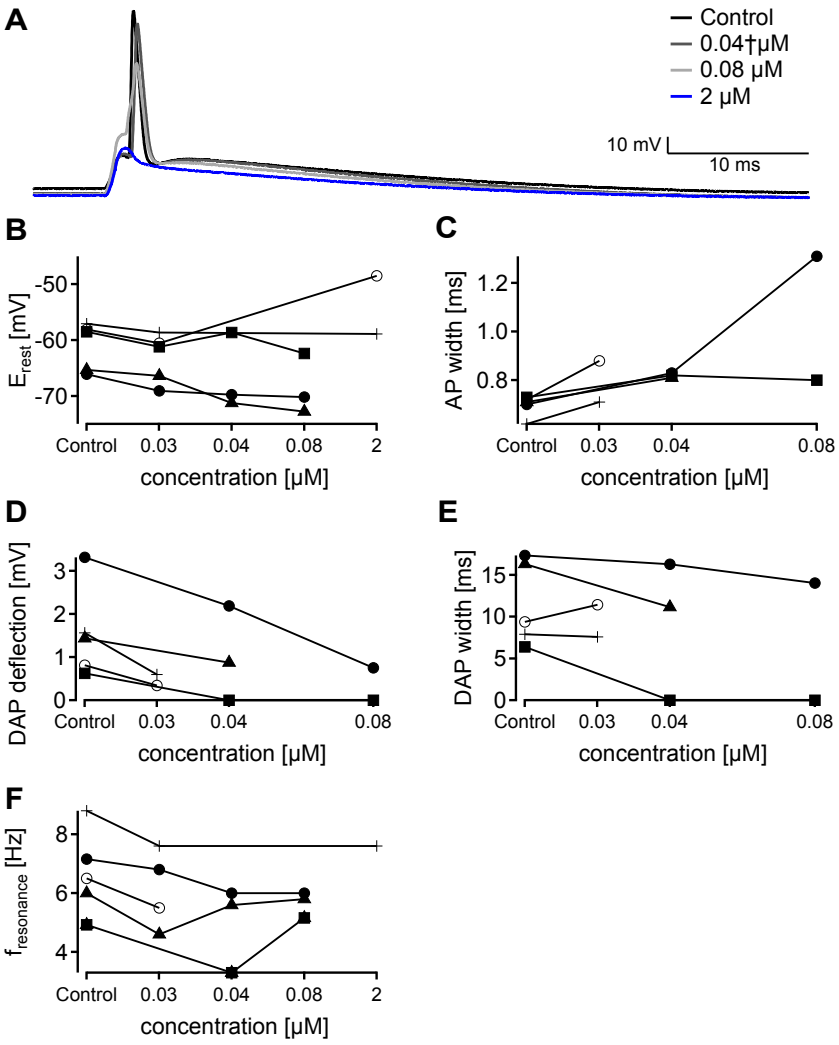

Figure 3.8: Effects of different concentrations of TTX (0.03, 0.04, 0.08 and 2 µM) on DAPs in mEC layer II neurons. (A) Single APs elicited by a short current ramp under control conditions (black) and after bath application of 0.04 µM (dark grey), 0.08 µM (light grey) and 2 µM (blue) of TTX. (B-F) Scatter plots of different characteristics in the control condition and in the presence of different concentrations of TTX for n = 5 cells: (B) resting membrane potential (E_{rest}), (C) AP width, (D) DAP deflection, (E) DAP width and (F) resonance frequency ($f_{resonance}$).

3.4.5 *ZD*

Additionally, we assessed the effects of 50 µM ZD (ZD7288), a blocker of HCN channels which mediate I_h (BoSmith et al., 1993), on the DAP. I_h is a slow, non-inactivating inward current activated by hyperpolarization, which deactivates slowly upon depolarization (Dickson, Magistretti, M. H. Shalinsky et al., 2000). Blocking HCN channels led to a significant difference in resting membrane potential (Fig. 3.9 B) and completely abolished the sag (D) and the resonance frequency (E). There was a significant broadening effect on the AP width (C) and the amplitude of the DAP deflection was significantly decreased (F), while the DAP width showed no changes (G) (Tab. 3.10). The effect of ZD on the resonance frequency, the sag, and the resting membrane potential are consistent with reported results in the literature (Alonso and Klink, 1993; Dickson, Magistretti, M. H. Shalinsky et al., 2000; Haas et al., 2007). In contrast, the effects on the AP width and the DAP deflection have not been previously reported, and might be due to interactions between I_h and the T-type calcium conductance.

Char.	Control		ZD		p value
$\mathbf{E_{rest}}$, mV	-65.63	± 3.262	-71.74	± 7.41	0.0283
AP width, mV	0.8072	± 0.065	1.18	± 0.65	0.0078
DAP defl., mV	4.68	± 3.028	1.648	± 1.47	0.0257
DAP width, ms	27.42	± 8.215	24.08	± 13.6	0.5308
$\mathbf{f_{resonance}}$, Hz	4.127	± 1.433	0	± 0	0.0007
Sag, mV	2.589	± 1.055	0.0781	± 0.22	0.0002

Table 3.10: Mean values ± SD and statistical tests of control and ZD (n = 8) effects on the DAP. Calculated p values of the paired t-tests (two-tailed, $p < 0.05$) and the Wilcoxon matched-pairs signed rank test (AP width and Sag) are added. Significance level: $p < 0.05$.

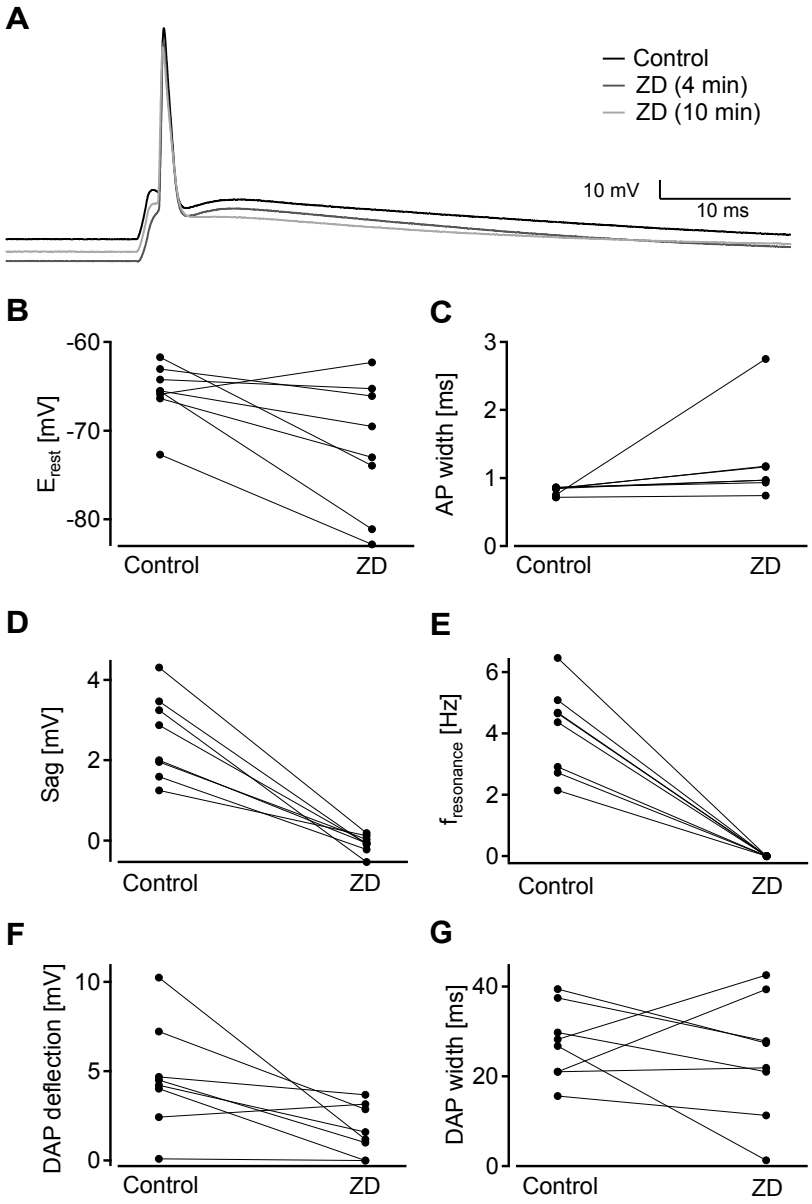

Figure 3.9: Effects of 50 μM HCN/Ih blocker ZD on DAPs in MEC layer II neurons. (A) Single APs elicited by a short current ramp under control conditions (black) and after bath application of 50 μM ZD (grey). (B-G) Scatter plots of different characteristics in the control condition and in the presence of ZD on the left axis: (B) resting potential (E_{rest}), (C) AP width, (D) sag, (E) resonance frequency ($f_{resonance}$), DAP (F) deflection and (G) width.

3.4.6 *Washout*

Finally, we tested the effect of patching cells over the same time interval (approximately 25 minutes): the control condition (10 min), bath application (4 min) and drug condition (10 min). As before, we injected the same short current ramp 1 minute after patching the cell (Control) and again after 30 minutes but without any drug application (washout) (Fig. 3.10A). Patching cells (n = 5) over a long time period had no significant effects on the resting membrane potential (B) (paired t-test) and on the AP width (C) (Wilcoxon matched-pairs signed rank test) as shown in Tab. 3.11. The DAP complex, however, did change significantly over this time period. Surprisingly, both the amplitude (D) and the width (E) of the DAP deflection decreased significantly (Tab. 3.11), as tested with the paired t-test ($p < 0.05$).
These results were unexpected. They call into question the conclusions from the previous subsections and make an interpretation of all pharmacologically measured data difficult.

To get back to our initial idea that DAPs underlie transient bursts/short ISIs/doublets we investigate the function of the DAP in the following section.

Char.	Control		washout		p value
$\mathbf{E_{rest}}$, mV	-67.46	$\pm$ 2.668	-66.47	$\pm$ 1.821	0.3192
AP width, mV	0.722	$\pm$ 0.031	0.732	$\pm$ 0.058	0.6968
DAP defl., mV	2.338	$\pm$ 1.062	0.75	$\pm$ 0.738	0.0176
DAP width, ms	14.28	$\pm$ 2.092	9.846	$\pm$ 1.645	0.0013

Table 3.11: Mean values $\pm$ SD and statistical tests of Control and washout effects on the DAP. Data were measured 1 and 30 minutes after patching the cells (n = 5). The resting membrane potential, DAP deflection and DAP width were tested for significant differences using the paired t-test (two-tailed). The AP width was not normally distributed and was therefore tested using Wilcoxon matched-pairs signed rank test. Calculated p values are added. Significance level: $p < 0.05$.

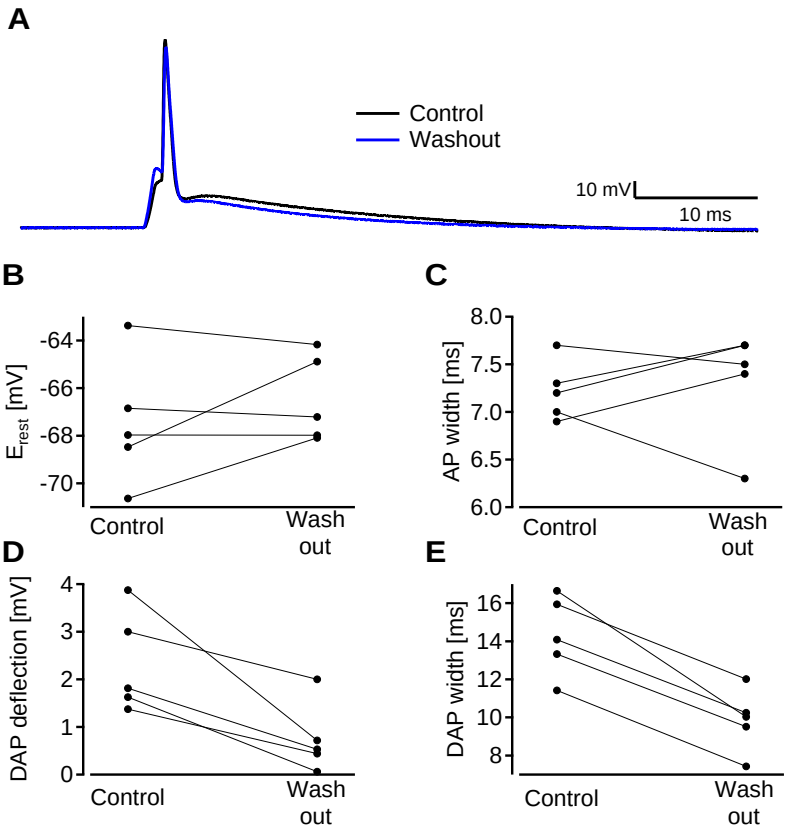

Figure 3.10: Effects of long recordings on DAPs in MEC layer II neurons. (A) Single APs elicited by a short current ramp after 1 minute (control, black) and after 30 minutes (washout, blue). (B-E) Scatter plots of different characteristics in the control condition and during the washout condition, as shown on the left axis: (B) resting membrane potential (E_{rest}), (C) AP width, (D) DAP deflection and (E) DAP width.

My initial hypothesis was that DAPs facilitate doublets or bursts of action potentials I tested this hypothesis in mEC layer II cells (n = 19) using a paired pulse stimulation protocol. First, the current required to elicit an action potential was determined with a ramp stimulus (see Methods). A current 20% above this measured current threshold was used for the following experiment. The protocol procedure is explained in Figure 3.11 A and its subfigures:

First, a standard 2 ms ramp was injected as a control measurement (control ramp). After an interval of 200 ms, cells were hyperpolarized (blue) or depolarized (red) by $\pm$100 pA for 500 ms or not stimulated at all (control condition in black) (see Fig. 3.11 A3). After this stimulation, cells were allowed to return to their resting membrane potential for 5-7 ms before a double ramp was injected. The double ramp consists of two ramps, as can be seen in Figure 3.11 A1 and its corresponding current trace in Figure A2. A standard ramp (2 ms), equal to the control ramp, was followed by a second smaller ramp (2 ms). This stimulation protocol was repeated twelve times with the same current intensity, but each time the second ramp was shifted by 2 ms to a later time point (see Fig. 3.11 A2). For the first intensity condition, a current below, but close to threshold, was chosen for the second ramp. After this current intensity condition, the intensity of the second ramp was increased by 100 pA and so forth. These alterations shifted the second response from sub- to suprathreshold. To investigate the DAP dependence on the pre-stimulation membrane potential, DAP values were calculated from the mean of the last three repetitions of one intensity condition, and this was repeated for all intensities.

Figure 3.12 A shows a raster plot of the suprathreshold responses to the second ramp of one example cell, stimulated with different current intensities as a function of the inter-spike interval between APs triggered by the first and second ramp. Current required to elicit an AP on the second ramp of the double ramp complex was computed as percentage needed for an AP on the first ramp of the double ramp (% 1st. AP current). Another measurement was determined from this experiment: the firing window. This illustrates the time interval between the first and last elicited AP (in the second ramp) in all conditions, again separated for control, hyperpolarization and depolarization. As can be seen in A and B, hyperpolarizing the cells reduced the current required to elicit an AP in response to the second ramp and hyperpolarized cells fired for much longer. Figures B and C show that the amplitude of

the DAP deflection correlates with these two measurements, the firing window and the percentage of current required relative to the first AP of the double ramp. Cells with larger DAP deflections are able to elicit a second AP for longer and have a broader firing window (B). This was also shown to be statistically significant according to the Friedman test (not all measurements were normally Gaussian-distributed with the Kolmogorov-Smirnov test). Furthermore, cells with larger DAPs require significantly (tested with one-way ANOVA, data showed normal distribution) less current to trigger another AP (C).

In conclusion, the results of the DAP function show that the window of opportunity for a second, quickly following spike gets broader by increased amplitudes of the DAP deflection. Additionally, the results suggest that DAPs facilitate spiking by greatly decreasing the current threshold. These data strongly support our idea that DAPs of mEC layer II cells facilitate a second spike and amplify the production of doublets or burst.

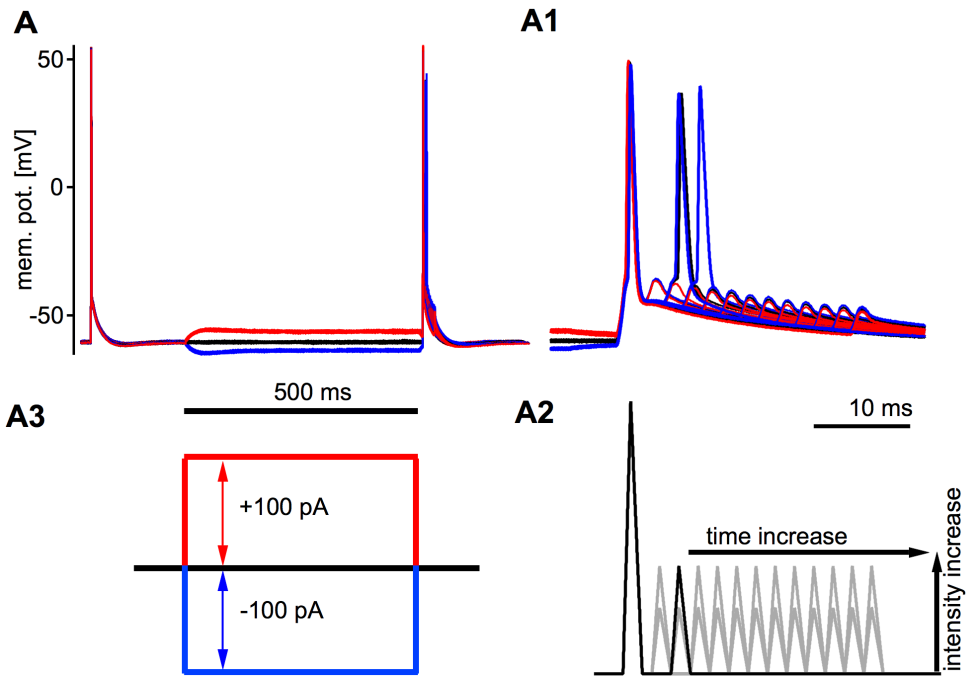

Figure 3.11: Functional implications of the DAP. (A) Cell membrane response to the paired pulse stimulus protocol with a control ramp at the beginning and the paired ramps at the end. (A1) Illustration of the cell's response to two consecutive ramps. (A2) Corresponding stimulus timing and intensity of the two consecutive ramps shown in A1. Black trace shows one stimulus trace, grey traces illustrate two whole stimulus protocols with two different current intensities. (A3) Pre-stimulation protocol of the two consecutive ramps with three different conditions: hyperpolarized (blue trace) by -100 pA, depolarized (red trace) by +100 pA and the control condition (black) without stimulation.

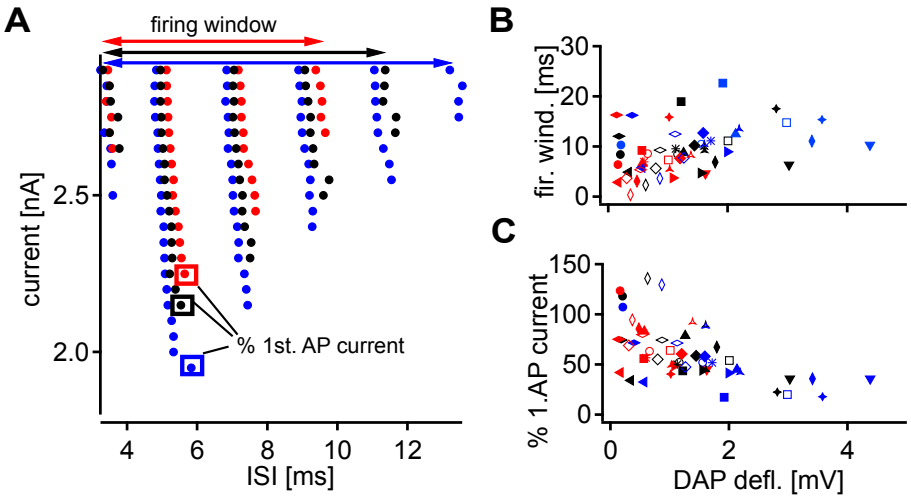

Figure 3.12: (A) Current required to elicit an AP at the second ramp of the two consecutive ramps as a function of the time between this AP and the AP of the first double ramp (inter-spike-interval (ISI)) in all three conditions. The first AP for all three stimulus conditions is indicated with a box and the firing window of each condition is shown with an arrow. (B) Time interval of the firing window (Correlation coefficient value $\pm$ SD = 0.017 $\pm$ 0.017) and the current threshold of the first AP (C) (Correlation coefficient value $\pm$ SD = 0.017 $\pm$ 0.05) correlate with DAP deflection. Different symbols in B and C illustrate different cells with the three conditions (blue, red and black).

3.6.1 *Post-hoc stainings of electrophysiologically recorded cells*

According to Alonso and Klink (1993), layer II of the entorhinal cortex contains two types of principal neurons classified as stellate cells (SCs) and pyramidal cells (PCs). Distinctive features of SCs are a prominent sag responses to hyperpolarization, intrinsic subthreshold membrane potential oscillations in the theta frequency range (near the resonance frequency) and a short latency at rheobase. In both the rat and gerbil, mEC principal neurons show similar responses. The serotype of mEC neurons that show these responses is under debate, and to allow for better discrimination between these two cell types of layer II, we combined electrophysiological recordings with immunohistochemistry by labeling recorded neurons posthoc (see Methods 2.5) (Varga et al., 2010; Ray, Burgalossi et al., 2017; Kitamura et al., 2014). Varga et al. (2010) identified two cellular markers, Reelin and Calbindin, which appear to label stellate and pyramidal cells, respectively. We therefore used these two markers and related the morphology of recorded cells to the analysis of their intrinsic electrophysiological properties. An example of a sagittal mEC section with recorded cells (pink) and the post-hoc Calbindin (green)- and Reelin (blue)-immunoreactivity is shown in Figure 3.13 A.

A comparison between labeled cells and their corresponding properties is illustrated in Figure 3.13 B1-B3. Magnified patched cells are filled with Alexa 594 and then post-hoc stained with Calbindin and Reelin (B1). The first example cell is Reelin-positive and Calbindin-negative. It responds with a pronounced sag (B2) and displays resonance (B3). Both results, immunostainings and recorded features, refer to the described SC.
The second cell is also Reelin-positive and Calbindin-negative, which would again indicate a SC. But the cell displays only a very small sag and a very low resonance frequency suggesting a PC. Here, both results conflict with each other.
A pronounced sag and resonance frequency, indicating the presence of a SC is elicited in example cell three, which shows both a positive Reelin and a positive Calbindin staining. The double staining is surprising and indicates an overlap of these two cytochemical populations.
However, the fourth example is again both Reelin-positive and Calbindin-positive, but exhibits no sag and no resonance response. Without the Reelin-positive staining this cell would refer to the typical pyramidal neuron. The double-labeling suggests more heterogeneous cell populations than expected.

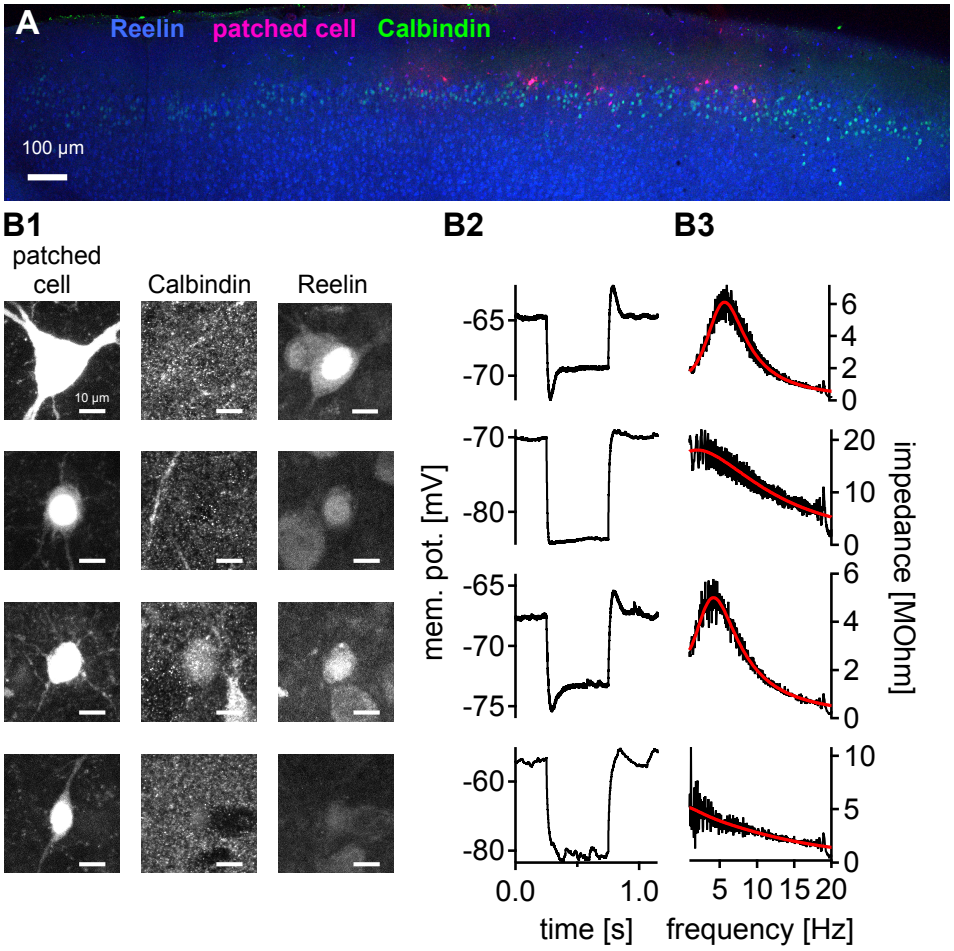

Figure 3.13: Cell type-specific expression of Calbindin and Reelin in mEC neurons. (A) Overview of a sagittal mEC section of recorded cells (pink) and the post-hoc stained Calbindin (green) and Reelin (blue) immunoreactivity. (B1) Magnification of recorded cells filled with Alexa 594, post-hoc stained with Calbindin and Reelin and their corresponding sag (B2) and resonance properties (B3). Scale bars: overview: 100 µm; zoom: 10 µm.

Figure 3.14 summarizes the distribution of immuno-stained cells and their sag and resonance properties to see if the cell stainings match with the expected features. For this results from single stainings and from double-stainings were taken into account. In gerbils, 32 out of 38 recorded cells were Calbindin-negative and 6 positive as shown in Figure 3.14 A. Five of the positive cells displayed a prominent resonance frequency and sag and 24 of the negative cells responded with a big resonance frequency and 28 cells

with a pronounced sag.
Of a total number of 197 cells recorded in rats, 155 were Calbindin-negative and 42 positive (see Fig. 3.14 B). Of the 42 positive cells, 36 displayed a resonance frequency higher than 2 Hz and 38 had a pronounced sag (with a amplitude larger than 1 mV). Based on the Calbindin-positive stainings we would have expected no sag and no resonance frequencies (Alonso and Klink, 1993; Canto and Witter, 2012; Kitamura et al., 2014; Varga et al., 2010). Of the 155 Calbindin negative cells, 119 displayed a resonance frequency and 123 showed a prominent sag, indicating that these cells were probably SCs.
Of the 88 cells that were stained against Reelin, 86 were Reelin-positive and 2 negative. A majority (n=74) of these cells showed a prominent resonance response and 76 displayed a sag response as expected. Of the 2 negative tested cells, 2 had a resonance above 2 Hz and 1 showed a prominent sag response, again indicating heterogeneous populations.

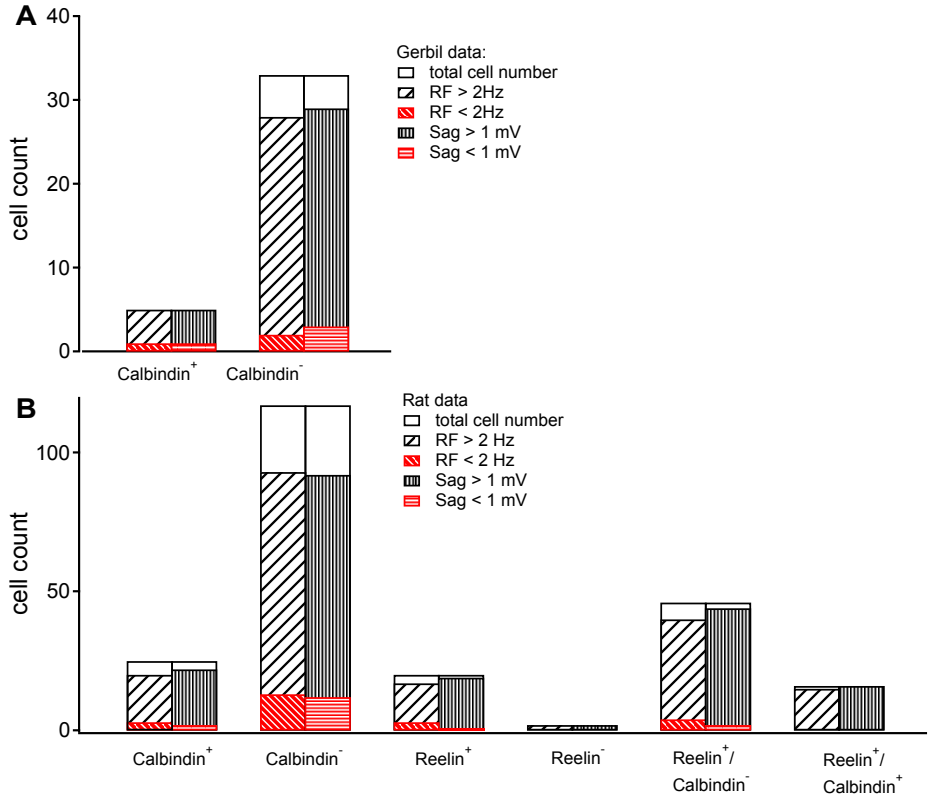

Figure 3.14: Histogram of the immuno-stained cells depending on their resonance frequency (RF) or their sag amplitude. (A) shows gerbil data and (B) rat data.

An additional and very helpful analysis is the reconstruction of the measured cells and the counting of their primary dendrites. This was done for former experiments (~first 100 measured cells) as shown in Figure 3.15 but not combined with the post-hoc stained cells. After Canto and Witter (2012) SCs and PCs can be easily distinguished by their morphology: PCs have less dendrites than SCs (2-11), a pyramidal shaped soma and an apical dendrite reaching the pia. In the former analysis most cells had 8-9 primary dendrites counted in both animal species.

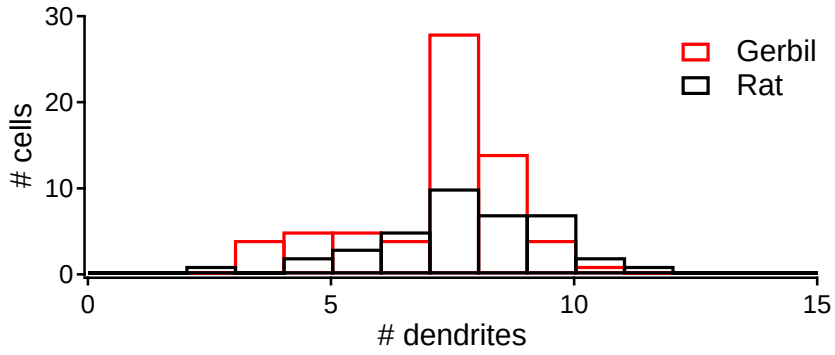

Figure 3.15: Histogram of primary dendrites in mEC layer II. Dendrites counted in rats are shown in black, dendrites counted in gerbils are shown in red.

The overlap of measured electrophysiological parameters with the cell type-specific expression stainings is not surprising, given the presence of some double labeled cells. The total number of recorded and double labeled cells is illustrated in Figure 3.14 B in the last bar graph ($Reelin^+/Calbindin^+$). All measured and labeled cells showed prominent sag and resonance responses. In Figure 3.16 an example section of layer II performed by a standard immunohistochemical procedure (see Methods 2.5) without electrophysiological recordings revealed also double labeled ($Reelin^+/Calbindin^+$) neurons indicating that this layer consists of more heterogeneous populations.

In conclusion, the comparisons of the recordings and the corresponding post-hoc-stainings of the cells show that Calbindin and Reelin are not as specific as stated by Varga et al. (2010) or that the separation by Alonso and Klink (1993) or Canto and Witter (2012) is not that homogeneous as suggested. We also found many double labeled cells. These results would explain our difficulties in classifying the different cells (see Section 3.1).

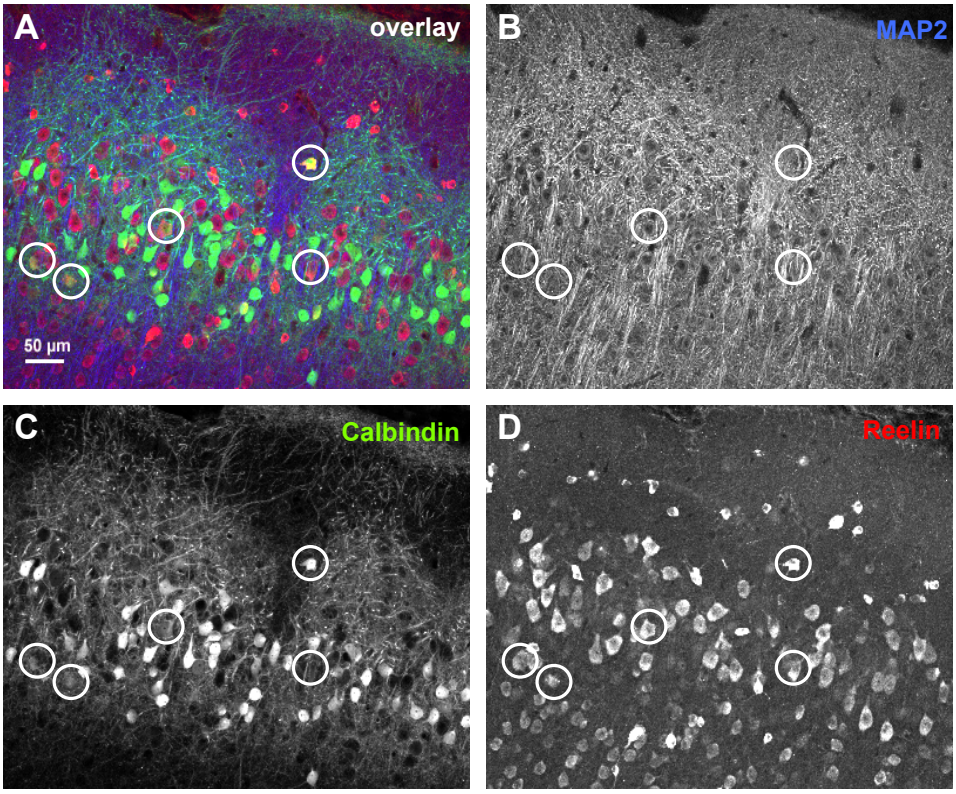

Figure 3.16: Double labeled mEC layer II neurons. (A) Representative confocal image showing the overlap of a sagittal mEC section stained against Calbindin (green), Reelin (red) and MAP2 (blue) immunoreactivity. These are also shown as single channels: (B) MAP2, (C) Calbindin and (D) Reelin. White circles indicate yellow double labeled cells. Scale bar: 50 µm.

3.6.2 *Expression profiles of Calbindin, Reelin and recorded cells*

In addition we analyzed the expression profile of Calbindin and Reelin throughout the mEC to get an impression of the distribution of PCs and SCs as well as the verification of the location of recorded cells by setting line scans (width = 50 pixel) with ImageJ (plot profile tool), as illustrated in Figure 3.17 A. The subfigures B-E represent the single line scans for the four recorded and post-hoc stained example cells in A. The blue line scans represent cells stained for Reelin, green line scans represent cells stained for Calbindin and the red line scans represent the single cells, which were recorded. Line scans always started at the pial surface to ensure a distinct starting point (= 0). Measured line scans were normalized to 1 by taking the minimum of the x values (= pial surface) and subtracting it from each

x value (= Diffx). Each Diffx was then divided by the resulting maximum value (=Max) (Diffx/Max = Factor). The arbitrary unit values of the three different channels were each divided by their maxima. Subfigure F summarizes all measured expression profiles (grey) separated for the three channels with the mean profile shown in color. These expression profiles indicate that Calbindin is restricted to a certain area (layer II and III), decreasing after 0.5, whereas Reelin expression first increases similarly to Calbindin, but then stays constant. The profiles of the patched cells indicate that the recording sites were closer to layer I than to layer III. Based on these results it is not surprising that we did not have many typical PC recordings, because we measured not deep enough. But we also wanted to be sure to record from layer II, not from layer III and the transition between both layers is hard to determine. Combining these results with the former dendrite counting reflects that most measured cells are SCs or similar to SCs (Alonso and Klink, 1993; Canto and Witter, 2012).

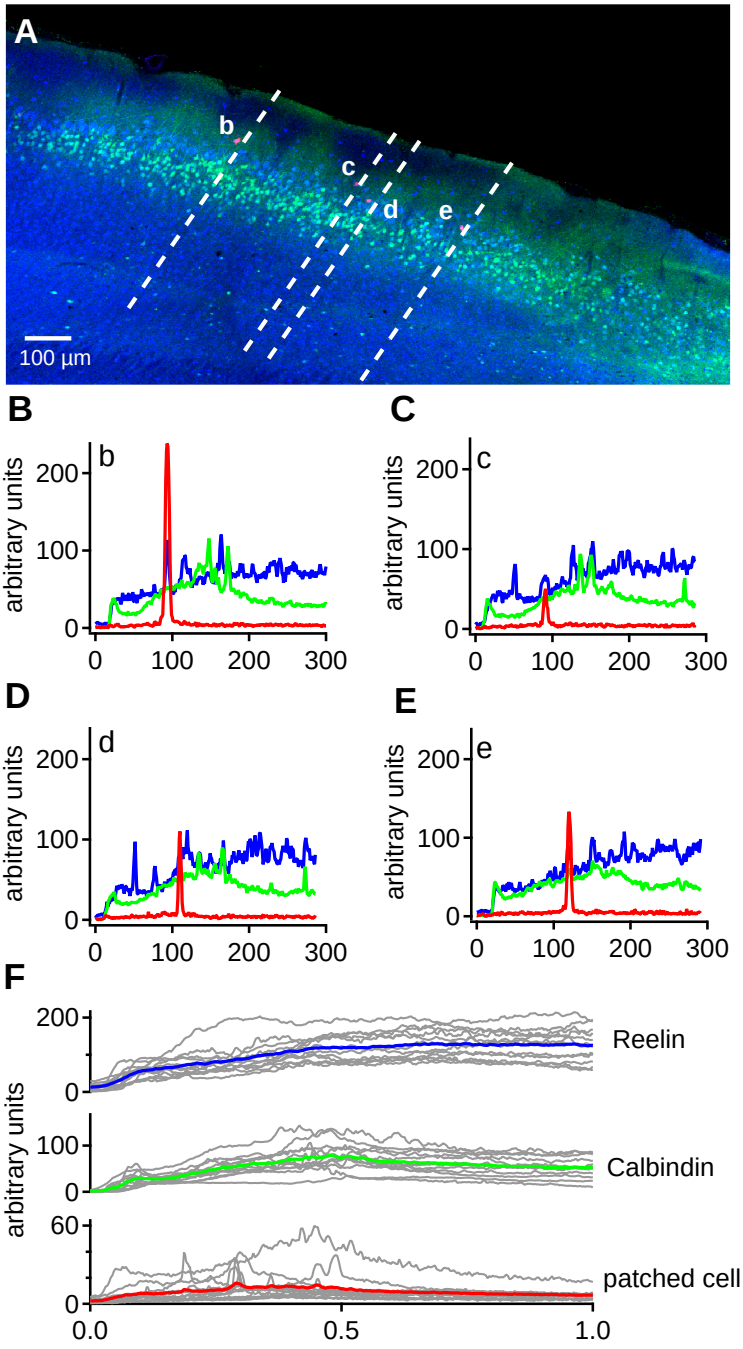

Figure 3.17: mEC line scans: (A) Overview of a sagittal mEC section of recorded cells (b-e) (pink) and the post-hoc stained Calbindin (green) and Reelin (blue) immunoreactivity, with four example line scans illustrated by dashed white lines. Scale bar: 100 µm. (B-E) Line scan profiles of arbitrary units for each color channel plotted over the line distance. (F) Mean values (in color) of normalized lines scans (grey) for n = 13 different slices from five rats.

3.6.3 *Comparisons of immunohistochemical procedures*

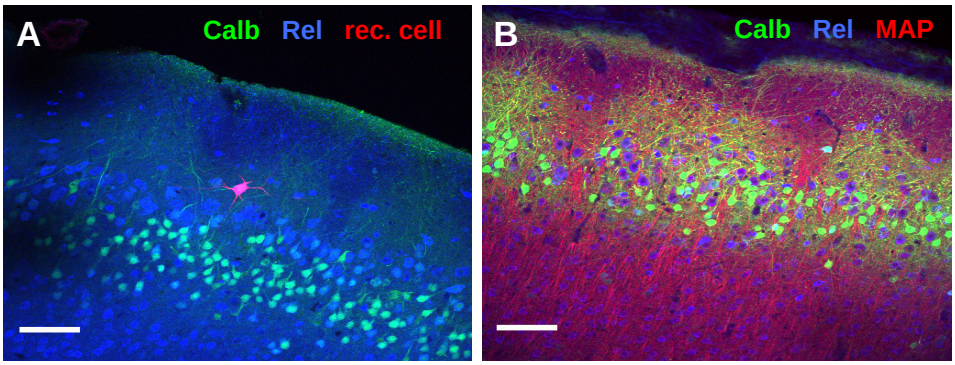

Figure 3.18: Comparison of immunohistochemical stainings between slices that had previously been recorded from (A) and slices from perfused animals (B). Sagittal sections of the mEC immunostained against (A) Calbindin (green) and Reelin (blue) and with a recorded cell filled with Alexa 594 (red), (B) Calbindin (green), Reelin (blue) and MAP2 (red). Scale bar: 100 µm.

We also performed standard immunohistochemical procedures (see Methods 2.5) on perfused rats to compare the quality of the staining with slices, which had previously been recorded from. An example of these two different stainings is shown in Figures 3.18 A and B. A shows a section of a 400 µm slice with a recorded neuron filled with Alexa 594 (red) and B shows a 60 µm section stained according to standard procedures. Both antibodies (against Calbindin (Calb) and Reelin (Rel)) worked well in both procedures. The slice in Figure 3.18 B was additionally stained against the microtubule-associated protein 2 (MAP2), a marker specifically expressed in the perikarya and dendrites of neuronal cells (manufacturer's technical information). In both images the described tent-like structure of bundled Calbindin-positive dendrites can be spotted (Burgalossi and Brecht, 2014; Kitamura et al., 2014) (as well as in Fig. 3.19 A and F).

Besides this comparison, we also carried out additional stainings using the antibody against Wfs1 (Wolframin Syndrom 1), another marker of pyramidal neurons (Kitamura et al., 2014), and two different antibodies against other calcium-binding proteins, Calretinin (Calr) and Parvalbumin (Parv), which specifically mark different types of interneurons (Buetfering et al., 2014; Armstrong et al., 2016; Wouterlood, Denderen et al., 2000). Figure 3.19

provides a validation of the performed immunohistochemical stainings. Figure 3.19 A (same as Figure 3.18 B) is repeated here to facilitate comparison between Calbindin and Wfs1. In B, neurons were stained against Wfs1, Reelin and Nissl (Nis). Nis is a dye, that stains the ribosomal RNA associated with the rough endoplasmic reticulum in neuronal perikarya and dendrites, and therefore stains all neurons. The antibody against Wfs1 stained pyramidal cells/somata and their dendrites, and overlapped perfectly with the antibody against Calbindin (Figure 3.19 C). The antibody against Calretinin seemed to work as well, staining smaller cells with no overlap with Wfs1 (Figure 3.19 D). Parvalbumin positive neurons and their dendrites are shown in Figure 3.19 E and F, and do not overlap with Reelin and Wfs1.

In summary, we could show that the post-hoc stainings without perfusing the animal are comparable with slices stained after standard immunohistochemical procedures. Both procedures lead to images of high quality. Double stainings of Calbindin and Wfs1 stained the same cells. In addition, calretinin and parvalbumin worked well to specifically stain interneurons.

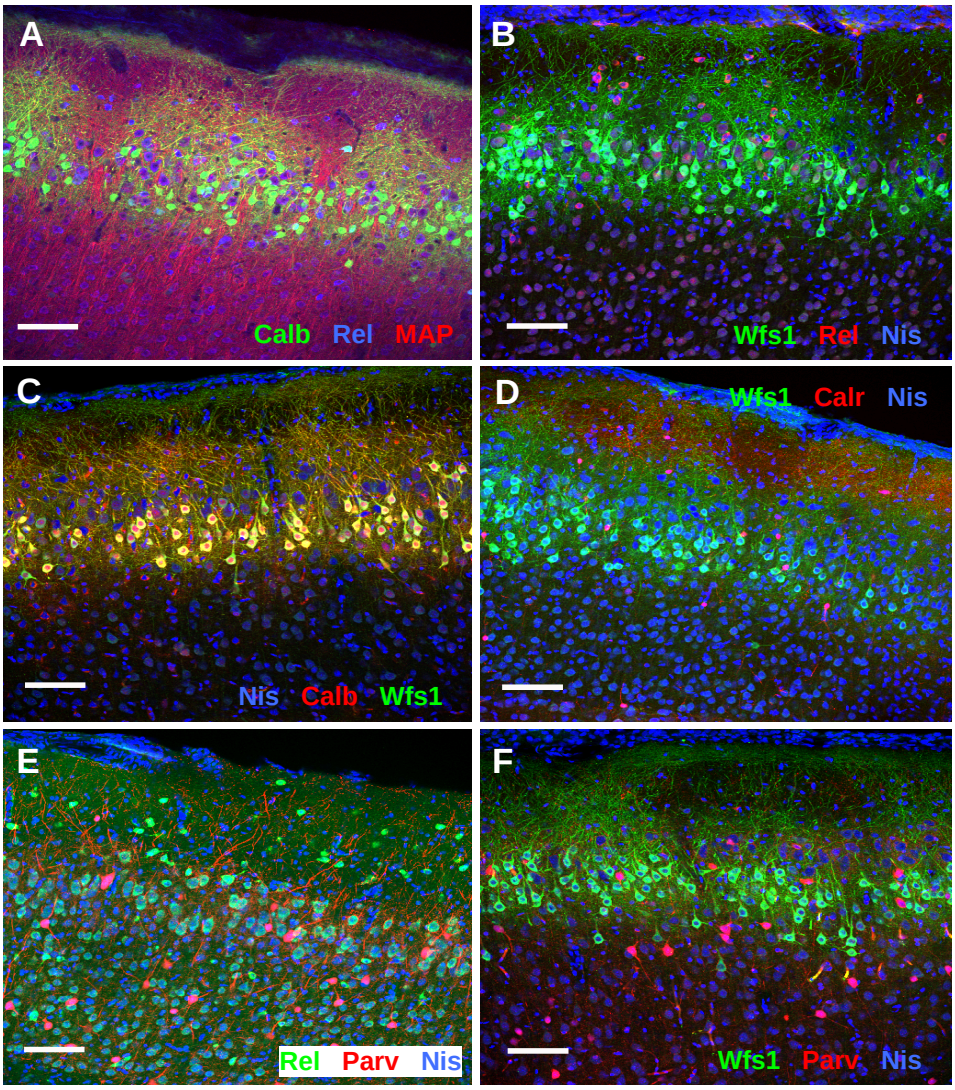

Figure 3.19: Immunohistochemical validation of Wfs1 and interneuron antibodies. Sagittal sections of the mEC immunostained against (A) Calbindin (green), Reelin (blue) and MAP2 (red), (B) Wfs1 (green), Reelin (red) and Nissl (blue), (C) Wfs1 (green), Calbindin (red, CB300) and Nissl (blue), (D) Wfs1 (green), Calretinin (red, 6B3), (E) Reelin (green), Parvalbumin (red) and Nissl (blue), (F) Wfs1 (green), Parvalbumin (red) and Nissl (blue). (A) is identical to Figure 3.18 B. Scale bar: 100 µm

I characterized the electrophysiological properties (sag, resonance and DAP) of more than 700 mEC layer II neurons and did post-hoc stainings of recorded cells. Now we will try to ascertain whether these neurons belong to distinct non-overlapping subpopulations, as Alonso and Klink (1993) and others stated (Klink and Alonso, 1997; Linden and Lopes da Silva, 1998; Canto and Witter, 2012). Therefore, we performed a heuristic approach of a quantitative cluster analysis (see Methods 2.7.2) on the rat data set (we did not use the gerbil data set because of its smaller size). A cross-validated factor analysis suggested seven identified physiological parameters to describe the measured sub- and supra-threshold responses: ISI1/ISI2, R_{in} (Mohm), resonance frequency (Hz), Q-value, AP width (ms), Latency at rheobase (ms), Tau (ms).
For these parameters, k-means clustering revealed the silhouette and similarity scores listed in Table 3.12. To validate our results from the k-means clustering, we also used an alternative method called hierarchical Ward clustering with the silhouette and similarity scores listed in Table 3.13:

k-means Cluster	C = 2	C = 3	C = 4	C = 5	C = 6
Silhouette	0.404281	0.326587	0.315212	0.253046	0.221994
Similarity	0.956311	0.953594	0.813227	0.638278	0.571260

Table 3.12: Silhouette and Similarity score of the k-means clustering for different cluster sizes. Factor and cluster analysis were performed by Johannes Nagele.

Ward-Cluster	C = 2	C = 3	C = 4	C = 5	C = 6
Silhouette	0.535201	0.397262	0.353276	0.263174	0.228609
Similarity	0.595777	0.723943	0.718715	0.544035	0.498785

Table 3.13: Silhouette and Similarity score of the Ward clustering for different cluster sizes. Cluster analysis was performed by Johannes Nagele.

The values in both Tables 3.12 and 3.13 suggested that we could divide the cell population into three or four clusters. Five or more clusters led to a considerable drop in the computed scores and were therefore excluded. To decide for C=3 or C=4 clusters I compared the selected features on which the clustering was based on. This is shown in Figure 3.20 which plots the cumulative histograms of the selected features for three (C=3) and four (C=4)

Cluster	C = 2	C = 3	C = 4	C = 5	C = 6
Similarity score	0.614	0.785	0.798	0.375	0.378

Table 3.14: Similarity scores between k-means clustering and Ward clustering for the different cluster. Cluster analysis was performed by Johannes Nagele.

clusters of the k-means clustering. A comparison the features of C=3 with C=4 indicated that cluster C2 of C=3 is identical to cluster C1 of C=4. C3 of C=3 also overlaps with C2 of C=4. Interestingly, C1 of C=3 is very similar to C3 and C4 of C=4 (see Fig. 3.20 A and B, C and D, E and F, G and H), lead one to decide on three clusters. But comparing the membrane time constants in Figure 3.20 I against Figure 3.20 J and the first latency at rheobase in Figure 3.20 K against L indicated that C3 and C4 of C=4 are different and can be separated. In addition, the similarity score was calculated between the k-means and the Ward clustering for different cluster numbers (see Tab. 3.14) showing the highest score at C=4.
We decided to go into further detail of the data of C=4 clusters. Table 3.15 summarizes the cell numbers calculated by k-means and Ward clustering for all cluster members and the total cell numbers of each cluster. The largest overlap regarding the k-means clustering is for C1 but the cell numbers of the other clusters show also similar results between Ward and k-means clustering.

Cluster	Ward C1	Ward C2	Ward C3	Ward C4	
K-means C1	240	11	1	0	$\Sigma = 252$
K-means C2	1	68	7	0	$\Sigma = 76$
K-means C3	0	18	18	11	$\Sigma = 47$
K-means C4	0	6	19	17	$\Sigma = 42$
	$\Sigma = 241$	$\Sigma = 103$	$\Sigma = 45$	$\Sigma = 28$	$\Sigma = 417$

Table 3.15: Summary of the intersections of cell numbers calculated by k-means and Ward clustering for four clusters and the total cell number for each cluster. Cluster analysis was performed by Johannes Nagele.

An illustrative arrangement of the resulted Ward clusters is depicted in Figure 3.21, in the dendrogram. This is a typical illustration of the hierarchical Ward clustering which is not possible to plot for the k-means clustering. Setting a point of intersection, as illustrated by the dashed line, revealed four clusters and gives you a nice overview of the Ward clustering.

In the following section, basic properties, which have already been shown for all cells together (see Section 3.1) and the suggested features will be represented for each cluster of the four cluster of the k-means clustering and if possible assigned to a certain cell type.

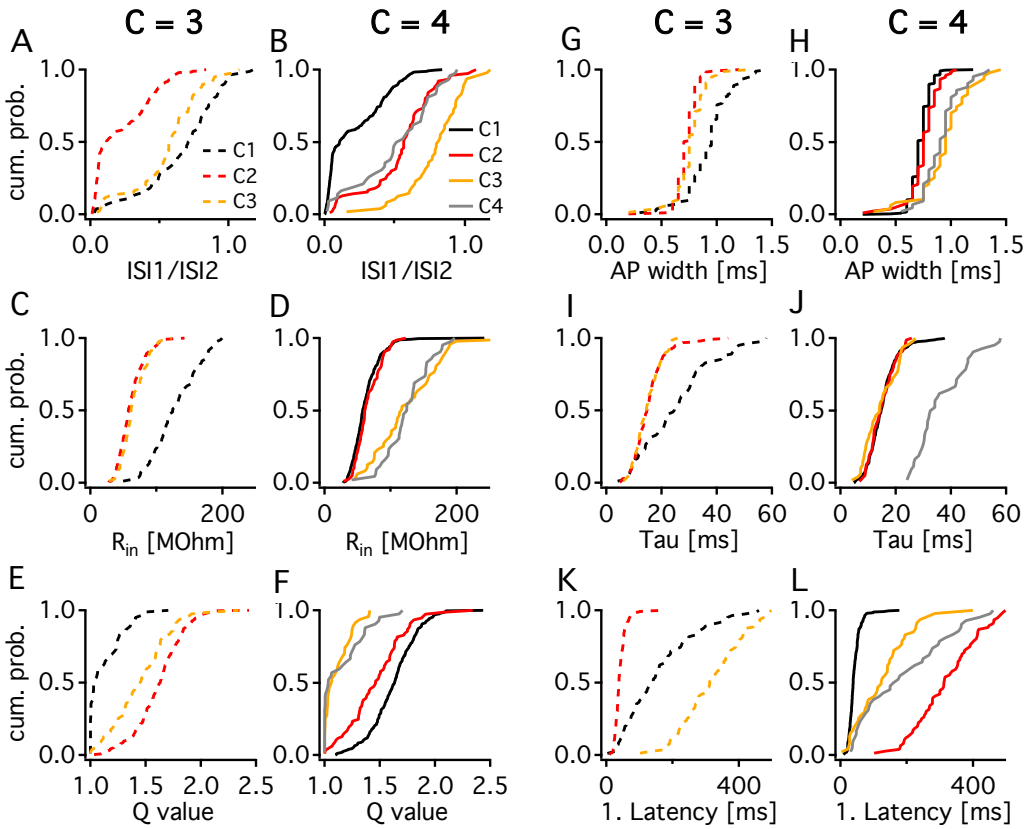

Figure 3.20: Comparison of the cumulative histograms of the k-means clustering of the selected features between three (C=3) and four clusters (C=4): (A) and (B) ISI1/ISI2 ratio; (C) and (D) R_{in}, input resistance; (E) and (F) Q value; (G) and (H) AP width; (I) and (J) tau, time membrane constant; (K) and (L) latency at rheobase. Colored lines indicate the different cluster groups.

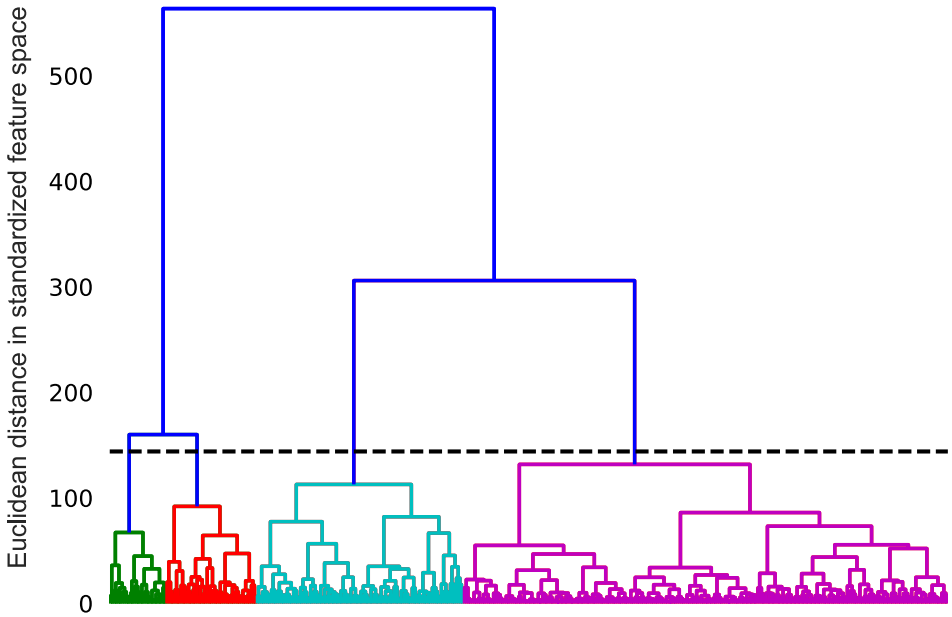

Figure 3.21: This dendrogram illustrates the arrangement of the clusters computed by hierarchical Ward clustering. The black dashed line represents the point of intersection resulting in four clusters, which are distinctly colored. This figure was provided by courtesy of Johannes Nagele.

3.7.1 *Basic properties of clustered mEC cells*

A non-parametric Kruskal-Wallis test was used to compare the selected features and the electrophysiological properties of the four clusters which are presented with their means and standard deviations in Table 3.16. The resulting significant p values are listed in Table 3.17 and show that all tested parameters are significantly different within the four clusters. Figure 3.22 shows the data from Figure 3.2, separated in the four different clusters resulting from the k-means clustering. The cumulative histograms and the scatter plots clearly illustrate that clusters C1 and C2 are more similar in their resting membrane potential (A), input resistance (B), capacitance (C), sag (D), resonance frequency (E) and voltage threshold (F). These similarities can also be read out from the listed means in Table 3.16. In contrast, C3 and C4 are also very similar in their basic properties to one another. The only parameter which separates the four clusters very distinctly is the latency of the first suprathreshold response shown in Figure 3.20 L. The majority of C1 cells has a very short latency, whereas the C2 cluster which is otherwise very similar has a very long latency, even longer than C3 and C4. On the other hand, there is quite a substantial overlap (Fig. 3.22 D) in the case of the sag, which is very similar for ~50% of all cells in each cluster. For the other 50%, the sag is either present or absent (see Fig. 3.22 D, G, H and I). From these results one can infer that cells of C1 represent the typical SC described by Alonso and Klink (1993) with a pronounced sag, resonating to frequencies in the theta range and a very short latency to the first spike at rheobase as a consequence of the sag response to depolarizing currents. In contrast, cluster C4 could be assigned to PCs due to larger input resistances and acting as a low-pass filter. Around 50 % of C4 cells showed only a very small or no sag response and also the latency to the first spike is much longer than C1 cells pointing towards PCs (Alonso and Klink, 1993; Canto and Witter, 2012; Linden and Lopes da Silva, 1998; Erchova et al., 2004). Cluster C2 could be interpreted as a stellate-like cell with long latencies or as the described intermediate SCs (Fuchs et al., 2016). Because of the small capacitances and the higher input resistances cluster C3 could be classified as interneurons. Examples to illustrate each cluster cell type will be shown in a following subsection (see Section 3.7.3).

In summary, we divided cells from mEC layer II into four different groups using automated cluster analysis, which matched the cell types described in the literature.
We will now turn in the next subsection to the question of whether biophysical properties of neurons can be used to predict the presence or absence of a DAP.

Char.	C1	C2	C3	C4
ISI1/ISI2	0.22± 0.2	0.55± 0.24	0.79±0.20	0.52 ±0.27
R_{in}	62.27±22.5	66.13±19.3	126.3±54.0	126.1±34.0
Q value	1.62±0.215	1.47±0.27	1.1 ±0.12	1.16 ± 0.199
AP width	0.77±0.00094	0.75±0.137	0.9±0.24	0.92±0.17
tau	15.17±5.41	14.98±4.60	15.03±7.2	36.54±9.42
Latency	41.69±19.02	318.6±93.6	127.6 ± 83.3	190 ±131
E_{rest}	-62.82±4.09	-64.29±4.45	-69.89±7.68	-69.13±8.64
Cap.	253±77.5	235.1±69.1	139.1±81.6	317.6±158
sag	-2.375±0.85	-2.41±0.98	-1.621±2.01	-1.885±1.56
$f_{resonance}$	6.248±1.13	5.518±1.47	2.567±1.49	2.153±1.81
volt. thr.	-41.62±5.95	-40.41±6.68	-37.07±8.02	-37.33±11.4

Table 3.16: Features on which the k-means clustering was applied to and basic electrophysiological parameters for the different clusters. Values are means ± SD. ISI1/ISI2 ratio; R_{in}, input resistance;Q value; AP witdh, action potential half width; tau, time membrane constant; latency; E_{rest}, resting membrane potential; Cap.,membrane capacitance; $f_{resonance}$, resonance frequency; volt. thr., voltage threshold.

Char.	p value
ISI1/ISI2	<0.0001
R_{in}	<0.0001
Q value	<0.0001
AP width	<0.0001
tau	<0.0001
Latency	<0.0001
E_{rest}	<0.0001
Cap.	<0.0001
sag	<0.0001
$f_{resonance}$	<0.0001
volt. thr.	0.0003

Table 3.17: Statistical tests of the selected features on which the different clusters were calculated from and statistical tests of the comparison of electrophysiological parameters of the different clusters. P values were calculated with the non-parametric Kruskal-Wallis test. Significance level: $p < 0.05$.

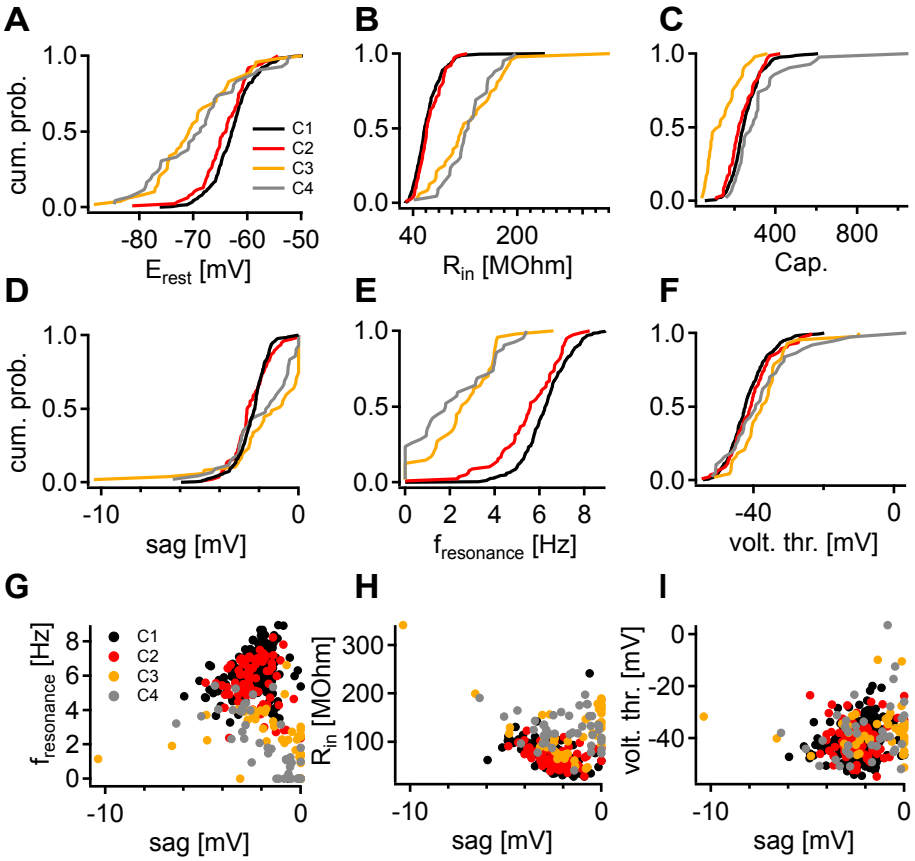

Figure 3.22: Cumulative histograms of the basic properties for the four different clusters resulting from the k-means clustering in layer II of the mEC (A-F). Scatter plots of resonance frequency, input resistance and the voltage threshold plotted against the sag (G-I). Subfigures B was already illustrated in subfigure D of Figure 3.20.

3.7.2 *Depolarizing afterpotentials of clustered cells*

We were interested in using cluster analysis to find out whether a DAP can be predicted by a set of electrophysiological parameters and therefore be assigned to a certain cell group. Thus, we left out the DAP features from the k-means cluster analysis so that we could test whether the remaining parameters could predict the DAP properties. The DAP properties for four clusters are illustrated in Figure 3.23 and Table 3.18.

A comparison of the DAP deflection and width across all four clusters showed significant differences in the medians (non-parametric Kruskal-Wallis test, see Tab. 3.18). The cumulative histograms of Figure 3.23 illustrate that the majority of cells in clusters C1 and C2 exhibit a pronounced DAP deflection (> 2 mV). The mean values of the DAP measures and their standard deviations are listed in Table 3.18. C4 cells display a smaller DAP but it is still present, whereas the majority (~80%, value was read out from Fig. 3.23 A) of C3 cells show either a very small or no DAP. Only a minority of C3 representatives (~20 %) elicited pronounced DAPs (see Tab.3.18 and Fig. 3.23 A, C, E and G). An inspection of the DAP width showed less clear separation. Cluster C4 deviates most from the others with the longest DAP width (see Tab.3.18 and Fig. 3.23 B, D, F and H).

Figures 3.23 C-H illustrate DAP deflection and width plotted against different measured cell properties to see possible influences. Yet, given that all clusters comprise DAPs, our results do not support the idea that presence of DAPs alone can be predicted by certain cell features to categorize them into specific principal cell types.

Char.	C1		C2		C3		C4		p value
Defl.	2.61	±1.5	2.37	±1.3	1.41	±1.6	2.2	±1.85	<0.0001
Width	17.4	±6.2	16.1	±5.2	16.3	±5.4	25.1	±13.6	0.0042

Table 3.18: Means ± SD of the DAP properties for the four different clusters of mEC layer II cells. Statistical tests comparing the electrophysiological parameters of the different clusters were performed with the non-parametric Kruskal-Wallis test. Significance level: $p < 0.05$.

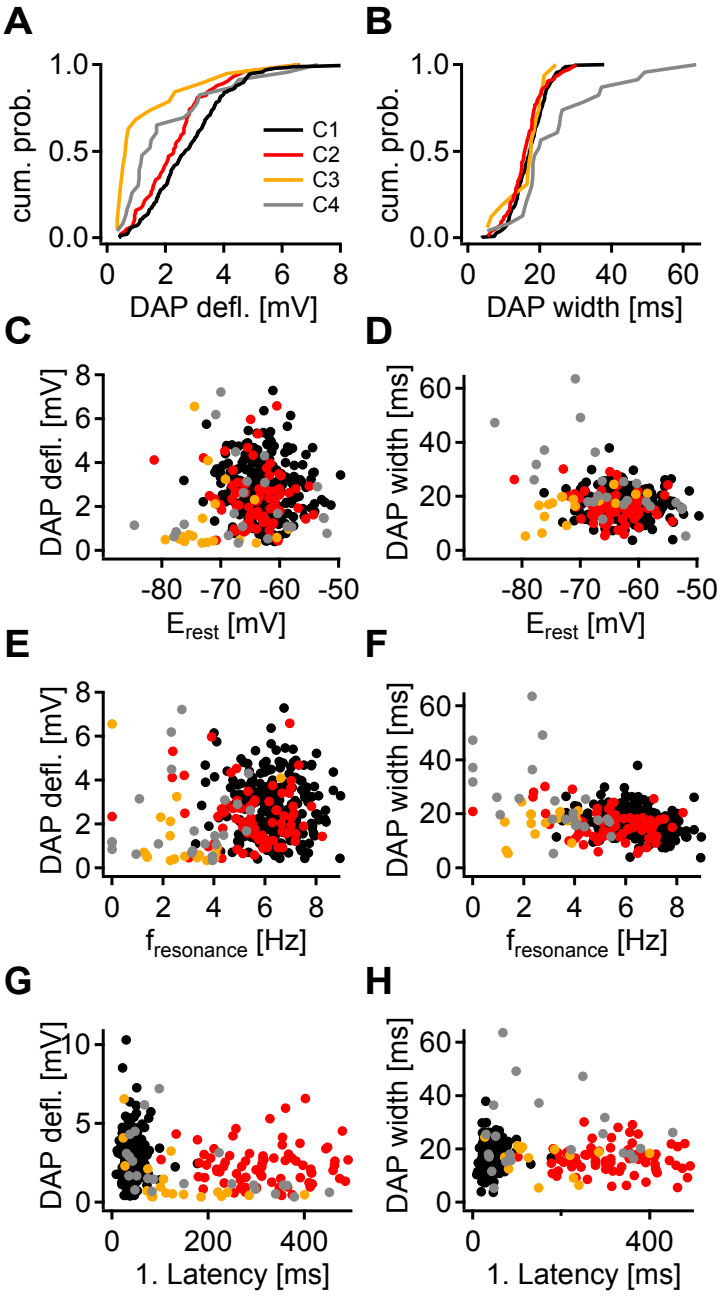

Figure 3.23: DAP properties for the four different clusters of mEC layer II cells. (A-B) Cumulative histograms of DAP characteristics: deflection and width. (C-H) Scatter plots with DAP deflection or DAP width in relation to the membrane resting potential, resonance frequency and voltage threshold.

3.7.3 *Clustering examples*

The following three figures (Fig. 3.24, 3.25 and 3.26) show example mEC layer II neurons that were randomly selected from each cluster. The raw traces corresponding to the different standard stimulus protocols are also plotted for illustration purposes.

In Figure 3.24, the cell from the C1 cluster responded similarly to the standard mEC layer II stellate cell described by Alonso and Klink (1993). The response shows a pronounced sag to a negative current injection (blue trace), a subthreshold sag to a positive current injection (light grey trace), a pronounced DAP (dark grey trace), a short latency (dark grey trace) of the first suprathreshold response and a very short ISI at the beginning of the current injection (black trace). The magnified inset clearly illustrates this short inter-spike-interval. The pronounced DAP is repeated in Figure 3.25 C1 in response to the standard ramp protocol that elicits an AP. The resonating response to the ZAP stimulus is shown in Figure 3.26 C1.

The example cell from the C2 cluster showed a more pronounced negative sag, but a less pronounced positive sag and DAP than the C1 example cell. The first spike came late in the third third of the stimulation protocol, which is characteristic to the long latencies of this cluster (see Fig. 3.7 F). The representative cell from the C2 cluster did not burst at the beginning which points together with the less pronounced rebound and DAP towards an intermediate SC type.

In contrast, the representative cell from the C3 cluster displayed a much broader sag than the examples from clusters C1 and C2, but showed no sag response to a positive current injection. A fAHP after the AP leads to the impression of a sharp minimum between two spikes (see Fig. 3.24). Three spikes were elicited within the first suprathreshold response, compared to only one spike in the examples from clusters C1 and C2. The representative cell from cluster C3 also did not show bursting at the beginning of the stimulation and resonated at low frequencies between 1-1.5 Hz with a transition to a low-pass filter. These properties of the representative neuron from cluster C3 is consistent with it being an interneuron.

The fourth cell cluster, C4, had generally similar properties to the standard mEC layer II pyramidal neuron, but with a broader sag than the examples from cluster C1 and C2, yet less broad than C3. The representative C4 cell responded with a rebound to positive current injections and resonates to low frequencies similar to that of C1 and C2 representative cells, albeit less

pronounced and smaller. The first elicited spike came late with no following bursts.

Taken together, our results indicate that DAPs could facilitate bursting as illustrated in Section 3.5, are not specific to a certain type of mEC cells, and that their origin cannot be attributed to a single ion channel as shown in Section 3.4.

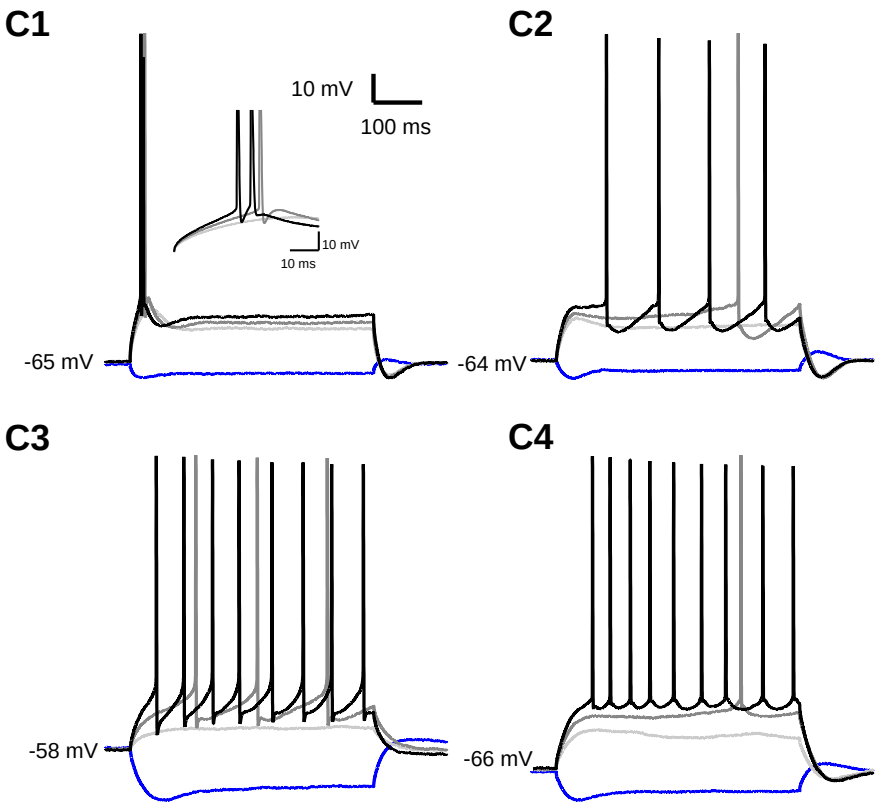

Figure 3.24: Membrane potential responses of a representative cell from each cluster in response to the IV stimulus/protocol. The blue trace illustrates the first voltage deflection in response to a -150 pA current injection. Light gray illustrates the last subthreshold response, dark grey the first and black the second suprathreshold response. Different resting membrane potentials are indicated. Inset in C1 is a zoom in of the spikes.

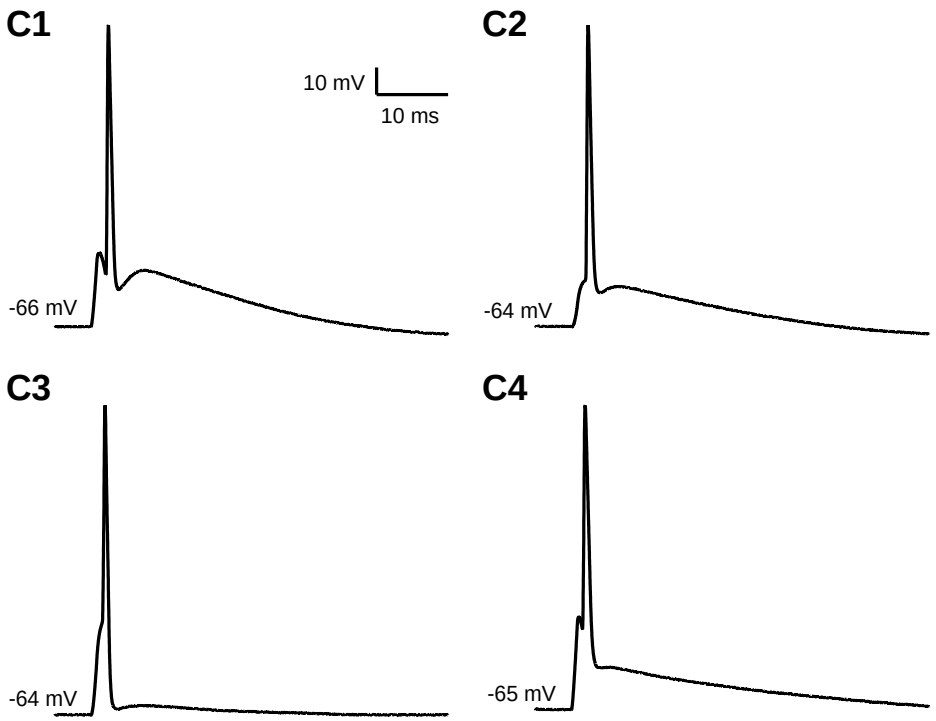

Figure 3.25: Depolarizing afterpotentials of a representative cell from each cluster. First suprathreshold single AP elicited by a short current ramp (0.8 ms increase, 1.2 ms decrease) followed by a DAP. Different resting membrane potentials are indicated.

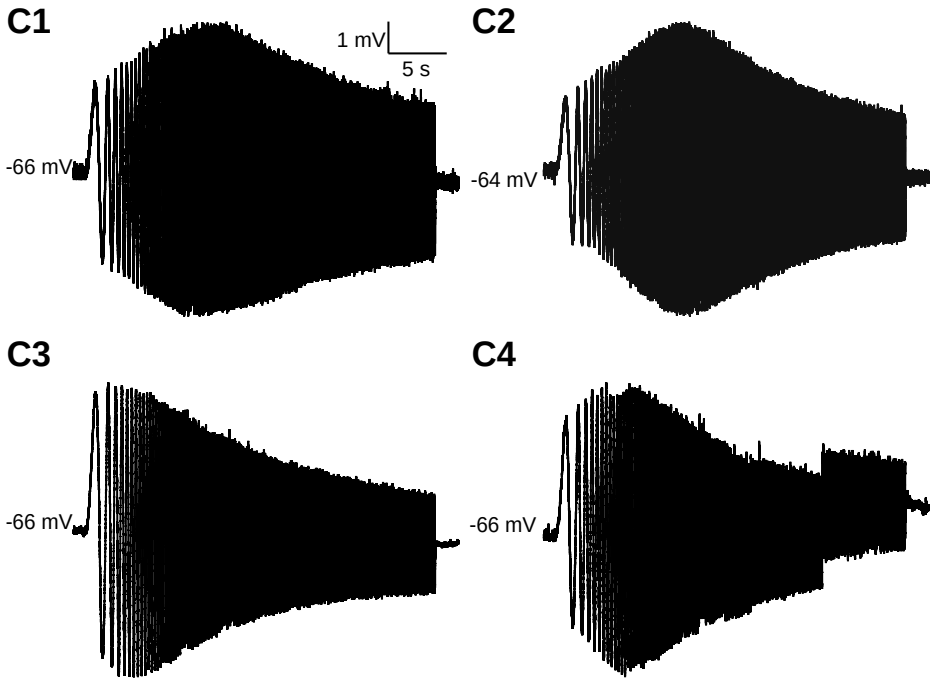

Figure 3.26: Membrane potential responses of a representative cell from each cluster in response to ZAP stimulation. Different resting membrane potentials are indicated.

As we have seen in Section 3.3 and demonstrated in Section 3.5, hyperpolarizing mEC layer II cells further enhances the AP probability by increasing the DAP amplitude. Thus, we argue that the DAP and the membrane oscillations combined with the depolarizing ramp which occurs when an animal crosses a grid-field (Domnisoru et al., 2013; Schmidt-Hieber and Häusser, 2013), as shown in Figure 1.12 in the upper trace, are well suited to amplify the firing probability and induce doublets or bursts.

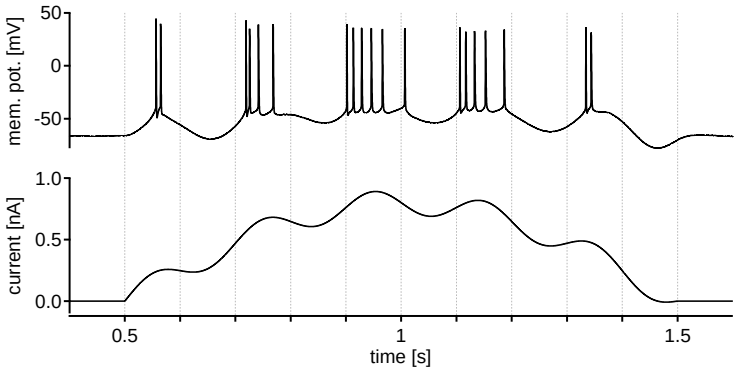

Figure 3.27: Sinusoidal stimulus example: the lower panel illustrates the injected current of a sinusoidal stimulus (1 s) with a frequency of 5 Hz. The corresponding cell membrane response is shown in the upper panel. The stimulus consists of a slow half-sine oscillation and a fast sinusoidal oscillation.

To test this hypothesis, we performed in vitro patch-clamp recordings and injected sinusoidal currents (fast sinusoidal oscillation) that are modulated by a slow depolarization wave (slow sinusoidal oscillation), partially mimicking the in vivo firing response (see Methods 2.4.5). The fast sinusoidal oscillation was meant to mimic theta inputs. The slow sinusoidal oscillation, which was only a half sine cycle, was designed to imitate the slow depolarization ramp from the Domnisoru et al. (2013) and Schmidt-Hieber and Häusser (2013) publications. An example of this sinusoidal stimulus is shown in the lower panel of Figure 3.27, with the corresponding cell response in the upper trace. Under normal in vivo conditions, the time duration of a passage through a grid field varies (e.g. in the data of Domnisoru et al. (2013) and Schmidt-Hieber and Häusser (2013)). As a consequence, we chose different periods for the half sine cycle (1-10 seconds). We recorded from 63 mEC layer II cells and varied the duration and the frequency of this stimulus, as shown in the following table:

Length/Freq.	20 Hz	5 Hz	$f_{resonance}$	Control
10 s	√	√	√	√
5 s	-	√	√	-
2 s	√	√	√	-
1 s	√	√	√	-

Table 3.19: Overview of the variations in the sinusoidal stimulus. Ticks indicate the tested conditions. A stimulation of 10 seconds was also applied without the fast oscillation and labeled as control. Stimulus conditions with a length of 10 seconds were repeated at least twice and the shorter stimulus conditions were iterated 10 times each.

3.8.1 *Inter-spike-interval distribution*

Short doublets are rapid sequences of two action potentials. To look for these, I will now analyze the ISI distributions. Measured ISIs for the different stimulus conditions are illustrated in Figure 3.28 A. The majority of spikes are elicited within an interval of 0-50 ms, except for the responses to the 10 second stimulations, which are more equally distributed. Secondly, we defined short doublets/ISIs as two APs that succeed each other within a time window of 10 ms (short ISI < 10 ms). This time window was chosen too extend beyond the time gap between AP and the following DAP maximum (see Fig. 3.3 H). In further analyses, I will drop the results from the 10 second long stimulations, as these did not produce short ISIs, as indicated by the red line (Fig. 3.28 A) and shown in Figure 3.28 B (zoom in of A). In conclusion, short ISIs comprise only a small fraction of 2.2% of all ISIs (3453 short ISIs out of 153902 ISIs), but could be elicited in all short (1 - 5 seconds) stimulus conditions. In vivo, the fraction of short ISIs was much higher (Latuske et al., 2015).

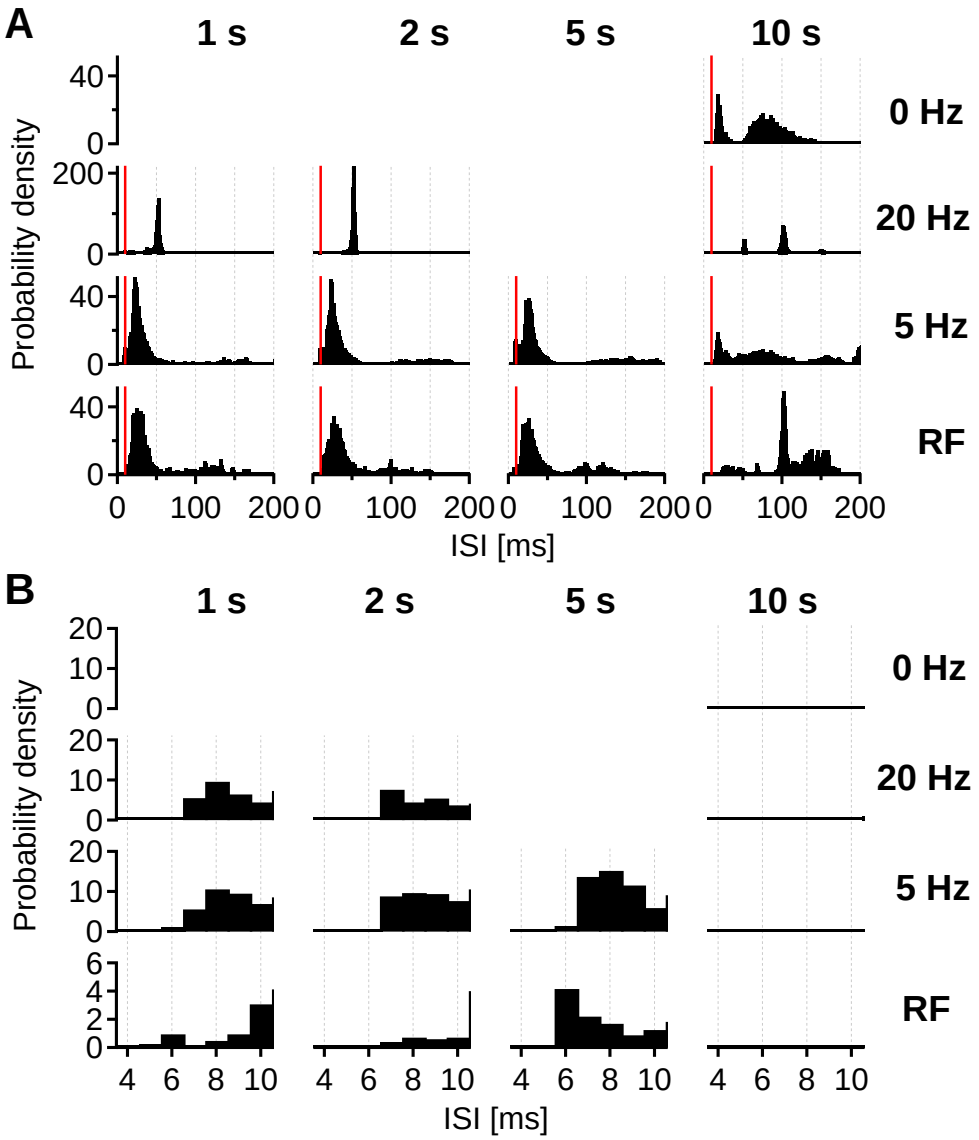

Figure 3.28: ISI histograms: (A) all measured ISIs within the listed conditions for all cells normalized to the probability density. The red lines indicate the 10 ms border. (B) Zoom in of the range between 4-10 ms of (A) for the short ISIs. White areas within the plots were not measured conditions, whereas in (B) within the 10 second column short ISIs were not elicited. RF is another abbreviation for resonance frequency .

3.8.2 *Distribution within fast and slow oscillations*

Next, we looked at the distribution of spikes with respect to either just the fast sinusoidal oscillation (Fso) (Fig. 3.29) or just the slow sinusoidal oscillation (Sso) (Fig. 3.30). These histograms are not averaged over cycles and are not normalized, so as to highlight the distribution of short ISIs (in red). The majority of spikes occurred in the rising phase of the Fso, except in the 10 second 20 Hz stimulation, where cells tended to fire more at the peak and during the falling phase. In the control condition there was no fast sinusoidal stimulus and the resulting distribution of spikes was uniform as expected. We examined the Fso distributions, because we were interested to see if these cells phase-lock. Fernandez, Malerba et al. (2013) could show that SCs in the mEC preferably spike phase-lock to theta inputs. Theta inputs (5-10 Hz) would be comparable with $f_{resonance}$ and 5 Hz. Responses elicited by the resonance frequency are less sharp and do not mirror the Fso as precisely as the 5 Hz and 20 Hz stimulations. This is caused by grouping data of different cells with different resonance frequencies together. But between 20 Hz and 5 Hz no difference regarding the spike phase-locking is visible.

Plotting the phases of the spikes in the Sso mirrors the slow oscillation as well as the fast oscillation, which is again only missing in the control plot. Cells spiked more as they approached the peak of the Sso (Fig.3.30), which was expected because the cells get closer to threshold by the depolarizing ramp/slow half sine wave.

All cells exhibited a discretisation effect and can be observed in responses to the resonance and the 5 Hz stimulations. This effect can be explained by the Fso starting always with the same fast cycle. Therefore one could expect five niveaus at 1s/5Hz per half-cycle, 10 niveaus at 2s/5Hz and 25 niveaus at 5s/5Hz.

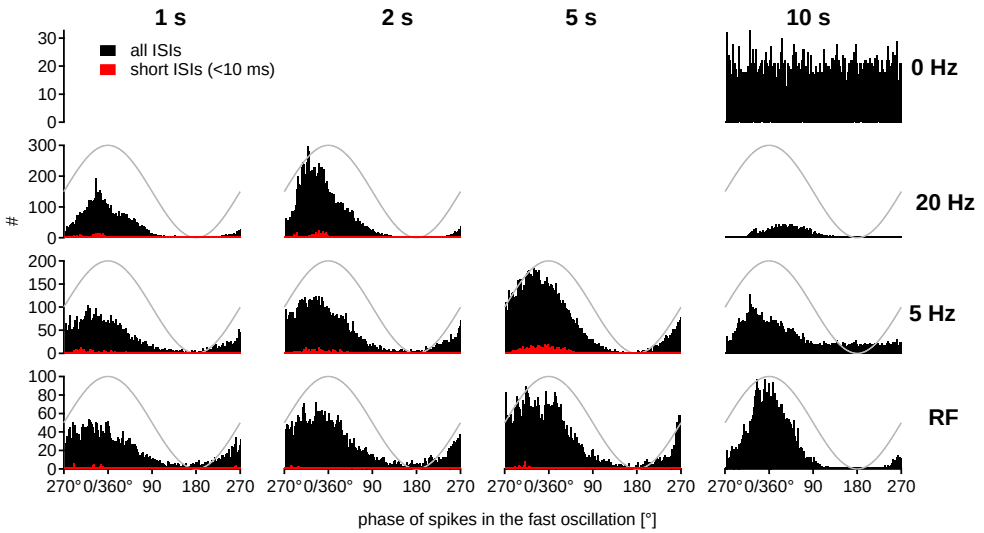

Figure 3.29: Distribution of all ISIs (black) and the short ISIs (red) for the stimulation of the fast oscillation phase (grey) for all measured conditions. The histograms are not normalized.

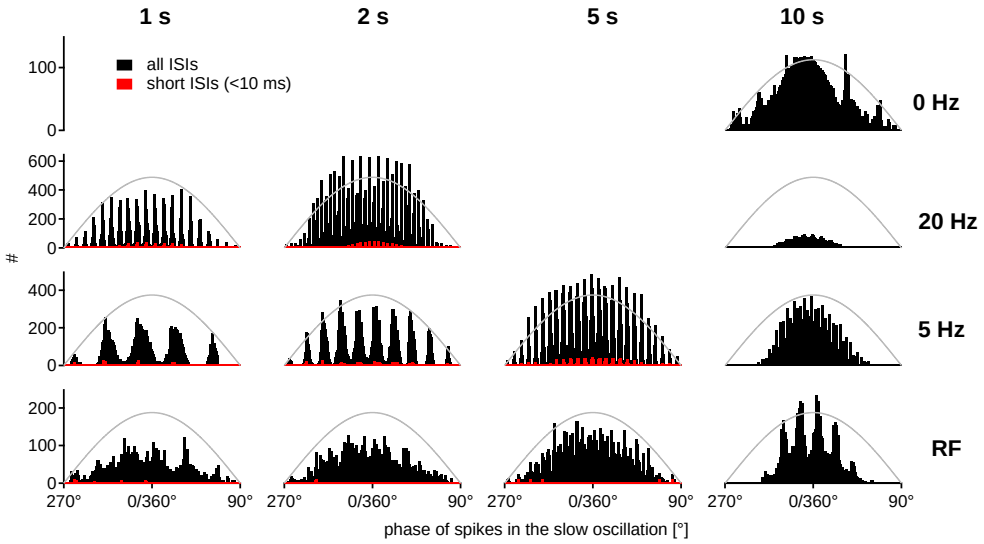

Figure 3.30: Distribution of all ISIs (black) and the short ISIs (red) for the stimulation of the slow oscillation phase (grey) for all measured conditions. The histograms are not normalized.

3.8.3 *Phase of spikes with short inter-spike-intervals*

As demonstrated above in Section 3.2, the time between DAP and preceding AP was between 2-7 ms. Therefore, to include all possible ISIs within the DAP range we analyzed our data from 0-10 ms of 23 remaining cells. In addition, the results of the k-means clustering were adopted to assess how different cell types respond to this stimulation. Therefore the assigned clusters of the 63 measured cells were taken from the results of dividing into four clusters (C=4). We also considered the DAP deflections of the four clusters in Figure 3.31 to see if a short ISI amplified by a DAP would be even possible. Illustrated DAP deflections and membrane resting potentials were not measured within the sinusoidal stimulation protocol. It was not possible to measure DAPs definitively, because the fast sinusoidal current injections could be confounded with DAPs. This for example could happen when the current intensity is too low (at the beginning of the stimulation) to elicit more than one spike and the sine wave modulation mimics a DAP after the elicited spike. Therefore we used DAPs after an AP elicited by a short current ramp. Moreover, we divided the slow ramp into subintervals to separate the effects of Sso and Fso.

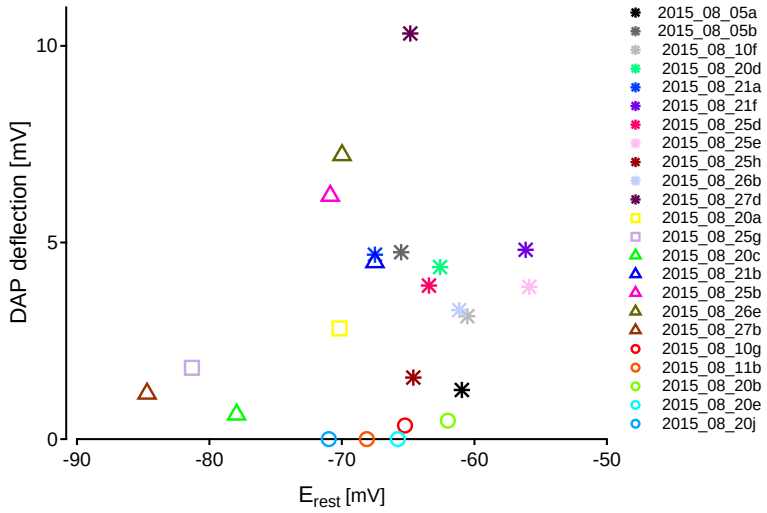

Figure 3.31: DAP deflection as a function of the membrane resting potential. DAPs were measured from single APs elicited by a short current ramp and correspond to the cells which were stimulated with sinusoidal stimuli. Different clusters are indicated as $*$ for stellate cells (C1), $\square$ for intermediate cells (C2), $\circ$ for interneurons (C3), $\triangle$ for pyramidal cells (C4).

Fast sinusoidal oscillation

A separation of the ISI responses of the four different clusters (C1: n = 11, C2: n = 2, C3: n = 5, C4: n = 5) depending on the phase of the first AP of a short burst within the Fso is shown in Figure 3.32. Prominent responses are listed in the following for each cluster:

- C1: All cells displayed a DAP (see Fig. 3.31) and therefore short ISIs could have been enhanced by the DAP. The majority of spikes occurred in the rising phase leading to an asymmetric distribution. Spikes are distributed over the whole range from 250°-360/0° in response to the 5 Hz stimulation, whereas spikes are closer to 360/0° in response to the 20 Hz stimulation. Shorter ISIs (> 8 ms) only emerged during the 5 Hz stimulation with stimulation durations of 1 and 2 seconds. The C1 cluster matches perfectly with the described properties of the typical stellate cells (Alonso and Klink, 1993; Canto and Witter, 2012; Nolan, Dudman et al., 2007). Due to this fact and including the DAP appearance and the pre-hyperpolarization amplification effect of the DAP we have expected that these cells elicit short ISIs in the rising phases and more ISIs at 5 Hz or at the $f_{resonance}$ than at 20 Hz.

- C2: The two cells of this group showed both a DAP deflection (see Fig. 3.31). One of the two cells was strongly driven by the injected current, spiking nearly symmetrically around the peak, with the ISI distributed over the whole range. Our clustering classified this group as intermediate cells. This assignment and the presence of a DAP is contrary to our expectation that these cells might be interneurons. Indeed, these neurons could be driven by the current and spike over the whole phase range of the different stimuli like cell example 2015-08-25g, just like interneurons.

- C3: This cluster group showed either no DAP deflection or a very small small DAP (< 1 mV, see Fig. 3.31). The majority of spikes occurred on the rising phase. In response to the 20 Hz stimulation, the spikes also occurred closer to the peak of the fast oscillation, in contrast to the slow envelope that mas modulated (5 Hz/$f_{resonance}$). This cluster represented interneurons of layer II. The absence of DAP coincided with no short ISIs and no strong modulation by the injected current like cell example 2015-08-25g.

- C4: All cells of this cluster had a DAP (see Fig. 3.31). The majority of spikes occurred on the rising phase. C4 cells showed the same trend as cells of clusters 1 and 3, congregating closer to the peak in response to

20 Hz than at 5 Hz or at the resonance frequency. Clustering predicts that these cells represent pyramidal neurons. On account of this and the elicited DAPs we expected a short ISI production. But due to a absent resonance in PCs the ISIs could have been elicited by every frequency.

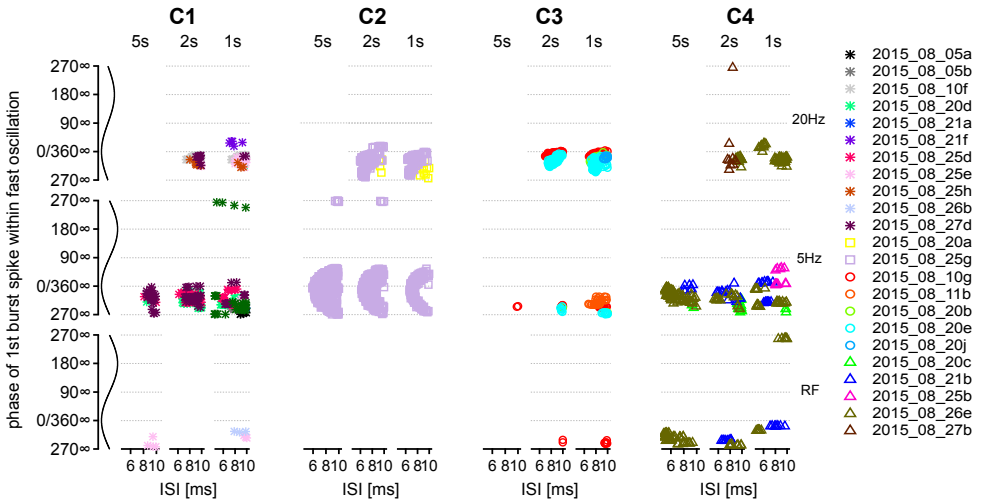

Figure 3.32: Phase of the first spike of a short ISI within the fast oscillation of the different stimuli. Colors mark all measured cells and their names are indicated in the legend. White areas indicate conditions that were not measured (20 Hz at 5 seconds). Different symbols represent the different cell types: $*$ for stellate cells (C1), $\square$ for intermediate cells (C2), $\circ$ for interneurons (C3), $\triangle$ for pyramidal cells (C4).

Slow sinusoidal oscillation

Figure 3.33 shows the ISI responses of the four different clusters based on the phase of the first AP of a short ISI within the slow oscillation for all measured conditions:

- C1: In response to the 5 Hz or the resonance frequency stimulation, spikes were more distributed over the slow oscillation. During the 20 Hz stimulation, spikes also occurred close to the peak. Cells of this cluster also jittered. As this cluster represents the typical SCs we expected that the ISIs occur more often on the rising phase due to the pre-ramp-hyperpolarization.
- C2: The spikes are equally distributed over the whole stimulation. In contrast to all other cells, the second representative neuron of cluster 2 spikes more during the decrease of the slow oscillation. For this cluster we had expected a similar behavior to cluster 1 but with fewer short ISIs due to the reduced overshoot at stimulation start (see Fig. 3.24 C2).
- C3: These cells show the same behavior as representatives from cluster 1 in response to the 20 Hz, the 5 Hz and the resonance frequency stimulation. Here again due to the absence of DAPs we presumed either no short ISIs or strongly driven by the current injection.
- C4: Three out of four cells from this cluster fire either at the beginning or at the end of the slow oscillation during the 5 Hz stimulation. In response to the 20 Hz stimulation, the majority of spikes again occurred close to the peak. Cell representatives also jitter. Based on the fact that this cluster probably represents PCs and the DAP presence in all five cells which, according to Alessi et al. (2016), depends on voltage-gated Na^+ channels, we expected a prevalence of short ISIs in the middle region of the slow oscillation.

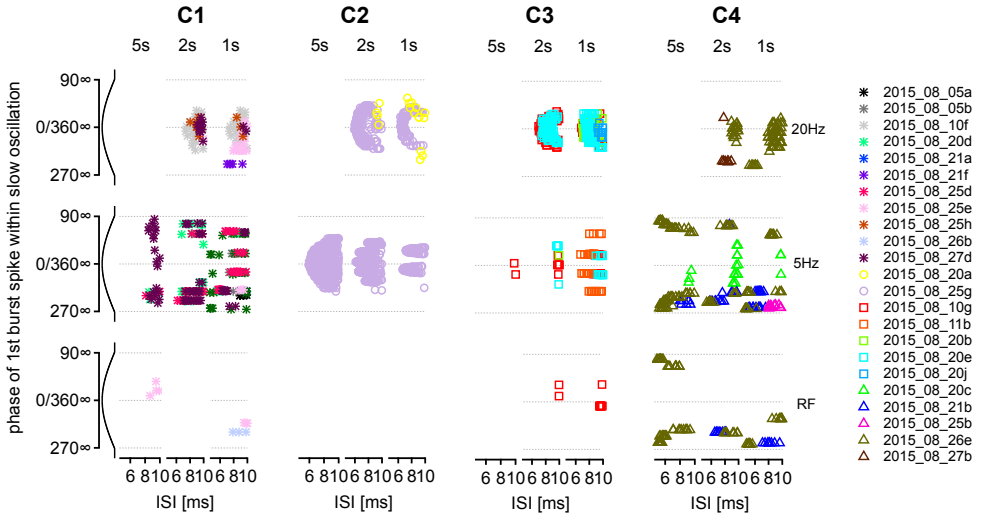

Figure 3.33: Phase of first spike of a short ISI within the slow sinusoidal oscillation of the different stimuli. Colors mark all measured cells and their names indicated in the legend. White areas indicate conditions that were not measured. $*$ for stellate cells (C1), $\square$ for intermediate cells (C2), $\circ$ for interneurons (C3), $\triangle$ for pyramidal cells (C4).

3.8.4 *Statistics on phase differences*

Given the small number of spikes during stimulations with the $f_{resonance}$ and the proximity of the resonance frequencies to 5 Hz, the results of the $f_{resonance}$ stimulation were disregarded in the subsequent analysis. In the last step of the analysis of this experiment, we calculated the difference between the phase at which the first spike of a doublet occurred and the sinusoidal peak. The idea behind this is to see whether cells in different clusters reacted differently not only within one condition but also across different frequencies. The results are summarized as mean ± standard deviation for each condition (Fso in Fig. 3.34; Sso in Fig. 3.35 B). The stimulus conditions and the clusters were compared in three different ways.

Fast sinusoidal oscillation

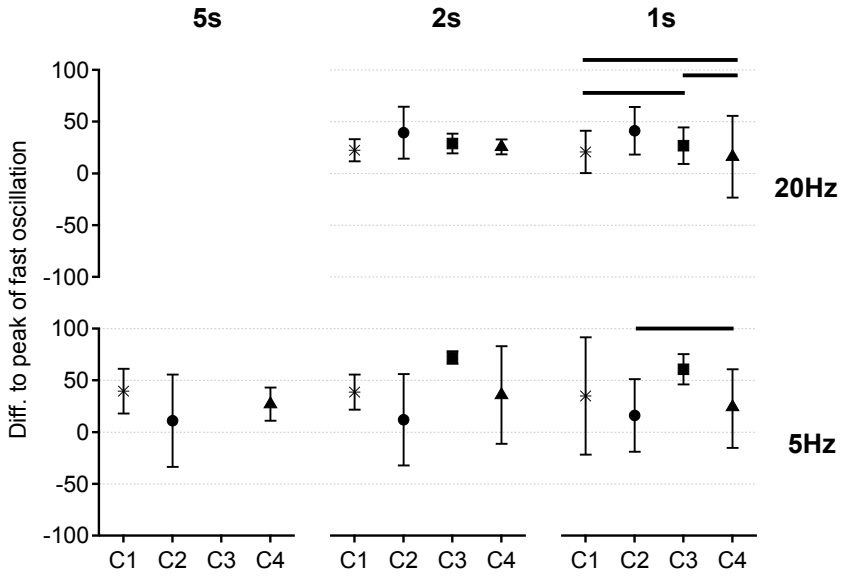

Figure 3.34: Means ± SD of the phase difference of the first spike of a doublet within the fast oscillation to the peak of the phase for the different cluster and the different stimulus conditions. Horizontal black lines between clusters indicate non-significant results (non-parametric Mann-Whitney test). Remaining comparisons were significantly different at a significance level of $p < 0.05$.

First, we assessed each condition of the Fso for the presence of statistically significant differences (Kruskal-Wallis test). This revealed significant differences between the clusters for all conditions (see Tab. 3.20).

Freq./Length	5 s	2 s	1s
20 Hz		<0.0001	<0.0001
5 Hz	<0.0001	<0.0001	<0.0001

Table 3.20: Fast sinusoidal oscillation: P values of the comparison between clusters within each condition of the phase difference to the peak of the fast oscillation. Statistical significance was tested with the non-parametric Kruskal-Wallis test. Significance level: $p < 0.05$.

Second, a detailed comparison of all possible cluster variations within one condition was performed for all stimulations using a non-parametric Mann-Whitney test. The resulting p values are listed in Table 3.21. Note that the black lines in Figure 3.34 indicate non-significant differences between clusters. Within the stimulus conditions 20 Hz/2 sec, 5 Hz/5 sec and 5 Hz/2 sec, the clusters differed significantly from one another. In the condition 5 Hz/1 sec, all variations differed significantly, except for the comparison between C2 and C4. The opposite was true for the 20 Hz/1 sec stimulation, with a significant difference for the following comparisons: C1 and C2, C2 and C3, C2 and C4. These results are partially consistent with our expectations. Different stimuli durations should lead to qualitatively similar results. We expected that C1 and C4 (SC vs. PC) to show significant differences for all 5 Hz stimulations, which is what I also measured. Also the results between C1 and C3 (SC vs. Interneuron) match with our expectation and are significantly different. For the results between C1 and C2 (SC vs. Intermediate) or C4 and C2 (PC vs. intermediate) we had no clear forecast. Due to the intermediate cell classification these cells could respond more like SCs or more like PCs or completely different. But C2 significantly differed from C1 and C4. The same was true for the interneurons, as expected.

For the conditions stimulated with 20 Hz, we would have expected significant differences between C1/ C2/ C4 and C3 independent from the stimulus length which matches with the results. These expectations are based on the fact that interneurons do not show resonance properties leading to no big differences to the 5 Hz stimulation. In contrast to that, we had no clear expectation how the three remaining clusters would differ from each other and apparently there was no significant difference in the 20 Hz /1 sec condition.

Length/Freq.	20Hz/5s	20Hz/2s	20Hz/1s
C1 - C2			0.7936
C1 - C3		<0.0001	<0.0001
C1 - C4		0.0123	0.9938
C2 - C3		0.0005	<0.0001
C2 - C4		0.0454	0.5319
C3 - C4		0.0231	<0.0001
Length/Freq.	5Hz/5s	5Hz/2s	5Hz/1s
C1 - C2		<0.0001	<0.0001
C1 - C3	<0.0001	<0.0001	<0.0001
C1 - C4	0.0076	<0.0001	0.0004
C2 - C3		<0.0001	<0.0001
C2 - C4		0.0002	<0.0001
C3 - C4	<0.0001	<0.0001	0.0610

Table 3.21: P values of detailed comparison between clusters of one conditions for the phase difference to the maximum phase of the fast sinusoidal oscillation. Statistical significance was tested with the non-parametric Mann-Whitney test. Significance level: $p < 0.05$.

Third, we again used the Mann-Whitney test to match each cluster with 20 Hz and 5 Hz for both stimuli duration with the results listed in Table 3.22. Comparing 20 Hz and 5 Hz stimulated for 2 seconds revealed highly significant differences between both frequencies for all four clusters. The same results were obtained for 20 Hz/5 Hz stimulated for 1 second, except that C4 did not differ significantly between both frequencies. We compared these two frequency conditions for different stimulus durations, based on the resonance property which is very present in C1 (SC), C2 (intermediate). Clusters C3 (interneuron) and C4 (PC) respond with lower resonance frequencies or are low-pass-filter. Therefore we assumed a significant difference between 5 Hz condition and 20 Hz condition at least for C1 and C2 which is true for both clusters. However, cluster C4 differs significantly between both frequencies for the 2 sec stimulus duration, whereas the 1 sec duration was not significantly different which is also surprising.

Cluster/Cond.	20Hz/5Hz 2s	20Hz/5Hz 1s
C1	<0.0001	<0.0001
C2	<0.0001	<0.0001
C3	<0.0001	<0.0001
C4	0.0025	0.1232

Table 3.22: Fast sinusoidal oscillation: p values of the Mann-Whitney test for the comparison of different conditions within one cluster. Significance level: $p < 0.05$.

Slow sinusoidal oscillation

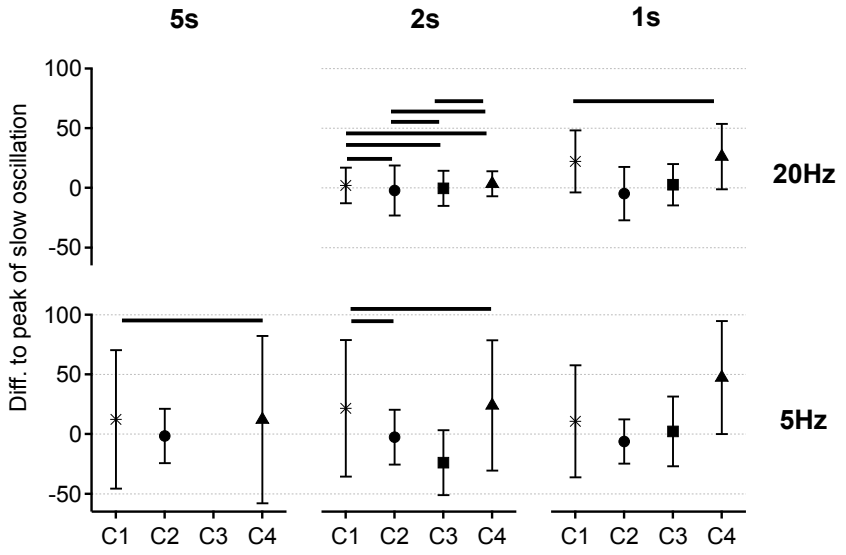

Figure 3.35: Means ± SD of the phase difference of the first spike of a doublet within the slow oscillation to the peak of the phase for the different cluster and the different stimulus conditions. Horizontal black lines between clusters indicate non-significant results (non-parametric Mann-Whitney test). Remaining comparisons were significantly different at a significance level of $p < 0.05$.

We performed the same three comparisons on these results for the Sso to show how symmetric the spiking behaviour was.

The first comparison analysis, in which we assessed each condition of the Sso for the presence of statistically significant differences revealed no significant differences between the four clusters within the 20 Hz/2 sec stimulation condition (non-parametric Kruskal-Wallis test). All other stimulus variations contained significant differences between the clusters (see Tab. 3.23).

Freq./Length	5s	2s	1s
20 Hz		0.3918	<0.0001
5 Hz	0.0003	<0.0001	<0.0001

Table 3.23: Slow sinusoidal oscillation: P values of the comparison between clusters of one condition for the phase difference to the peak of the slow oscillation. Statistical significance was tested with the non-parametric Kruskal-Wallis test. Significance level: $p < 0.05$.

Assigned clusters within a condition yielded the p values listed in Table 3.24 (Mann-Whitney test). Non-significant results are indicated in Figure 3.34 B. Stimulating with the 5 Hz/1 sec condition resulted in highly significant differences between all variations of the four clusters. In contrast, stimulating for 2 seconds yielded no significant difference between C1-C2 and C1-C4. Stimulating with 5 seconds also did yield a not significant result between C1-C4. Considering the Sso stimuli for 5 Hz we would have expected differences between the clusters based on the different cell properties as described before, but not between the different stimulus durations. It is interesting that clusters C1-C4 are not different which is against our assumption.

Comparing the 20 Hz conditions, the 1 second stimulus duration only revealed no significant differences between C1-C4. A second "control" analysis confirmed the results calculated with the Kruskal-Wallis test, namely, no significance. Also for the 20 Hz conditions we would have assumed differences between the clusters.

Concluding, mimicking in-vivo firing responses were not successful. So we could not lend support to our hypothesis that the characteristics of DAP and membrane oscillations combined with a depolarizing ramp amplify the firing probability and induce bursts.

Comparing excitation with a sinusoidal frequency of 20 Hz and with 5 Hz for 1 second showed no difference within clusters C1, C2 and C3, whereas

Length/Freq.	20Hz/5s	20Hz/2s	20Hz/1s
C1 - C2		0.4486	<0.0001
C1 - C3		0.2545	<0.0001
C1 - C4		0.6580	0.6498
C2 - C3		0.4234	0.0014
C2 - C4		0.3187	<0.0001
C3 - C4		0.2313	<0.0001
Length/Freq.	5Hz/5s	5Hz/2s	5Hz/1s
C1 - C2		0.0671	0.0115
C1 - C3	0.0366	<0.0001	<0.0001
C1 - C4	0.3793	0.6836	<0.0001
C2 - C3		0.0452	<0.0001
C2 - C4		0.0302	<0.0001
C3 - C4	0.0003	<0.0001	<0.0001

Table 3.24: P values of the comparison between clusters of one condition for the phase difference to the maximum phase of the slow sinusoidal oscillation. Statistical significance was tested with the non-parametric Mann-Whitney test. Significance level: $p < 0.05$.

C4 showed significantly different responses. The same comparison with a 2 second long stimulation revealed significant differences within C1, C3 and C4 (see Tab. 3.25). We assumed no differences between the varied stimuli durations, but due to the interplay of the Fso we expected significant differences between the frequencies.

Cluster/Cond.	20Hz/5Hz 2s	20Hz/5Hz 1s
C1	0.0001	0.6631
C2	0.8141	0.5119
C3	0.0015	0.5483
C4	0.0061	<0.0001

Table 3.25: Slow sinusoidal oscillation: p values of the Mann-Whitney test that compares the different conditions within one cluster. Significance level: $p < 0.05$.

4

DISCUSSION

4.1 SUMMARY OF RESULTS

In the present study, I performed whole-cell current-clamp recordings from mEC layer II cells in acute brain slices of mature rats and gerbils to demonstrate that depolarizing afterpotentials play an important role in the information processing of the entorhinal cortex.

Previous in vivo recordings in the rodent EC have shown that most measured grid cells were located in layer II of the mEC. Thus, I first characterized electrophysiological properties of mEC layer II cells. These findings were then combined with additional post-hoc immunohistochemical stainings of some recorded cells and finally classified by a quantitative k-means clustering. The majority of recorded cells displayed the characteristic stellate cell (C1) sag responses, resonances in the theta range (5-10 Hz) and very short latencies to the first spike at rheobase. I also measured typical pyramidal cells (C4) with smaller or no sag and resonance responses, higher input resistances and longer latencies. Two other clusters were assigned: an intermediate stellate cell type (C2) due to their stellate-like responses except for very long latencies to the first action potential, and interneurons (C3) due to their high input resistances coupled with very small capacitances. Post-hoc labeling of recorded neurons revealed double labeled cells which indicates that the used serotypes (Reelin and Calbindin) can not be applied to specifically stain SCs and PCs. This suggests the existence of an additional heterogeneous population.

The majority of recorded mEC layer II cells also showed a prominent depolarizing afterpotential (DAP) within 2 - 7 milliseconds after an action potential. DAPs are state dependent and could be influenced by a pre-hyperpolarization of the membrane before eliciting the AP. This finding led me to apply TTX or different calcium channel blockers to find out which intrinsic factors are involved in the DAP. Indeed, initial results suggested calcium and sodium channels mediate the DAP. However, these findings were controverted by control recordings which measured the responses to the same protocols after

30 minutes without any pharmacological application. These control recordings complicated the interpretation of all pharmacological experiments.

To elucidate the functional impact of the DAP, its influence on the facilitation of action potential generation was assayed by a paired pulse paradigm. The intensity of the first current pulse was chosen to elicit an action potential, whereas the intensity of the second pulse was varied so as to shift responses from sub- to supra-threshold. Larger DAPs generate a broader window of opportunity for spikes, which correlates with facilitated spiking and enhanced responses.

In the last experimental approach we partially mimicked the in-vivo firing response to test whether the membrane oscillations that occur during a grid-field passage are well suited to enhance firing probability in a burst like fashion. Although an enhancement cannot be confirmed by our results, it seems that a stimulation frequency within the theta range facilitates doublets in a broader range within the fast oscillation.

4.2 CLASSIFICATION OF MEC CELLS

In vitro recordings of mEC layer II principal cells of mature rats and gerbils have exhibited characteristics like sag responses, membrane resonance, input resistance and capacitance shown previously in rats and mice (Alonso and Klink, 1993; Klink and Alonso, 1997; Linden and Lopes da Silva, 1998; Erchova et al., 2004; Nolan, Malleret et al., 2004; Canto and Witter, 2012). The capacitance, input resistance and tau were significantly different between gerbils and rats. Mature rats are nearly double the size of a mature gerbil, resulting in bigger neurons with a higher capacitance and a lower input resistance/fast membrane time constant, which leads to faster APs in rats (rat R_{in} < gerbil R_{in}, rat Cap. > gerbil Cap., rat tau < gerbil tau) (Herculano-Houzel et al., 2015).

Stellate cells, which are the primary cellular constitutes of this layer II should have a pronounced sag and a distinct resonance frequency, whereas pyramidal cells have no sag or RF according to Alonso and Klink (1993). In contrast, Linden and Lopes da Silva (1998) showed that all layer II cells produce sags, which matches better to our results and those of Canto and Witter (2012) confirming that each cell class is subject to some variability. According to Richter et al. (1997), the current density of I_h, the inward rectifier current, which is responsible for sag and resonance, is significantly increased in adult rats (> P28) compared to juvenile rats (P8 – P14). They also found that the I_h current density was larger in stellate cells than in layer IV pyramidal cells.

These results could explain the variance within the sag data, where cells were recorded from animals between P30 - P45. Although the animals were all adult, we cannot exclude that an increase still occurred within these 15 days (Dickson, Magistretti, M. H. Shalinsky et al., 2000; Nolan, Dudman et al., 2007; Pastoll et al., 2012).

To answer how to cluster measured cells, we additionally used immunohistochemically antibodies against Reelin (for SC) and Calbindin (for PC) to label recorded neurons posthoc (Varga et al., 2010; Kitamura et al., 2014; Ray, Naumann et al., 2014; Burgalossi and Brecht, 2014). These experiments were complicated by the recording time necessary to allow diffusion of the intracellular solution from the pipette into the cell. Furthermore, a good reseal was required to ensure the cell could still be detected. Another problem by which some labeled cells could have been lost is the treatment of the slice with the detergents to permeabilize the cell membrane for the immunohistochemical procedure. Further tests with the fixation and the incubation times could also improve the posthoc labeling in the future. However, these stainings worked quite well and were comparable with standard procedure stainings. Together with the presence of double labeled cells, these experiments revealed that mEC layer II has a physiologically and immunohistochemically more heterogeneous character than previously described, which made it difficult to cluster into different cell types.

Using a heuristic k-means cluster analysis based on these properties (R_{in}, ISI1/ISI2, Q-value, resonance frequency, AP width, latency to the first action potential, membrane time constant tau) suggested four clusters. The first latency at rheobase was identified as best separator, as indicated by Fuchs et al. (2016), who also used the ISI1/ISI2 ratio as well as the DAP amplitude and the presence of an apical dendrite (Justus et al., 2017). By this clustering method the number of initial parameters was decreased from 18 to 7, reducing the dimensions and making the calculation faster.

Our clustering revealed an interneuron group (C3) within our four clusters. This group had a high input resistance, a fast membrane time constant, no resonance and a fast spiking pattern. Given these results, we classified principal neurons into three classes, namely stellate cells (C1), pyramidal cells (C4) and an intermediate class (C2) (Lee et al., 2010; Buetfering et al., 2014; Martínez et al., 2017). The conclusion that stellate cells constitute cluster C1 is based on the pronounced sag potential, the short latency and the burst firing at the beginning of the stimulation (Alonso and Klink, 1993; Dickson, Magistretti, M. H. Shalinsky et al., 2000; Canto and Witter, 2012; Yoshida et al., 2012; Fuchs et al., 2016). We assigned cluster C4 to pyramidal cells due

to small resonance frequencies, less pronounced sags, late spiking responses at rheobase and a higher input resistances (fewer dendrites) (Alonso and Klink, 1993; Linden and Lopes da Silva, 1998; Canto and Witter, 2012; Alessi et al., 2016; Fuchs et al., 2016). The intermediate class of cluster C2 shows more overlap with stellate cells than with pyramidal cells, the main difference being a significantly longer latency (318.6 ms $\pm$ 93.63 ms) to the first spike compared to the latency of cluster C1. This result is similar to Fuchs et al. (2016) who observed a latency of 350.95 ms $\pm$ 32.55 ms classifying this cell type as intermediate stellate cells.

A disadvantage of k-means clustering compared to hierarchical clustering is that the number of clusters has to be set before, potentially yielding poor results. This method therefore requires multiple trials starting with random initial conditions. We additionally calculated the silhouette and similarity score to choose the optimal cluster number. A comparison of the results from k-means clustering with those obtained with hierarchical clustering revealed that the largest cluster found by either method is highly similar (> 88% shared cells) whereas that is not the case for the other three clusters (see Tab. 3.15). This finding underscores that both cluster methods can yield diverging results and have to be interpreted with a grain of salt. Another approach could be to do first the Ward clustering on the data and then using the centers of the Ward clusters as starting-points for the k-means clustering to compare if k-means can improve on these results. Another improvement of the k-means clustering method would be to include morphological data along with the electrophysiological data for further detailed clustering. The acquisition of morphological data, especially relating to the presence of an apical dendrite, was often inconclusive. Depending on the cutting angle during acute brain slice preparation, the axons and dendrites can be cut during slicing, which could affect the observed tent-like geometry of PCs (Ray, Naumann et al., 2014). In addition, the connections between other mEC layer II neurons can be cut.

We also tried to reproduce the results of Fuchs et al. (2016) and Justus et al. (2017). Justus et al. (2017) could distinguish SCs, PCs and a group of fast-spiking interneurons, whereas Fuchs et al. (2016) found two other principal cell classes, called intermediate stellate and intermediate pyramidal cells. However, the same analysis (Principal component analysis performed by Johannes Nagele) did not reveal more or fewer clusters. Here it should be pointed out that we did not have the additional morphological information about the apical dendrites in the cells. Fuchs et al. (2016) also found co-expression of the two immunohistochemical markers in intermediate stellate and intermediate pyramidal neurons and could separate excitatory neurons

by paired recordings, detecting cell-type-specific excitatory and inhibitory connectivity. Both of these studies were performed in mice at lower temperatures: 30 - 32 °C in Fuchs et al. (2016), and 34 °C in Justus et al. (2017), and with smaller electrode tips (3 - 8 M), which could generate differences with our data (input resistance, membrane resting potential, tau, DAP).

Fuchs et al. (2016) also claimed that one prominent clustering feature was the depolarizing afterpotential, which is absent in their pyramidal neurons. This is in complete contrast to our results, where neurons in each cluster produce depolarizing afterpotentials.

4.3 DAP DEPENDENCE ON DIFFERENT CHANNELS

Depolarizing afterpotentials (DAPs) arose in the majority of measured cells in mEC layer II. They are an intrinsically generated phenomenon, the core of the triphasic postspike dynamics following an AP (Alonso and Klink, 1993; Linden and Lopes da Silva, 1998; Dickson, Magistretti, M. H. Shalinsky et al., 2000; Hönigsperger et al., 2017). The DAP is characterized by a depolarizing deflection of a few millivolts with the maximum occurring 5-6 ms after the AP. DAPs are reported in SCs, pyramidal/pyramidal-like cells as well as in some subgroups of interneurons (somatostatin and neuropeptide Y non-NGF positive cells) in the mEC layer II (Alonso and Klink, 1993; Alessi et al., 2016; Ferrante, Tahvildari et al., 2017). Alessi et al. (2016) also stated that DAPs observed in pyramidal-like neurons were significantly smaller in amplitude at membrane resting potential than in SCs. Furthermore, we could replicate their results and results from Alonso and Klink (1993), showing that the DAP in SCs increased in amplitude upon pre-stimulation with large negative currents. This suggested a high correlation between the cell's membrane voltage and the channels which are involved during resting (Zhang et al., 1993).

4.3.1 *Calcium channels*

The presence of calcium channels in the principal neurons of layer II in the rat entorhinal cortex has already been investigated. Interestingly, high-voltage activated (HVA) calcium currents were expressed with different densities in SCs and PCs, in contrast to low-voltage activated (LVA) calcium currents which did not differ in current density between SCs and PCs (Bruehl and Wadman, 1999; Castelli and Magistretti, 2006). Alessi et al. (2016) performed similar experiments to us. Testing the influence of different calcium

channel blockers, a non-selective (Cadmium), a low-voltage activated channel (NNC) and a high-voltage activated channel blocker (Nifedipine), revealed a significant influence similar to one of the two mechanisms Alessi et al. (2016) found for DAP generation. Hyperpolarized SCs seem to produce calcium-dependent DAPs, whereas SCs and PCs close to threshold elicit sodium-dependent DAPs (Alessi et al., 2016). Alessi et al. (2016) tested the calcium dependence of the DAP, first by exposing the cells to low extracellular calcium concentrations (0.5 mM) and second, by also applying NNC (20 μM) with the membrane potential set at - 82 mV. Both interventions led to a disappearance or decrease of the DAP complex in SCs. Interestingly, the combination of the same concentration of NNC with a lower holding potential of - 87 mV led to unstable effects on the DAP, which suggests a voltage- and state-dependency of the channels. However, the application of mibefradil (10 μM) and Nickel (50 μM), both of which affect low-voltage activated calcium channels, did not result in prominent effects on the DAP, indicating the involvement of $Ca_v3.1$ subunits, which are less sensitive to Nickel. These results are not surprising, given that many studies, mainly performed in hippocampus, state the impact of R- and T-type calcium currents on the DAP complex (Zhang et al., 1993; Visan et al., 2002; Metz, Jarsky et al., 2005; Magee and Carruth, 1999).

4.3.2 *Sodium channels*

Our results confirm the finding of Alessi et al. (2016) that DAPs also depend on sodium channels near threshold in SCs and PCs. In their original experiment, the application of 30 nM TTX significantly affected the DAP in SCs and PCs, similar to our results. In a second experiment, they completely blocked the sodium-channels with 1 μM TTX and injected a special current ramp to generate a reconstructed AP. In this case, DAPs could not be reproduced in either cell type when elicited from the resting membrane potential. However, when elicited from more negative potentials, a calcium-driven DAP could be elicited in SCs. These experiments demonstrate the influence of voltage activated sodium channels in both cell types.

4.3.3 *HCN channels (I_h)*

We additionally tested the effect of the I_h current on the DAP complex, especially based on the fact that DAPs evoked from more negative membrane potentials were larger. I_h is crucial for the generation of subthreshold oscillations, resonance frequencies, sag and also contributes to the resting mem-

brane potential (Dickson, Magistretti, M. H. Shalinsky et al., 2000; Hu et al., 2002; Erchova et al., 2004; Nolan, Dudman et al., 2007; Lüthi and McCormick, 1998). Due to the significant reduction of the DAP amplitude upon blocking low-voltage activated calcium channels, and due to this experimental condition I_h would not be able to produce a depolarizing deflection. However, we were surprised that our data also revealed a significant decrease in the DAP deflection by blocking I_h. Dickson, Magistretti, M. H. Shalinsky et al. (2000) have shown that blocking I_h with ZD reduces the mAHP, which is only slightly affected by calcium channel blockers (Alonso and Llinás, 1989). Furthermore, second messengers such as cyclic AMP are responsible for the voltage-dependence of I_h activation (DiFrancesco and Tromba, 1988). Binding of cyclic AMP to an intracellular domain on HCN leads to activation at less negative voltages and a facilitation of I_h channel opening. Therefore blocking I_h should have similar effects to a rundown or washout.

4.3.4 *Potassium channels*

The effects of potassium (K^+) currents on DAP generation are also of interest. Potassium currents are also important for the development of an AP and were also found to influence the DAP and control burst generation in the hippocampus (Dendritic D-type K^+ currents, KCNQ/M-current) (Metz, Spruston et al., 2007; Yue and Yaari, 2004). KCNQ channel subunits are widely distributed in neurons and are also expressed in the mEC. Activation of this channel promotes depolarization and influences bursting activity (Magistretti et al., 2004). Eder, Ficker et al. (1991) reported three different types of K^+ currents in SCs of the EC: an A-current (fast transient), a delayed rectifier current (either KCNQ/M-current/Kv7) and a calcium activated K^+ current (Nigro et al., 2014; Magistretti et al., 2004; Khawaja et al., 2007). They also found an A-current in PCs and a sustained outward current in both cell types with different current densities, which could be another possible explanation for DAP differences (Eder and Heinemann, 1994). Hönigsperger et al. (2017) showed in their experiments that the application of GTx, which inhibits a delayed rectifier K^+ current activating beyond -30 mV, enhanced the DAP in SCs. They concluded that the Kv2 channels of SCs play an important role in the information production of spatial representation. These findings suggest that investigating the influence of K^+ currents on the DAP generation might reveal intrinsic mechanisms for controlling bursts.

4.3.5 *Washout*

In addition, a rapid, irreversible washout of high-voltage-gated calcium channels is known to occur after 10 - 20 minutes (Fenwick et al., 1982; Pastoll et al., 2012). This phenomenon could be another possible explanation for the decrease in the DAP amplitude, which was observed during all pharmacological and washout experiments. To avoid or slow down the washout problem, we added Mg^{2+}-ATP to the internal solution. The addition of cyclic AMP could potentially delay the washout even more. While we limited the impact of washout by minimising the number of protocols to test, washing the blockers in the bath required at least 3.5 minutes. An alternative procedure would be to puff the channel blockers on the recording site. However, while this method would be faster, it would also be less controllable. The pressure applied for puffing can weaken or disrupt the seal. Moreover the true drug concentration on the recording site is also not exactly known. A second alternative would be to do perforated patch with a recording pipette containing small amounts of an antibiotic agent, such as gramicidin, which can diffuse in the lipid bilayer and make small pores in the cell membrane. These pores provide electrical access to the inside of the cell. The disadvantage of this method is a higher access resistance, which can have a negative effect on the signal-to-noise ratio. Moreover, the diffusion of the antibiotics to perforate the membrane takes some time (~15 min).

4.4 FUNCTIONAL IMPACT OF THE DAP

The transient membrane depolarization of the DAP at which the cell's membrane potential is closer to threshold than under baseline conditions the DAP could possibly facilitate firing of a second that quickly follows the first AP. Indeed, the modulation and the paired pulse stimulation showed that preceding membrane hyperpolarization led to larger DAPs and to a decrease in the current threshold, similar to Linden and Lopes da Silva (1998). Higher excitability due to larger DAPs was highly correlated with an increase in the window of opportunity for a second AP. We never observed a DAP following the second AP. Therefore, the DAP mechanism is suited to support the generation of doublets, but not of bursts with more than two spikes (Linden and Lopes da Silva, 1998; Storm, 1987; Yue and Yaari, 2004). These results are consistent with results from Alessi et al. (2016), who performed similar experiments with a short square pulse stimulation of 1 ms. A square pulse is not representative of a natural/physiological stimulus, we used a 2 ms ramp (0.8 ms rising phase and 1.2 ms descending phase), which better mimics the

time course of synaptic input. Another important difference to Alessi et al. (2016) was the recording temperature. Their recordings were performed at room temperature (21 - 22 °C) whereas we measured at physiological temperature (36 ± 1 °C). This difference in methodology may explain the substantial difference in the input resistance they measured and I measured (see (Alessi et al., 2016) supporting information Fig.1). Alessi et al. (2016) measured a mean input resistance in SCs of 135 MΩ while we measured a mean input resistance of 62 MΩ. The input resistance has been shown to correlate negatively with temperature (Thompson et al., 1985; Griffin and Boulant, 1995). Due to a voltage-independency and an increase in the calcium influx at lower temperatures, Thompson et al. (1985) suggested the contribution of Ca^{2+}-activated K^{+} channels in this temperature phenomenon. They concluded that temperature can elicit a significant changes in intrinsic (DAP) and synaptic cell physiology, which should be considered in slice experiments.

We could show that the DAP facilitates the generation of a second spike, leading to a doublet or burst which, in turn, could trigger a massive release of neurotransmitter at downstream synapses. This transmitter release plays an important role in the improvement of transmission reliability and therefore in the information transfer between neurons in synaptic plasticity (Lisman, 1997; Izhikevich et al., 2003). Compared to single spikes, it has been shown that for burst, the signal-to-noise ratio can be optimized and the information about the stimulus increased (Sherman, 2001; Reinagel et al., 1999).

4.5 CONNECTING IN VIVO WITH IN VITRO WITH SINUSOIDAL INPUTS

By investigating neuronal responses to sinusoidal stimuli, we aimed to connect in vivo data (Domnisoru et al., 2013; Schmidt-Hieber and Häusser, 2013) with in vitro data. Our aim was to test whether the interplay between the DAP, membrane oscillations and a slow depolarizing ramp that occur when an animal passes a grid-field, can enhance the firing probability during grid field passage. A previous in vivo study (Latuske et al., 2015) showed under similar conditions that ~25% of all ISIs were short ISIs (see Fig. 1.13 A and B). In contrast, only a small amount (2.2%) of short ISIs (<10 ms) was elicited during our sinusoidal stimulations in vitro. Even more surprising is the fact that no short ISIs were found when the depolarizing ramp was slow to rise and fall. It is possible that the current intensity was not sufficient to produce more doublets. Monitoring or online-analysis during the recording

should be improved for future experiments to check the ISIs, and modulate stimulus magnitudes accordingly.

We examined the ISI distribution within the fast and the slow sinusoidal oscillations (Fso and Sso). For the Fso, we took into account results from Buzsáki and Draguhn (2004) and Fernandez, Malerba et al. (2013). Buzsáki and Draguhn (2004) claimed that neurons can specifically select their inputs via their intrinsic resonating/ oscillating properties. However, using dynamic clamp, Fernandez, Malerba et al. (2013) showed that SCs in the mEC strongly phase-lock to theta inputs when stimulated with sinusoidal inputs. Additionally, they indicated that background membrane voltage fluctuations regulate the absolute magnitude of phase-locking. Furthermore, the I_h current is crucial in setting the spike phase-locking (Fernandez, Malerba et al., 2013). This is in accordance with the role of I_h in the generation of the resonance frequency, which again is within the theta range in SCs (Haas et al., 2007; Nolan, Dudman et al., 2007). We could not confirm differences in the strength of phase-locking across different time courses for the slow ramp and the fast oscillation, given the relatively small sample sizes. Proceeding from the assumption that the I_h current generates the resonance frequency, we predicted a higher spiking rate and more doublets stimulated within the theta frequency range (Erchova et al., 2004; Schreiber et al., 2004). This would also fit to a computational modeling study by Hasselmo (2013), which suggested a control of the I_h current dynamics in the period of traveling waves within an inhibitory network. These waves could affect the grid cell generation and the detected I_h gradient along the dorsal to ventral axis. This could have an impact on the size and spacing between grid cell firing fields (Hasselmo, 2013; Giocomo and Hasselmo, 2008; Giocomo and Hasselmo, 2009; Garden et al., 2008). This described gradient could also be a reason for the different responses between cells.
Within this context, Higgs and Spain (2009) investigated PCs in neocortical layer 2 - 3. They looked at how two-spike bursts could have been triggered by three different stimuli: noise, step onsets and sine waves in two frequency bands (7 – 16 Hz and 250 – 450 Hz). In these two frequency ranges, bursting enhanced the cell's intrinsic resonances. The two-spike bursts are similar to our elicited doublets. The lack of a third or of subsequent spikes could result from the absence of the DAP on the second spike. Interestingly, they also tested the impact of the DAP in a single-compartment leaky integrate-and-fire model, confirming that the DAP is crucial for short ISIs.

Responses of neurons between clusters to sinusoidal stimuli did not conform to our expectations. Based on the prominent sag, resonance, short latency and DAP responses in SCs (C1) combined with the pre-hyperpolarization

which facilitates spiking, we expected this cell type to fire more during the rising/peak part of the Fso and Sso, similar to the results. This contrasts with to the results of Domnisoru et al. (2013) who showed a symmetrical distribution within the ramp which can not be explained by our data.
Still, regarding the Fso, Domnisoru et al. (2013) showed much higher firing rate at the peaks of the cycle (at which the cells were more depolarized and closer to threshold) than during the troughs similar to our results. Theta oscillations with a higher amplitude elicited spikes with a more precisely defined timing (Domnisoru et al., 2013).
In contrast, PCs (C4) elicit smaller or no sags, have low-pass filter properties and produce smaller DAPs. As a result of these characteristics, we would have expected these cells to fire at the peak, mostly driven by the current and the DAP, in contrast to our results. We expected the third discovered cell type (C2), which responds like a SC apart from the short latency, to fire similarly to SCs. Additionally, one could have expected rebound spikes as a result of their pronounced sag responses. These rebound spikes are a mechanism suggested to mediate or generate grid cell firing (Bonilla-Quintana et al., 2017; Ferrante, Shay et al., 2017). But at least one of the two measured cells responded more similarly to an interneuron. For measured interneurons, the results did not conform to our expectations. Given their fast spiking property they were assumed to fire everywhere within the stimuli driven by the current. These results show that the clustering is still imperfect.

Rather than using a subjective clustering by eye, I decided to use the objective hierarchical k-means clustering, which was separated based on the latency of the first spike at rheobase, resonance frequency and sag. Interestingly, the clustering done by eye revealed a nicer separation of the cells and matched our expectation: clustered SCs fired more at the beginning of the Sso in the increasing phase and also during the Fso, whereas PCs fired more around the peaks. Based on these results, the cluster analysis should be further improved.

Previous in vivo recordings of grid cells, border cells and head-direction cells in mice by Latuske et al. (2015) have shown two groups of neurons in the superficial layers of the mEC: a "bursty" and a "non-bursty" group . They observed more grid cell periodicity in bursty neurons, whereas non-bursty neurons were more selective for head-direction or border cells. Interestingly, bursty neurons spiked at an earlier phase during theta oscillation than non-bursty neurons. If we assume that bursty cells are SCs and non-bursty cells are PCs this could be comparable to our Sso results simulating a slow depolarizing ramp and where we expected SCs to fire earlier. Another interesting observation which ran completely against our expectations was that both

cell groups fire preferentially at the same phase of a theta cycle, close to the end of the decreasing phase. Latuske et al. (2015) conclude two different integration mechanisms in the mEC which encode different spatial signals.

Ebbesen et al. (2016) claim the complete opposite to Latuske et al. (2015). They state that mEC layer II PCs are theta-modulated, have shorter spikes and burst, in contrast to layer II SCs which apparently show no bursting behavior, have longer spikes and are only weakly modulated by theta (Ebbesen et al., 2016; Fernandez, Malerba et al., 2013). This was also observed by Schmidt-Hieber and Häusser (2013) in SCs which did neither burst at resting potential nor in a depolarized state suggesting that in vivo intrinsic oscillations could be dampened by strong synaptic inputs (Fernandez and White, 2008). This suggestion would also fit to Domnisoru et al. (2013) who claim that "ramps, not oscillations, are the primary drive of field formation". Another idea is that a temporal code is formed by the excitatory inputs during fast oscillations ('rate-to-phase transform') (McLelland and Paulsen, 2009).

Given the small number of bursts and to improve the methodology of this experiment, I would suggest that future experiments use dynamic clamp to simulate specifically different inputs or channels. An improvement would be to collect more control traces without the fast stimulation to have a better comparison to the Fso traces.

5

CONCLUSION

Depolarizing afterpotenials were observed in all mEC layer II cell groups, they amplify burst spiking behavior and seem to play an important role in the dynamics of the mEC. We identified some channels that are involved in the DAP phenomenon, but open questions remain. Additional pharmacological experiments are necessary to uncover further aspects, including perforated patch or puff-application which would speed up the recording time and decrease wash-out effects. Optimized and supplementary immunohistochemical stainings would also help to uncover the different cell populations in the layer II of the mEC. Another improvement of the methods would be to use dynamic clamp in combination with calcium and voltage imaging. Combining these different methods would allow us to change different channel dynamics online and image calcium or voltage changes in the dendrites, the soma or in both.

Using dynamic clamp and imaging methods, it would also be interesting to investigate how the network around and within the superficial mEC layers is connected. At present, there are various inconsistencies. In addition, we sought a complete understanding of the mechanisms underlying this prominent activity pattern. By combining these experimental methods with computational modeling we will be able to construct a comprehensive and consistent biophysical mEC layer II cell model.

It is very important to ascertain these questions given the involvement of bursting mechanisms in spatial navigation, synaptic plasticity but also in brain disorders such as epilepsy and Alzheimer's disease (Zhang et al., 1993; Lisman, 1997; O'Keefe and Dostrovsky, 1971; Visan et al., 2002).

LIST OF FIGURES

LIST OF TABLES

LIST OF ABBREVIATIONS

PBS **p**hosphate-**b**uffered **s**aline

PFA **p**ara**f**orm**a**ldehyde

ZAP impedance **a**mplitude **p**rofiles

ACSF **a**rtificial **c**erebro**s**pinal **f**luid

DAP **D**epolarizing **A**fter**P**otential

E_{rest} **rest**ing membrane potential

EC **E**ntorhinal **C**ortex

$f_{resonance}$ **r**esonance **f**requency

fAHP **f**ast **A**fter**H**yper**P**olarisation

Fso **f**ast **s**inusoidal **o**scillation

HF **H**ippocampal **F**ormation

ISI **I**nter-**S**pike-**I**nterval

lEC **l**ateral **E**ntorhinal **C**ortex

mAHP **m**edium-rate **A**fter**H**yper**P**olarization

mEC **m**edial **E**ntorhinal **C**ortex

PC **P**yramidal **c**ell

RF **r**esonance **f**requency

SC **S**tellate **c**ell

Sso **s**low **s**inusoidal **o**scillation

Wfs1 **W**olframin **S**yndrom **1**

Abbasi, S. and S. S. Kumar (2014). 'Regular-spiking cells in the presubiculum are hyperexcitable in a rat model of temporal lobe epilepsy'. In: *Journal of Neurophysiology* 112, pp. 2888–2900.

Alessi, C., A. Raspanti and J. Magistretti (2016). 'Two distinct types of depolarizing afterpotentials are differentially expressed in stellate and pyramidal-like neurons of entorhinal-cortex layer II'. In: *Hippocampus* 26.3, pp. 380–404.

Alonso, A. and R. Klink (1993). 'Differential electroresponsiveness of stellate and pyramidal-like cells of medial entorhinal cortex layer II.' In: *Journal of neurophysiology* 70.1, pp. 128–43.

Alonso, A. and R. Llinás (1989). 'Subthreshold Na+-dependent theta-like rhythmicity in stellate cells of entorhinal cortex layer II'. In: *Nature* 342, pp. 175–177.

Amaral, D. G., C. Dolorfo and P. Alvarez-Royo (1991). 'Organization of CA1 projections to the subiculum: A PHA-L analysis in the rat'. In: *Hippocampus* 1.4, pp. 415–436.

Amaral, D. G., H. E. Scharfman and P. Lavenex (2007). 'The dentate gyrus: fundamental neuroanatomical organization (dentate gyrus for dummies)'. In: *Progress in Brain Research* 163, pp. 3–22.

Ammer, J. J., I. Siveke and F. Felmy (2015). 'Activity-Dependent Transmission and Integration Control the Timescales of Auditory Processing at an Inhibitory Synapse'. In: *Current Biology* 25.12, pp. 1562–1572.

Andersen, P., T. W. Blackstad and T. Lömö (1966). 'Location and Identification of Excitatory Synapses on Hippocampal Pyramidal Cells'. In: *Experimental brain research* 1, pp. 236–248.

Andersen, P., R. Morris, D. Amaral, T. Bliss and J. O' Keefe (2009). *The Hippocampus Book*, pp. 1–852. arXiv: arXiv:1011.1669v3.

Armstrong, C., J. Wang, S. Y. Lee, J. Broderick, M. J. Bezaire, S.-H. Lee and I. Soltesz (2016). 'Target-Selectivity of Parvalbumin-Positive Interneurons in Layer II of Medial Entorhinal Cortex in Normal and Epileptic Animals'. In: *Hippocampus* 26.6, pp. 48–56.

Azouz, R., M. S. Jensen and Y. Yaari (1996). 'Ionic basis of spike after-depolarization and burst generation in adult rat hippocampal CAl pyramidal cells'. In: *Journal of Physiology* 1996.492.1, pp. 211–223.

Barry, C., C. Lever, R. Hayman, T. Hartley, S. Burton, J. O'Keefe, K. Jeffery and N. Burgess (2006). 'The Boundary Vector Cell Model of Place Cell Firing and Spatial Memory'. In: *Reviews in the Neurosciences* 17.1-2, pp. 71–97.

Beed, P., M. H. K. Bendels, H. F. Wiegand, C. Leibold, F. W. Johenning and D. Schmitz (2010). 'Analysis of excitatory microcircuitry in the medial entorhinal cortex reveals cell-type-specific differences.' In: *Neuron* 68.6, pp. 1059–66.

Bliss, T. V. P. and L. T (1973). 'Long-lasting potentiation of synaptic transmission in the dentate area of the unanaesthetized rabbit following stimulation of the perforant path.' In: *The Journal of Physiology* 232.2, pp. 357–374.

Boccara, C. N., F. Sargolini, V. H. Thoresen, T. Solstad, M. P. Witter, E. I. Moser and M.-B. Moser (2010). 'Grid cells in pre- and parasubiculum.' In: *Nature Neuroscience* 13.8, pp. 987–94.

Bonilla-Quintana, M., K. C. Wedgwood, R. D. O'Dea and S. Coombes (2017). 'An Analysis of Waves Underlying Grid Cell Firing in the Medial Enthorinal Cortex'. In: *Journal of Mathematical Neuroscience* 7.1.

BoSmith, R. E., I. Briggs and N. C. Sturgess (1993). 'Inhibitory actions of ZENECA ZD7288 on whole-cell hyperpolarization activated inward current (If) in guinea-pig dissociated sinoatrial node cells'. In: *British Journal of Pharmacology* 110.1, pp. 343–349.

Brodmann, K. (1909). *Vergleichende Lokalisationlehre der Grosshirnrinde in inren Prinzipien dargestellt auf Grund des Zellenbaues*. Leipzig: Barth, p. 324.

Bruehl, C. and W. J. Wadman (1999). 'Calcium currents in acutely isolated stellate and pyramidal neurons of rat entorhinal cortex'. In: *Brain Research* 816.2, pp. 554–562.

Brun, V. H., T. Solstad, K. B. Kjelstrup, M. Fyhn, M. P. Witter, E. I. Moser and M.-B. Moser (2008). 'Progressive increase in grid scale from dorsal to ventral medial entorhinal cortex.' In: *Hippocampus* 18.12, pp. 1200–12.

Buetfering, C., K. Allen and H. Monyer (2014). 'Parvalbumin interneurons provide grid cell-driven recurrent inhibition in the medial entorhinal cortex.' In: *Nature Neuroscience* 17.5, pp. 710–8.

Burgalossi, A. and M. Brecht (2014). 'Cellular, columnar and modular organization of spatial representations in medial entorhinal cortex'. In: *Current Opinion in Neurobiology* 24, pp. 47–54.

Burgalossi, A., L. Herfst, M. von Heimendahl, H. Förste, K. Haskic, M. Schmidt and M. Brecht (2011). 'Microcircuits of functionally identified neurons in the rat medial entorhinal cortex.' In: *Neuron* 70.4, pp. 773–86.

Burgess, N., A. Jackson, T. Hartley and J. O'Keefe (2000). 'Predictions derived from modelling the hippocampal role in navigation'. In: *Biological Cybernetics* 83.3, pp. 301–312.

Burgess, N. and J. O'Keefe (1996). 'Neuronal computations underlying the ring of place cells and their role in navigation'. In: *Hippocampus* 762.1996, pp. 749–762.

Buzsáki, G. and A. Draguhn (2004). 'Neuronal oscillations in cortical networks'. In: *Science* 304.5679, pp. 1926–1929.

Caballero-Bleda, M., M. Leda and M. P. Witter (1993). 'Regional and Laminar Organization of Projections From the Presubiculum and Parasubiculum to the Entorhinal Cortex : An Anterograde Tracing Study in the Rat'. In: *Journal of Comparative Neurology* 129, pp. 115–129.

Canto, C. B., F. G. Wouterlood and M. P. Witter (2008). 'What does the anatomical organization of the entorhinal cortex tell us?' In: *Neural Plasticity* 2008, pp. 1–18.

Canto, C. B. and M. P. Witter (2012). 'Cellular properties of principal neurons in the rat entorhinal cortex. II. The medial entorhinal cortex.' In: *Hippocampus* 22.6, pp. 1277–99.

Castelli, L. and J. Magistretti (2006). 'High-voltage-activated Ca2+ currents show similar patterns of expression in stellate and pyramidal cells from rat entorhinal cortex layer II'. In: *Brain Research* 1090.1, pp. 76–88.

Commins, S., J. P. Aggleton and S. M. O'Mara (2002). 'Physiological evidence for a possible projection from dorsal subiculum to hippocampal area CA1'. In: *Experimental Brain Research* 146, pp. 155–160.

Couey, J. J. et al. (2013). 'Recurrent inhibitory circuitry as a mechanism for grid formation.' In: *Nature Neuroscience* January, pp. 1–9.

Dickson, C. T., J. Magistretti, M. H. Shalinsky, E. Fransén, M. E. Hasselmo and A. Alonso (2000). 'Properties and role of I(h) in the pacing of subthreshold oscillations in entorhinal cortex layer II neurons.' In: *Journal of Neurophysiology* 83.5, pp. 2562–79.

Dickson, C. T., a. R. Mena and A. Alonso (1997). 'Electroresponsiveness of medial entorhinal cortex layer III neurons in vitro.' In: *Neuroscience* 81.4, pp. 937–50.

Dickson, C. T., J. Magistretti, M. Shalinsky, B. Hamam and A. Alonso (2006). 'Oscillatory Activity in Entorhinal Neurons and Circuits: Mechanisms and Function'. In: *Annals of the New York Academy of Sciences* 911.1, pp. 127–150.

DiFrancesco, D. and C. Tromba (1988). 'Muscarinic control of the hyperpolarization-activated current in rabbit sino-atrial node myocytes.' In: *The Journal of Physiology* 405.1, pp. 493–510.

Ding, S. L. (2013). 'Comparative anatomy of the prosubiculum, subiculum, presubiculum, postsubiculum, and parasubiculum in human, monkey, and rodent'. In: *Journal of Comparative Neurology* 521.18, pp. 4145–4162.

Doiron, B., A.-M. M. Oswald and L. Maler (2007). 'Interval Coding . II. Dendrite-Dependent Mechanisms'. In: *Journal of Neurophysiology*, pp. 2744–2757.

Doller, H. J. and F. F. Weight (1982). 'Perforant pathway activation of hippocampal CA1 stratum pyramidale neurons: Electrophysiological evidence for a direct pathway'. In: *Brain Research* 237.1, pp. 1–13.

Domnisoru, C., A. A. Kinkhabwala and D. W. Tank (2013). 'Membrane potential dynamics of grid cells.' In: *Nature* 495.7440, pp. 199–204.

Ebbesen, C. L., E. T. Reifenstein, Q. Tang, A. Burgalossi, S. Ray, S. Schreiber, R. Kempter and M. Brecht (2016). 'Cell Type-Specific Differences in Spike Timing and Spike Shape in the Rat Parasubiculum and Superficial Medial Entorhinal Cortex'. In: *Cell Reports* 16.4, pp. 1005–1015.

Eder, C., E. Ficker, J. Gündel and U. Heinemann (1991). 'Outward Currents in Rat Entorhinal Cortex Stellate Cells Studied with Conventional and Perforated Patch Recordings.' In: *The European Journal of Neuroscience* 3.July, pp. 1271–1280.

Eder, C. and U. Heinemann (1994). 'Current density analysis of outward currents in acutely isolated rat entorhinal cortex cells'. In: *Neuroscience Letters* 174.1, pp. 58–60.

Erchova, I., G. Kreck, U. Heinemann and A. V. M. Herz (2004). 'Dynamics of rat entorhinal cortex layer II and III cells: characteristics of membrane potential resonance at rest predict oscillation properties near threshold.' In: *The Journal of Physiology* 560.1, pp. 89–110.

Fenwick, E. M., A. Martyt and E. Nehert (1982). 'Sodium and Calcium Channels in Bovine Chromaffin Cells'. In: *Journal of Neurophysiology* 331, pp. 599–635.

Fernandez, F. R. (2005). 'Dendritic Na+ Current Inactivation Can Increase Cell Excitability By Delaying a Somatic Depolarizing Afterpotential'. In: *Journal of Neurophysiology* 94.6, pp. 3836–3848.

Fernandez, F. R., P. Malerba, P. C. Bressloff and J. A. White (2013). 'Entorhinal Stellate Cells Show Preferred Spike Phase-Locking to Theta Inputs That Is Enhanced by Correlations in Synaptic Activity'. In: *Journal of Neuroscience* 33.14, pp. 6027–6040.

Fernandez, F. R. and J. A. White (2008). 'Artificial synaptic conductances reduce subthreshold oscillations and periodic firing in stellate cells of the entorhinal cortex.' In: *The Journal of Neuroscience* 28.14, pp. 3790–803.

Ferrante, M., C. F. Shay, Y. Tsuno, G. William Chapman and M. E. Hasselmo (2017). 'Post-Inhibitory rebound spikes in rat medial entorhinal layer II/III principal cells: In Vivo, In Vitro, and computational modeling characterization'. In: *Cerebral cortex* 27.3, pp. 2111–2125.

Ferrante, M., B. Tahvildari, A. Duque, M. Hadzipasic, D. Salkoff, E. W. Zagha, M. E. Hasselmo and D. A. McCormick (2017). 'Distinct Functional Groups Emerge from the Intrinsic Properties of Molecularly Identified Entorhinal Interneurons and Principal Cells'. In: *Cerebral Cortex* 27.6, pp. 3186–3207.

Finch, D. M., E. E. Wong, E. L. Derian and T. L. Babb (1986). 'Neurophysiology of limbic system pathways in the rat: Projections from the subicular complex and hippocampus to the entorhinal cortex'. In: *Brain Research* 397.2, pp. 205–213.

Foster, T. C., C. A. Castro and B. L. McNaughton (1989). 'Spatial selectivity of rat hippocampal neurons: dependence on preparedness for movement.' In: *Science* 244, pp. 1580–1582.

Fuchs, E. C. et al. (2016). 'Local and Distant Input Controlling Excitation in Layer II of the Medial Entorhinal Cortex'. In: *Neuron* 89.1, pp. 194–208.

Funahashi, M. and M. Stewart (1997). 'Presubicular and parasubicular cortical neurons of the rat: Functional separation of deep and superficial neurons in vitro'. In: *Journal of Physiology* 501.2, pp. 387–403.

Fyhn, M., T. Hafting, A. Treves, M.-B. Moser and E. I. Moser (2007). 'Hippocampal remapping and grid realignment in entorhinal cortex.' In: *Nature* 446.7132, pp. 190–4.

Fyhn, M., S. Molden, M. P. Witter, E. I. Moser and M.-B. Moser (2004). 'Spatial representation in the entorhinal cortex.' In: *Science* 305.5688, pp. 1258–64.

Garden, D. L. F., P. D. Dodson, C. O'Donnell, M. D. White and M. F. Nolan (2008). 'Tuning of synaptic integration in the medial entorhinal cortex to the organization of grid cell firing fields.' In: *Neuron* 60.5, pp. 875–89.

Germroth, P., W. K. Schwerdtfeger and E. H. Buhl (1989). 'Morphology of identified entorhinal neurons projecting to the hippocampus. A light microscopical study combining retrograde tracing and intracellular injection'. In: *Neuroscience* 30.3, pp. 683–691.

Giocomo, L. M. and M. E. Hasselmo (2007). 'Neuromodulation by glutamate and acetylcholine can change circuit dynamics by regulating the relative influence of afferent input and excitatory feedback'. In: *Molecular Neurobiology* 36, pp. 184–200.

Giocomo, L. M. and M. E. Hasselmo (2008). 'Time constants of h current in layer ii stellate cells differ along the dorsal to ventral axis of medial entorhinal cortex.' In: *The Journal of Neuroscience* 28.38, pp. 9414–25.

Giocomo, L. M. and M. E. Hasselmo (2009). 'Knock-out of HCN1 subunit flattens dorsal-ventral frequency gradient of medial entorhinal neurons in adult mice.' In: *The Journal of Neuroscience* 29.23, pp. 7625–7630.

Griffin, J. D. and J. A. Boulant (1995). 'Temperature effects on membrane potential and input resistance in rat hypothalamic neurones.' In: *The Journal of Physiology* 488.2, pp. 407–418.

Groen, T. van and J. M. Wyss (1990). 'The connections of presubiculum and parasubiculum in the rat'. In: *Brain Research* 518.1-2, pp. 227–243.

Haas, J. S., A. D. Dorval and J. a. White (2007). 'Contributions of Ih to feature selectivity in layer II stellate cells of the entorhinal cortex.' In: *Journal of Computational Neuroscience* 22.2, pp. 161–71.

Haeften, T. van, F. G. Wouterlood, B. Jorritsma-Byham and M. P. Witter (1997). 'GABAergic presubicular projections to the medial entorhinal cortex of the rat.' In: *The Journal of Neuroscience* 17.2, pp. 862–874.

Hafting, T., M. Fyhn, T. Bonnevie, M.-B. Moser and E. I. Moser (2008). 'Hippocampus-independent phase precession in entorhinal grid cells.' In: *Nature* 453.7199, pp. 1248–52.

Hafting, T., M. Fyhn, S. Molden, M.-B. Moser and E. I. Moser (2005). 'Microstructure of a spatial map in the entorhinal cortex.' In: *Nature* 436.7052, pp. 801–6.

Haj-Dahmane, S. and R. Andrade (1997). 'Calcium-activated cation nonselective current contributes to the fast afterdepolarization in rat prefrontal cortex neurons.' In: *Journal of Neurophysiology* 78.4, pp. 1983–9.

Hamam, B. N., T. E. Kennedy, A. Alonso and D. G. Amaral (2000). 'Morphological and electrophysiological characteristics of layer V neurons of the rat medial entorhinal cortex.' In: *Journal of Comparative Neurology* 418, pp. 457–472.

Harris, K. D., H. Hirase, X. Leinekugel, D. A. Henze and G. Buzsáki (2001). 'Temporal interaction between single spikes and complex spike bursts in hippocampal pyramidal cells.' In: *Neuron* 32.1, pp. 141–9.

Hasselmo, M. E. (2013). 'Neuronal rebound spiking, resonance frequency and theta cycle skipping may contribute to grid cell firing in medial entorhinal cortex'. In: *Philosophical Transactions of the Royal Society B: Biological Sciences* 369.1635, pp. 20120523–20120523.

Hebb, D. O. (1949). *The Organization of Behavior*. New York: Wiley., pp. 1–365.

Heka (2013). 'PATCHMASTER Tutorial 2.73'. In: *Heka Elektronick*, pp. 1–259.

Herculano-Houzel, S., D. J. Messeder, K. Fonseca-Azevedo and N. A. Pantoja (2015). 'When larger brains do not have more neurons: increased numbers of cells are compensated by decreased average cell size across mouse individuals'. In: *Frontiers in Neuroanatomy* 9.64.

Higgs, M. H. and W. J. Spain (2009). 'Behavioral/Systems/Cognitive Conditional Bursting Enhances Resonant Firing in Neocor-

tical Layer 2–3 Pyramidal Neurons'. In: *Journal of Neuroscience* 29, pp. 1285–1299.

Hirase, H., A. Czurkó, J. Csicsvari and G. Buzsáki (1999). 'Firing rate and theta-phase coding by hippocampal pyramidal neurons during 'space clamping''. In: *European Journal of Neuroscience* 11.12, pp. 4373–4380.

Hodgkin, A. L. and A. F. Huxley (1952). 'A quantitative description of membrane current and its application to conduction and excitation in nerve'. In: *Journal of Physiology* 117, pp. 500–544.

Hönigsperger, C., M. J. Nigro and J. F. Storm (2017). 'Physiological roles of Kv2 channels in entorhinal cortex layer II stellate cells revealed by Guangxitoxin-1E'. In: *The Journal of Physiology* 595.3, pp. 739–757.

Hu, H., K. Vervaeke and J. F. Storm (2002). 'Two forms of electrical resonance at theta frequencies, generated by M-current, h-current and persistent Na+ current in rat hippocampal pyramidal cells'. In: *The Journal of Physiology* 545.3, pp. 783–805.

Huang, L., B. M. Keyser, T. M. Tagmose, J. B. Hansen, J. T. Taylor, H. Zhuang, M. Zhang, D. S. Ragsdale and M. Li (2004). 'NNC 55-0396 [(1S,2S)-2-(2-(N-[(3-Benzimidazol-2-yl)propyl]-N- methylamino) -ethyl)-6-fluoro-1,2,3,4-tetrahydro-1-isopropyl-2- naphtyl cyclopropane- carboxylate dihydrochloride]: A New Selective Inhibitor of T-Type Calcium Channels'. In: *Journal of Pharmacology and Experimental Therapeutics* 309.1, pp. 193–199.

Izhikevich, E. M., N. S. Desai, E. C. Walcott and F. C. Hoppensteadt (2003). 'Bursts as a unit of neural information: Selective communication via resonance'. In: *Trends in Neurosciences* 26.3, pp. 161–167.

Justus, D., D. Dalügge, S. Bothe, F. Fuhrmann, C. Hannes, H. Kaneko, ... and S. Remy (2017). 'Glutamatergic synaptic integration of locomotion speed via septoentorhinal projections'. In: *Nature Neuroscience* 20.1, pp. 16–19.

Kandel, E. R. and W. A. Spencer (1961). 'Electrophysiology of hippocampal neurons: II. after-potentials and repetitive firining'. In: *Journal of Neurophysiology* 24.3, pp. 243–259.

Khawaja, F., A. Alonso and C. Bourque (2007). 'Ca2+-dependent K+ currents and spike-frequency adaptation in medial entorhinal cortex layer II stellate cells'. In: *Hippocampus* 1148, pp. 1143–1148.

Kispersky, T., J. a. White and H. G. Rotstein (2010). 'The mechanism of abrupt transition between theta and hyper-excitable spiking activity in medial entorhinal cortex layer II stellate cells.' In: *PloS one* 5.11, e13697.

Kitamura, T., M. Pignatelli, J. Suh, K. Kohara, A. Yoshiki, K. Abe and S. Tonegawa (2014). 'Island Cells Control Temporal Association Memory'. In: *Science* 343.6173, pp. 896–901.

Klink, R. and A. Alonso (1997). 'Morphological characteristics of layer II projection neurons in the rat medial entorhinal cortex.' In: *Hippocampus* 7.5, pp. 571–83.

Koganezawa, N., R. Gisetstad, E. Husby, T. P. Doan and M. P. Witter (2015). 'Excitatory Postrhinal Projections to Principal Cells in the Medial Entorhinal Cortex'. In: *Journal of Neuroscience* 35.48, pp. 15860–15874.

Köhler, C. (1986). 'Intrinsic connections of the retrohippocampal region in the rat brain. II. The medial entorhinal area'. In: *Journal of Comparative Neurology* 246.2, pp. 149–169.

Kramer, R. H. and R. S. Zucker (1985). 'Calcium-dependent inward current in Aplysia bursting pace-maker neurones.' In: *Journal of Physiology* 362, pp. 107–130.

Kropff, E., J. E. Carmichael, M.-B. Moser and E. I. Moser (2015). 'Speed cells in the medial entorhinal cortex'. In: *Nature* 523.7561, pp. 419–424.

Latuske, P., O. Toader and K. Allen (2015). 'Interspike Intervals Reveal Functionally Distinct Cell Populations in the Medial Entorhinal Cortex'. In: *The Journal of Neuroscience* 35.31, pp. 10963–10976.

Lee, S., J. Hjerling-Leffler, E. Zagha, G. Fishell and B. Rudy (2010). 'The Largest Group of Superficial Neocortical GABAergic Interneurons Expresses Ionotropic Serotonin Receptors'. In: *The Journal of Neuroscience* 30.50, pp. 16796–16808.

Leibnitz, G. (1715). *Fifth letter to Samuel Clarke*. Tech. rep.

Lever, C., S. Burton, A. Jeewajee, J. O'Keefe and N. Burgess (2009). 'Boundary Vector Cells in the Subiculum of the Hippocampal Formation'. In: *Journal of Neuroscience* 29.31, pp. 9771–9777.

Levy, W. B. and O. Steward (1983). 'Temporal contiguity requirement for long-term associative potentiation/depression in the hippocampus'. In: *Neuroscience* 8.4, pp. 791–797.

Linden, S. van der and F. H. Lopes da Silva (1998). 'Comparison of the electrophysiology and morphology of layers III and II neurons of the rat medial entorhinal cortex in vitro.' In: *The European Journal of Neuroscience* 10.November 1997, pp. 1479–1489.

Lisman, J. E. (1997). 'Bursts as a unit of neural information: Making unreliable synapses reliable'. In: *Trends in Neurosciences* 20.1, pp. 38–43.

Lorente de Nó, R. (1934). 'Studies on the structure of the cerebral cortex. II. Continuation of the study of the ammonic system.' In: *Journal of Psychology and Neurology* 46, pp. 113–177.

Lüthi, A. and D. A. McCormick (1998). 'H-current: Properties of a neuronal and network pacemaker'. In: *Neuron* 21.1, pp. 9–12.

Ma, L., A. Alonso and C. T. Dickson (2008). 'Differential induction of long-term potentiation in the horizontal versus columnar superficial connections to layer II cells of the entorhinal cortex.' In: *Neural plasticity* 2008, pp. 1–12.

Magee, J. C. and M. Carruth (1999). 'Dendritic voltage-gated ion channels regulate the action potential firing mode of hippocampal CA1 pyramidal neurons.' In: *Journal of Neurophysiology* 82.4, pp. 1895–901.

Magee, J. C. and D. Johnston (1997). 'A Synaptically Controlled, Associative Signal for Synaptic Plasticity in Hippocampal Neurons'. In: *Science* 275.January, pp. 209–213.

Magistretti, J., L. Ma, M. H. Shalinsky, W. Lin, R. Klink and A. Alonso (2004). 'Spike Patterning by Ca2+-Dependent Regulation of a Muscarinic Cation Current in Entorhinal Cortex Layer II Neurons'. In: *Journal of Neurophysiology* 92.3, pp. 1644–1657.

Martínez, J. J., B. Rahsepar and J. A. White (2017). 'Anatomical and Electrophysiological Clustering of Superficial Medial Entorhinal Cortex Interneurons'. In: *Eneuro* 4.5, pp. 1–23.

Massey, P. V. and Z. I. Bashir (2007). 'Long-term depression: multiple forms and implications for brain function'. In: *Trends in Neurosciences* 30.4, pp. 176–184.

McCormick, D. A., B. W. Connors, J. W. Lighthall and D. a. Prince (1985). 'Comparative electrophysiology of pyramidal and sparsely spiny stellate neurons of the neocortex.' In: *Journal of Neurophysiology* 54.4, pp. 782–806.

McLelland, D. and O. Paulsen (2009). 'Neuronal oscillations and the rate-to-phase transform: mechanism, model and mutual information.' In: *The Journal of Physiology* 587.4, pp. 769–85.

McNaughton, B. L., C. A. Barnes and J. O'Keefe (1983). 'The contributions of position, direction, and velocity to single unit activity in the hippocampus of freely-moving rats'. In: *Experimental Brain Research* 52.1, pp. 41–49.

McNaughton, B. L., F. P. Battaglia, O. Jensen, E. I. Moser and M. B. Moser (2006). 'Path integration and the neural basis of the 'cognitive map''. In: *Nature Reviews Neuroscience* 7.8, pp. 663–678.

Mehaffey, W. H. (2005). 'Deterministic Multiplicative Gain Control with Active Dendrites'. In: *Journal of Neuroscience* 25.43, pp. 9968–9977.

Metz, A. E., T. Jarsky, M. Martina and N. Spruston (2005). 'R-type calcium channels contribute to afterdepolarization and bursting in hippocampal CA1 pyramidal neurons.' In: *The Journal of Neuroscience* 25.24, pp. 5763–73.

Metz, A. E., N. Spruston and M. Martina (2007). 'Dendritic D-type potassium currents inhibit the spike afterdepolarization in rat hippocampal CA1 pyramidal neurons.' In: *The Journal of Physiology* 581.Pt 1, pp. 175–87.

Moser, E. I., M.-B. Moser and B. Mcnaughton (2017). 'Spatial representation in the hippocampal formation : a history'. In: *Nature Neuroscience* 20.11, pp. 1448–1464.

Muller, R. U., E. Bostock, J. S. Taube and J. L. Kubie (1994). 'On the directional firing properties of hippocampal place cells.' In: *The Journal of neuroscience : the official journal of the Society for Neuroscience* 14.12, pp. 7235–51.

Muller, R. U. and J. L. Kubie (1987). 'The effects of changes in the environment on the spatial firing of hippocampal complex-spike cells'. In: *Journal of Neuroscience* 7.7, pp. 1951–1968.

Naber, P. A., M. P. Witter and F. H. Lopes Da Silva (1999). 'Perirhinal cortex input to the hippocampus in the rat: Evidence for parallel pathways, both direct and indirect. A combined physiological and anatomical study'. In: *European Journal of Neuroscience* 11.11, pp. 4119–4133.

Naber, P. A., M. Caballero-Bleda, B. Jorritsma-Byham and M. P. Witter (1997). 'Parallel input to the hippocampal memory system through peri- and postrhinal cortices'. In: *NeuroReport* 8.11, pp. 2617–2621.

Naber, P. A., F. H. Lopes Da Silva and M. P. Witter (2001). 'Reciprocal connections between the entorhinal cortex and hippocampal fields CA1 and the subiculum are in register with the projections from CA1 to the subiculum'. In: *Hippocampus* 11.2, pp. 99–104.

Nassar, M., J. Simonnet, R. Lofredi, I. Cohen, E. Savary, Y. Yanagawa, R. Miles and D. Fricker (2015). 'Diversity and overlap of parvalbumin and somatostatin expressing interneurons in mouse presubiculum'. In: *Frontiers in Neural Circuits* 9.May, pp. 1–19.

Nigro, M. J., P. Mateos-Aparicio and J. F. Storm (2014). 'Expression and Functional Roles of Kv7/KCNQ/M-Channels in Rat Medial Entorhinal Cortex Layer II Stellate Cells.' In: *The Journal of Neuroscience* 34.20, pp. 6807–12.

Nolan, M. F., G. Malleret et al. (2004). 'A behavioral role for dendritic integration: HCN1 channels constrain spatial memory and plasticity at inputs to distal dendrites of CA1 pyramidal neurons'. In: *Cell* 119, pp. 719–732.

Nolan, M. F., J. T. Dudman, P. D. Dodson and B. Santoro (2007). 'HCN1 channels control resting and active integrative properties of stel-

late cells from layer II of the entorhinal cortex.' In: *The Journal of Neuroscience* 27.46, pp. 12440–51.

O' Keefe, J. and N. Burgess (1996). *Geometric determinants of the place fields of hippocampal neurons*.

O'Keefe, J. and D. Conway (1978). 'Hippocampal place units in the freely moving rat: Why they fire where they fire'. In: *Experimental Brain Research* 31.4, pp. 573–590.

O'Keefe, J. (1976). 'Place units in the hippocampus of the freely moving rat'. In: *Experimental Neurology* 51.1, pp. 78–109.

O'Keefe, J. and J. Dostrovsky (1971). 'Short Communications The hippocampus as a spatial map: Preliminary evidence from unit activity in the freely moving rat'. In: *Brain Research* 34, pp. 171–175.

O'Keefe, J., M. L. Recce, J.O'Keefe and M. L. Recce (1993). 'Phase relationship between hippocampal place units and the hippocampal theta rhythm'. In: *Hippocampus* 3.3, pp. 317–330.

O'Keefe, J. and A. Speakman (1987). 'Single unit activity in the rat hippocampus during a spatial memory task'. In: *Experimental Brain Research* 86.

O'Mara, S. (2005). 'The subiculum: What it does, what it might do, and what neuroanatomy has yet to tell us'. In: *Journal of Anatomy* 207.3, pp. 271–282.

O'Mara, S. M., S. Commins, M. Anderson and J. Gigg (2001). 'The subiculum: A review of form, physiology and function'. In: *Progress in Neurobiology* 64, pp. 129–155.

Pastoll, H., H. L. Ramsden and M. F. Nolan (2012). 'Intrinsic electrophysiological properties of entorhinal cortex stellate cells and their contribution to grid cell firing fields.' In: *Frontiers in neural circuits* 6.17, pp. 1–21.

Quirk, G. J., R. U. Muller and J. L. Kubie (1990). 'The firing of hippocampal place cells in the dark depends on the rat's recent experience'. In: *Journal of Neuroscience*.

Ramón y Cajal, S. (1909). 'Histologie du Systeme Nerveux de l'Homme et des Vertebres. Maloine, Paris: 1911. chap. II'. In: *Demography* 1.90, pp. 3–43.

Rand, W. M. (1971). 'Objective Criteria for the Evaluation of Clustering Methods'. In: *Journal of the American Statistical Association* 66.336, pp. 846–850.

Ray, S., A. Burgalossi, M. Brecht and R. K. Naumann (2017). 'Complementary Modular Microcircuits of the Rat Medial Entorhinal Cortex'. In: *Frontiers in Systems Neuroscience* 11.April, pp. 1–18.

Ray, S., R. Naumann, A. Burgalossi, Q. Tang, H. Schmidt and M. Brecht (2014). 'Grid-Layout and Theta-Modulation of Layer 2 Pyramidal Neurons in Medial Entorhinal Cortex'. In: *Science* 343.6173, pp. 891–896.

Reifenstein, E. T., R. Kempter, S. Schreiber, M. B. Stemmler and A. V. M. Herz (2012). 'Grid cells in rat entorhinal cortex encode physical space with independent firing fields and phase precession at the single-trial level.' In: *PNAS* 109.16, pp. 6301–6.

Reinagel, P., D. Godwin, S. M. Sherman and C. Koch (1999). 'Encoding of visual information by LGN bursts.' In: *Journal of Neurophysiology* 81.5, pp. 2558–69.

Richter, H., R. Klee, U. Heinemann and C. Eder (1997). 'Developmental changes of inward rectifier currents in neurons of the rat entorhinal cortex'. In: *Neuroscience Letters* 228.2, pp. 139–141.

Robertson, R. G., E. T. Rolls, P. Georges-François and S. Panzeri (1998). 'Head direction cells in the primate hippocampal formation'. In: *Hippocampus* 9, pp. 206–219.

Rousseeuw, P. J. (1987). 'Silhouettes: A graphical aid to the interpretation and validation of cluster analysis'. In: *Journal of Computational and Applied Mathematics* 20.C, pp. 53–65. arXiv: z0024.

Sargolini, F., M. Fyhn, T. Hafting, B. L. Mcnaughton, M. P. Witter, M. B. Moser and E. I. Moser (2006). 'Conjunctive Representation of Position, Direction, and Velocity in Entorhinal Cortex'. In: *Science* 312, pp. 758–762.

Schmidt-Hieber, C. and M. Häusser (2013). 'Cellular mechanisms of spatial navigation in the medial entorhinal cortex.' In: *Nature neuroscience* 16.3, pp. 325–31.

Schreiber, S., I. Erchova, U. Heinemann and A. V. M. Herz (2004). 'Subthreshold resonance explains the frequency-dependent integration of periodic as well as random stimuli in the entorhinal cortex.' In: *Journal of Neurophysiology* 92.1, pp. 408–415.

Schwartz, S. P. and P. D. Coleman (1981). 'Neurons of origin of the perforant path'. In: *Experimental Neurology* 74.1, pp. 305–312.

Schwerdtfeger, W. K., E. H. Buhl and P. Germroth (1990). 'Disynaptic olfactory input to the hippocampus mediated by stellate cells in the entorhinal cortex'. In: *Journal of Comparative Neurology* 292.2, pp. 163–177.

Scoville, W. B. and B. Milner (1957). 'Loss of recent memory after bilateral hippocampal lesions'. In: *Journal of Neurology, Neurosurgery and Psychiatry* 20, pp. 11–21. arXiv: `arXiv:1011.1669v3`.

Sherman, M. S. (2001). 'Tonic and burst firing: Dual modes of thalamocortical relay'. In: *Trends in Neurosciences* 24.2, pp. 122–126.

Simonnet, J., E. Eugène, I. Cohen, R. Miles and D. Fricker (2013). 'Cellular neuroanatomy of rat presubiculum'. In: *European Journal of Neuroscience* 37.4, pp. 583–597.

Skaggs, W. E. and B. L. McNaughton (1996). 'Theta Phase Precession in Hippocampal Neurinak Populations abd the Compression of'. In: *Hippocampus* 6, pp. 149–172.

Solstad, T., C. N. Boccara, E. Kropff, M.-B. Moser and E. I. Moser (2008). 'Representation of geometric borders in the entorhinal cortex.' In: *Science (New York, N.Y.)* 322.5909, pp. 1865–8.

Stafstrom, C. E. (2005). 'The role of the subiculum in epilepsy and epileptogenesis.' In: *Epilepsy currents* 5.4, pp. 121–129.

Steinhaus, H. (1956). 'Sur la division del corps matériels en parties'. In: *Bulletin de l'Académie Polonaise del Sciences - Classe III* 4.12, pp. 801–804.

Stensola, H., T. Stensola, T. Solstad, K. Frøland, M.-B. Moser and E. I. Moser (2012). 'The entorhinal grid map is discretized.' In: *Nature* 492.7427, pp. 72–8.

Steward, O. (1976). 'Topographic organization of the projections from the entorhinal area to the hippocampal formation of the rat'. In: *Journal of Comparative Neurology* 167.3, pp. 285–314.

Storm, J. (1987). 'Action potential repolarization and a fast afterhyperpolarization in rat hippocampal pyramidal cells.' In: *The Journal of Physiology* 385, pp. 733–759.

Suzuki, W. a. and D. G. Amaral (1994). 'Topographic organization of the reciprocal connections between the monkey entorhinal cortex and the perirhinal and parahippocampal cortices.' In: *The Journal of Neuroscience* 14.3, pp. 1856–77.

Tahvildari, B. and A. Alonso (2005). 'Morphological and electrophysiological properties of lateral entorhinal cortex layers II and III principal neurons.' In: *The Journal of Comparative Neurology* 491.2, pp. 123–40.

Tahvildari, B., M. Wölfel, A. Duque and D. A. Mccormick (2012). 'Selective Functional Interactions between Excitatory and Inhibitory Cortical Neurons and Differential Contribution to Persistent Activity of the Slow Oscillation'. In: *Journal of Neuroscience* 32.35, pp. 2165–2179.

Tamamaki, N. and Y. Nojyo (1995). 'Preservation of topography in the connections between the subiculum, field CA1, and the entorhinal cortex in rats'. In: *Journal of Comparative Neurology* 353.3, pp. 379–390.

Taube, J. S. and R. U. Muller (1998). 'Comparisons of head direction cell activity in the postsubiculum and anterior thalamus of freely moving rats'. In: *Hippocampus* 8.2, pp. 87–108.

Taube, J. S., R. U. Muller and J. B. Ranck, JB (1990). 'Head-direction cells recorded from the postsubiculum in freely moving rats. II. Effects of environmental manipulations'. In: *Journal of Neuroscience* 10.2, pp. 436–447.

Thompson, S. M., L. M. Masukawa and D. A. Prince (1985). 'Temperature dependence of intrinsic membrane properties and synaptic potentials in hippocampal CA1 neurons in vitro.' In: *The Journal of Neuroscience* 5.3, pp. 817–24.

Turner, R. W., L. Maler, T. Deerinck, S. R. Levinson and M. H. Ellisman (1994). 'TTX-sensitive dendritic sodium channels underlie oscillatory discharge in a vertebrate sensory neuron.' In: *The Journal of Neuroscience* 14.11, pp. 6453–6471.

Van Hoesen, G. W. and D. N. Pandya (1975). 'Some connection of the entorhinal (Area 28) and perirhinal (Area 35) cortices of the rhesus monkey I temporal lobe afferents'. In: *Brain* 95, pp. 1–24.

Van Strien, N. M., N. L. M. Cappaert and M. P. Witter (2009). 'The anatomy of memory: An interactive overview of the parahippocampal-hippocampal network'. In: *Nature Reviews Neuroscience* 10.4, pp. 272–282.

Varga, C., S. Y. Lee and I. Soltesz (2010). 'Target-selective GABAergic control of entorhinal cortex output.' In: *Nature Neuroscience* 13.7, pp. 822–824.

Visan, V., U. Heinemann, A. Volynets and W. Müller (2002). 'Calcium currents in rat entorhinal cortex layer II stellate and layer III pyramidal neurons in acute brain slice.' In: *Neuroscience letters* 327.3, pp. 153–156.

Ward Jr., J. H. (1963). 'Hierarchical Grouping to Optimize an Objective Function'. In: *Journal of the American Statistical Association* 58.301, pp. 236–244.

Winterer, J., N. Maier, C. Wozny, P. Beed, J. Breustedt, R. Evangelista, Y. Peng, T. D'Albis, R. Kempter and D. Schmitz (2017). 'Excitatory Microcircuits within Superficial Layers of the Medial Entorhinal Cortex'. In: *Cell Reports* 19.6, pp. 1110–1116.

Witter, M. P. and D. G. Amaral (2004). 'V. Cortex'. In: *The rat nervous system*. Ed. by G. Paxinos. Third Edit. Elsevier. Chap. 21. Hippoc, pp. 637–705.

Witter, M. P., T. P. Doan, B. Jacobsen, E. S. Nilssen and S. Ohara (2017). 'Architecture of the Entorhinal Cortex A Review of Entorhinal

Anatomy in Rodents with Some Comparative Notes'. In: *Frontiers in Systems Neuroscience* 11.June, pp. 1–12.

Witter, M. P., P. A. Naber, T. Van Haeften, W. C. M. Machielsen, S. A. R. B. Rombouts, F. Barkhof, P. Scheltens and F. H. Lopes Da Silva (2000). 'Cortico-hippocampal communication by way of parallel parahippocampal - subicular pathways'. In: *Hippocampus* 10.4, pp. 398–410.

Wong, R. K. and D. a. Prince (1981). 'Afterpotential generation in hippocampal pyramidal cells.' In: *Journal of neurophysiology* 45.1, pp. 86–97.

Wouterlood, F. G., E. Mugnaini and J. Nederlof (1985). 'Projection of olfactory bulb efferents to layer I GABAergic neurons in the entorhinal area. Combination of anterograde degeneration and immunoelectron microscopy in rat'. In: *Brain Research* 343.2, pp. 283–296.

Wouterlood, F. G., J. C. van Denderen, T. van Haeften and M. P. Witter (2000). 'Calretinin in the entorhinal cortex of the rat: distribution, morphology, ultrastructure of neurons, and co-localization with gamma-aminobutyric acid and parvalbumin.' In: *The Journal of Comparative Neurology* 425.2, pp. 177–92.

Ye, J., M. P. Witter, M.-B. Moser and E. I. Moser (2018). 'Entorhinal fast-spiking speed cells project to the hippocampus'. In: *PNAS*, p. 201720855.

Yeckel, M. F. and T. W. Berger (1990). 'Feedforward excitation of the hippocampus by afferents from the entorhinal cortex: redefinition of the role of the trisynaptic pathway.' In: *Proceedings of the National Academy of Sciences* 87.15, pp. 5832–5836.

Yoshida, M., L. M. Giocomo, I. S. Boardman and M. E. Hasselmo (2012). 'Frequency of subthreshold oscillations at different membrane potential voltages in neurons at different anatomical positions on the dorso-ventral axis in the rat medial entorhinal cortex'. In: *Journal of Neuroscience* 31.7489, pp. 12683–12694.

Yue, C. and Y. Yaari (2004). 'KCNQ/M Channels Control Spike Afterdepolarization and Burst Generation in Hippocampal Neurons'. In: *Journal of Neuroscience* 24.19, pp. 4614–4624.

Zhang, L., T. A. Valiante and P. L. Carlen (1993). 'Contribution of the low-threshold T-type calcium current in generating the post-spike depolarizing afterpotential in dentate granule neurons of immature rats.' In: *Journal of neurophysiology* 70.1, pp. 223–31.

Zola-Morgan, S., L. R. Squire, D. G. Amaral and W. A. Suzuki (1989). 'Lesions of perirhinal and parahippocampal cortex that spare the amygdala and hippocampal formation produce severe memory impairment'. In: *The Journal of Neuroscience* 9.12, pp. 4355–4370.

PUBLICATION LIST

ARTICLES

Franzen, D. L., S. A. Gleiss, C. Berger, F. S. Kuempfbeck, J. J. Ammer and F. Felmy (2014). 'Development and modulation of intrinsic membrane properties control the temporal precision of auditory brainstem neurons'. In: *Journal of Neurophysiology*, pp. 1–13.

SELECTED CONFERENCE PRESENTATIONS

Fischer, C., F. Kuempfbeck, J. Nagele, S. Haeusler, M. Stemmler, F. Felmy and A. Herz (2017). 'Biophysical Foundation and Function of the Depolarizing Afterpotential in Principal Cells of the Medial Entorhinal Cortex'. In: *Meeting of the National Bernstein Network Computational Neuroscience*.

Kuempfbeck, F., M. Stemmler, A. Herz and F. Felmy (2015). 'Origin and function of depolarizing afterpotentials in stellate cells in the medial entorhinal cortex'. In: *Göttingen Meeting of the German Neuroscience Society*.

ACKNOWLEDGMENTS

I would like to thank Andreas and Felix for being great supervisors, for hosting me in their labs, for teaching me a lot but most importantly for the many interesting discussions and the constant support throughout my PhD. Especially Felix' enthusiasm for patching and Andreas' thirst for knowledge and details have always been motivating and impressing.
I thank Caro, Jojo and Dora my project colleagues for the nice working atmosphere, all the fruitful discussions and your constant help and support.
I thank the whole Felmy lab, but especially Delwen and Alex for proofreading, critical comments and their valuable input on my projects. I thank Alisha for assisting me with some of my immunostainings and for being my printing officer.
I thank Diana, Eli, Ela, Ella, Steffi and all the other people from the third and first floor for creating such a fun and supportive atmosphere to work in. I very much enjoyed it over the last six years.
I thank Olga, Hilde, Jan, Sven, Christoph Kirst and the animal caretakers who kept everything running and helped me a lot with ImageJ, Matlab, Template Creator or other problems.
Ein großes Danke auch an meine Familie, vor allem an meine Mama, meine Schwester, meine Lilli und an meine Schwiegereltern, die mich immer unterstützt und es mir ermöglicht haben mit kleinem Kind fertig zu promovieren.
Als letztes will ich mich bei Stephan und Ronja für ihre Unterstützung und ihre Geduld bedanken. Ihr musstet einiges an gemeinsamer Zeit opfern und wart trotzdem immer sehr nachsichtig mit mir. Die rare gemeinsame Zeit habt ihr mir sehr versüßt und damit meine Motivation aufrechterhalten.

EIDESSTATTLICHE ERKLÄRUNG / AFFIDAVIT

Ich versichere hiermit an Eides statt, dass die vorgelegte Dissertation von mir selbständig und ohne unerlaubte Hilfe angefertigt ist.

Herrsching, 24th July 2018

Franziska S. Kümpfbeck

Erklärung

Hiermit erkläre ich,

- ☒ dass die Dissertation nicht ganz oder in wesentlichen Teilen einer anderen Prüfungskommission vorgelegt worden ist.
- ☒ dass ich mich anderweitig einer Doktorprüfung ohne Erfolg **nicht** unterzogen habe.
- ☐ dass ich mich mit Erfolg der Doktorprüfung im Hauptfach ..... und in den Nebenfächern ..... bei der Fakultät für ..... der..... (Hochschule/Universität) unterzogen habe.
- ☐ dass ich ohne Erfolg versucht habe, eine Dissertation einzureichen oder mich der Doktorprüfung zu unterziehen.

Herrsching, 24th July 2018

Franziska S. Kümpfbeck